



**NTNU – Trondheim**  
Norwegian University of  
Science and Technology

# Nanomechanical testing of in situ hydrogen charged high strength steel

**Jonatan Kuipers**

Master of Science in Mechanical Engineering

Submission date: June 2013

Supervisor: Christian Thaulow, IPM

Co-supervisor: Afrooz Barnoush, IPM

Norwegian University of Science and Technology  
Department of Engineering Design and Materials



THE NORWEGIAN UNIVERSITY  
OF SCIENCE AND TECHNOLOGY  
DEPARTMENT OF ENGINEERING DESIGN  
AND MATERIALS

**MASTER THESIS SPRING 2013  
FOR  
STUD. TECHN. JONATAN KUIPERS**

**NANOMECHANICAL TESTING OF IN SITU HYDROGEN CHARGED HIGH  
STRENGTH STEEL**

**Nanomekanisk testing av in situ hydrogen beladet høyfast stål**

Hydrogen embrittlement in high strength steel is a serious problem across several industries, and the focus for developing computational models for evaluating its impact is essential. The EU-project MultiHy focus on understanding the mechanisms of hydrogen embrittlement and to link the mechanisms to practical applications in industry. This Master thesis is closely linked to the activities in the EU project.

By applying the Focused Ion Beam at NTNU Nanolab specific microstructures or grains can be chosen for the investigation of nano-sized structures by machining pillars and cantilever beams. These specimens can subsequently be tested using a Nanoindenter at the Nanomechanical laboratory, and the resulting stress-strain relationships and fracture toughness can be quantified. This will provide detailed understanding of the deformation mechanisms of the microstructural constituents.

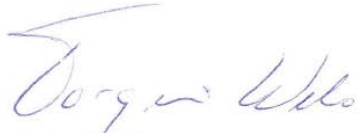
During the loading process, an experimental method has been developed allowing submerging the specimens in an electrolyte and charging with hydrogen. This provides the opportunity to study the effect of hydrogen embrittlement at the nano-scale.

This thesis will investigate the effect of finely dispersed titanium and niobium carbides on the nanomechanical behavior of high strength steel in the presence of hydrogen. This will be performed by nanomechanical testing of pillars and cantilever beams on samples with and without carbides both in the presence of hydrogen and without.


The thesis should include the signed problem text, and be written as a research report with summary both in English and Norwegian, conclusion, literature references, table of contents, etc. During preparation of the text, the candidate should make efforts to create a well arranged and well written report. To ease the evaluation of the thesis, it is important to cross-reference text, tables and figures. For evaluation of the work a thorough discussion of results is appreciated.

Three weeks after start of the thesis work, an A3 sheet illustrating the work is to be handed in. A template for this presentation is available on the IPM's web site under the menu "Masteroppgave" (<http://www.ntnu.no/ipm/masteroppgave>). This sheet should be updated one week before the Master's thesis is submitted.

The thesis shall be submitted electronically via DAIM, NTNU's system for Digital Archiving and Submission of Master's thesis.



Torgeir Welo  
Head of Division



Christian Thaulow  
Professor/Supervisor



NTNU  
Norges teknisk-  
naturvitenskapelige universitet  
Institutt for produktutvikling  
og materialer

# Abstract

---

The effect of finely dispersed titanium carbides on the nanomechanical behavior of high strength steel in the presence of hydrogen has been investigated. Nano sized pillars have been milled from steel samples using a Focused Ion Beam at the NTNU Nanolab. These have been compressed both in air and with in situ charged hydrogen. The resulting stress-strain curves have been extracted and compared against each other. An effect of hydrogen was found in martensitic phases, with the titanium carbide-containing sample showing less hydrogen damage than the sample without titanium. The same tests performed in the ferritic phase in specifically-chosen grains displayed no hydrogen effect on the yield strength, but in both cases the effect of hydrogen was observed in the increase of strain hardening for the titanium carbide-containing samples. A method for switching charging potentials during compression of a single nanopillar was developed, tested, and showed the effect of hydrogen on both samples, without a clear reduction for the titanium carbide-containing sample.

# Abstrakt

---

Effekten av finfordelte titankarbider på den nanomekaniske virkemåten av høyfast stål i nærvær av hydrogen har blitt undersøkt. Nanopillarer har blitt frest fra stålprøver ved hjelp av en Focused Ion Beam ved NTNU Nanolab. Disse har blitt komprimert både i luft og med in situ ladet hydrogen. De resulterende belastningskurvene er blitt uthentet og sammenlignet med hverandre. En effekt av hydrogen ble funnet i de martensittiske fasene av prøvene, hvor prøven med titankarbider viser mindre hydrogenskade enn prøven uten titan. De samme testene utført i ferrittisk fase i spesielt-valgte korn viste tilnærmet ingen effekt av hydrogen på flytegrensa, men i begge tilfeller ble hydrogeneffekten observert i form av en økning av tøyningsherdingen for prøven med titankarbider. En metode for vekslende ladet potensial for testing av enkelte nanopillarer ble utviklet, testet og viste hydrogeneffekten for begge prøver, uten en tydelig reduksjon for prøven med titankarbider.

## Contents

1	Introduction.....	6
2	Acknowledgements.....	7
3	MultiHy.....	8
4	Theoretical background .....	10
4.1	Hydrogen embrittlement.....	10
4.2	Mechanisms for hydrogen embrittlement.....	11
4.2.1	Hydrogen enhanced decohesion.....	11
4.2.2	Hydrogen enhanced localized plasticity.....	11
4.2.3	Hydrogen-induced embrittlement .....	11
4.2.4	Mechanisms evaluation .....	12
4.3	Hydrogen transport and trapping.....	12
4.4	Hydrogen embrittlement test methods .....	13
4.5	Electron Backscatter Diffraction.....	13
4.6	Focused Ion Beam.....	14
4.7	Nanomechanical indentation .....	16
5	Experimental .....	18
5.1	Sample data .....	18
5.2	Sample preparation .....	19
5.3	Electron Back-Scatter Diffraction .....	20
5.3.1	System specifications .....	20
5.3.2	Orientation selection process .....	22
5.4	Focused Ion Beam pillar milling.....	23
5.5	Nanomechanical indentation .....	26
5.5.1	Indenter setup.....	26
5.5.2	Electrochemical nanoindentation setup.....	29
5.5.3	In situ electrochemical testing.....	30
5.6	Post-compression imaging .....	33
6	Results .....	36
6.1	Surface indentations on samples 1400M.....	36
6.1.1	Indentation in air.....	36
6.1.2	Indentations in air and with hydrogen charging.....	37
6.2	Pillar compression on samples 1400M.....	38
6.3	Pillar compression on samples 1200M.....	40
6.4	Experimental pillar compression on samples 1400M, changing potentials.....	41

7	Discussion.....	46
7.1	Surface indentations on samples 1400M.....	46
7.2	Pillar compression on samples 1400M.....	46
7.3	Pillar compression on samples 1200M.....	47
7.4	Experimental pillar compression on samples 1400M, changing potentials.....	48
7.5	Further work.....	49
8	Conclusions.....	50
9	Bibliography.....	51
10	Appendix.....	53
10.1	Pillar compression on samples 1400M.....	53
10.2	Pillar compression on samples 1200M.....	63
10.3	Experimental in situ potential switching.....	74

# 1 Introduction

---

Hydrogen embrittlement is a huge and costly problem spanning multiple industrial sectors today, such as the producers of aircrafts, ships or nuclear reactors. Metals become brittle due to hydrogen exposure and can in some cases lead to catastrophic cracking of the material. It can occur anywhere in a metals lifetime, both in manufacturing and in operational use, as long as it is in contact with atomic or molecular hydrogen. The susceptibility of a metal to hydrogen embrittlement depends on several factors, and by controlling some of these factors it might be limited.

One of the potential factors for this is increasing the amount of carbides such as niobium and titanium to trap the diffusing hydrogen atoms and thus hinder the embrittling effect of hydrogen. Through the EU-project MultiHy, which is presented in the next chapter, samples of different heat treatment were received in sets of twos: one containing carbides and one without. Focus is put on performing the exact same procedures for the two samples, including sample surface preparation, milling of nanostructures and loading conditions. This is done so that the only difference is the carbides in one sample.

Measuring the effect of this countermeasure has been the goal of this thesis. Equipment is now available to do testing on a nano scale, which allows investigation of the deformation mechanisms that takes place. Using nanomechanical instruments specimens like pillars of diameter  $1\mu\text{m}$  and smaller can be fabricated by shooting ions towards a sample. Once constructed, the pillars can be compressed by a nanoindenter system where all loading parameters can be decided and monitored.

With a custom made sample holder the sample can be submerged in electrolyte, and by controlling the applied current hydrogen can be charged. This technique of in situ electrochemical nanoindentation has proved advantageous for investigating the hydrogen damage.

This thesis builds further upon the work of the author in the project work of 2012 (1), where much work was put into finding the best possible method of preparing the sample surface for nanomechanical testing. Several techniques were tested before a method was chosen. Indentations tests were performed on sample sets with and without both niobium and titanium in air. Throughout this thesis the focus has been to test the sample sets with and without titanium both in air and under hydrogen charging.



## *2 Acknowledgements*

---

The spring of 2012 I was introduced to advanced equipment such as different scanning electron microscopes, the Focused Ion Beam and the nanoindenter. This following year has been an interesting journey, which has been aided by many along the way. First, for showing me the ropes even as she was completing her own thesis an appreciation goes to M.Sc. Veronica G. Haugen. Next my supervisor Prof. Christian Thaulow is thanked for his continuous positive feedback and ideas even when stationed in India. Post Doc. Afroz Barnoush is thanked for his in-depth knowledge of the testing procedures and many fresh experimental ideas. Lastly PhDs Bjørn Rune Rogne and Adina Basa have always been available for any type of inquiry, and that is appreciated greatly. Finally, thanks go to Senior Engineer Yingda Yu and Prof. Wilhelm Dall (both Department of Material Science and Engineering) for their help with any troubles regarding EBSD-mapping.

### 3 MultiHy

MultiHy is the acronym for the EU-project “Multiscale Modeling of Hydrogen Embrittlement”, and the work performed in this master thesis is included in the project. MultiHy was started in May of 2011 and has a planned duration of 48 months. Its purpose is to develop an advanced multiscale framework for numerical modeling of hydrogen embrittlement. The project was initiated to be able to apply this model to a wide range of industrial problems, ranging from superficial metal corrosion to material failure. The project aims to be a big step towards achieving a tool for evaluating a materials’ susceptibility towards hydrogen embrittlement based on what microstructure, mechanical loading and environmental conditions are present.

MultiHy is using a “bottom-up”-approach, by starting with the creation of a large database using atomistic and kinetic Monte Carlo simulations to assess the behavior of hydrogen in a 3-dimensional complex microstructure, which is illustrated in Level 1 in Figure 1. The work performed in this master thesis, the physical testing, is a part of Level 4.

The main focus of the development of this model is the determination of how and with what rate hydrogen is transported the material. Materials will then be inspected to locate the key microstructural features which affect the rate and the method for hydrogen transport to the fracture initiation site.

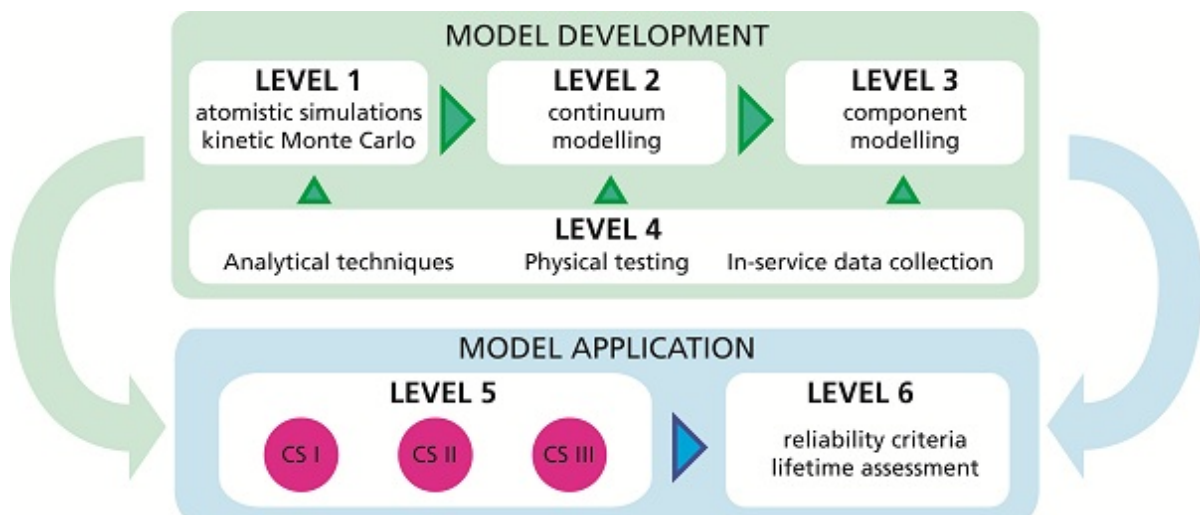


Figure 1 - MultiHy website (2); illustration of the approach of MultiHy

In addition to the development of a numerical model, the project has three case studies in which the effectiveness of the model will be tested. These three cases are shown in Level 5 in Figure 1, and the evaluation of these three studies will help determine the reliability of the model. Case study 1 involves the Ariane 5 satellite launcher, and seeks to optimize the pulse-plating process which is used during the fabrication of the nickel combustion chambers of the satellite. Case study 2 is focused on future automobile chassis components, where the goal is trying to minimize the influence of hydrogen embrittlement on the performance of the high-strength steel. This case study is the most relevant of the three in relation to this

project work. Case study 3, the final case study in the MultiHy project, is focused on predicting the lifetime of next-generation wind turbine bearings. Predicting the impact of hydrogen embrittlement on the bearings will help maximize the efficiency of the wind-turbines. These three case studies, illustrated in Figure 2, are good examples which reflect the diversity of problems related to hydrogen embrittlement across many industrial sectors.



Figure 2 - MultiHy website (2); illustration of three case studies

## 4 Theoretical background

---

This chapter will explain what hydrogen embrittlement is, and in what way it affects and damages materials. A number of mechanisms explaining hydrogen embrittlement have been proposed, and the ones which there are consensus about will be presented and discussed here.

### 4.1 Hydrogen embrittlement

---

For a long period of time hydrogen embrittlement in steel has been a technical challenge spanning several industrial sectors. Hydrogen embrittlement is the process in which different materials are degraded following hydrogen influence. The most common degradation method for steels is becoming brittle before eventually fracturing. The implementation of Multihy as an EU-project is a testament to how big of a problem hydrogen embrittlement has become.

When a material is affected by hydrogen embrittlement it is always initiated by the introduction of hydrogen into the material, for instance the absorption of hydrogen from seawater. For metals and steel this normally happens as single hydrogen atoms diffuse through the affected material. This diffusion into the material is made possible when the solubility of the hydrogen is elevated, for instance as a consequence of high temperatures. Hydrogen molecules are formed as the hydrogen atoms diffusing through the material regroup in voids inside the material matrix. These voids are normally at one of two locations in the microstructure (3); either in the interstitial lattice sites, or other sites associated with some crystalline defect. The formation of these hydrogen molecules creates a pressure, which, if it increases sufficiently, can induce a reduced ductility and tensile strength of the material. If the pressure increases further it can cause the void to crack open, known as hydrogen induced cracking. Metals with high-strength and low-alloy are most susceptible to hydrogen embrittlement. Although not technically metal, this also includes the steel samples in this project, which either contain titanium or are titanium-free in order to have reference points.

An initial suggestion of what hydrogen embrittlement is was made by Beachem (4) in 1972, where he presented a model for hydrogen-assisted cracking. This model showed that sufficiently concentrated hydrogen which dissolves into the lattice ahead of the crack tip would enhance the deformation processes, depending on what microstructure is present. Exactly how this enhancement worked was something he did not detail further, and since then there have been numerous suggestions of how hydrogen-assisted cracking takes place.

Beachem's model that hydrogen facilitated dislocation movement was later supported by amongst others Birnbaum (5), who went further in concluding there was support for mechanisms he referred to as "Hydrogen Induced Decohesion" (which will be referred to as hydrogen enhanced decohesion in this thesis) and "Hydrogen Enhanced Localized Plasticity". These will both be presented in the next section. As many others Birnbaum concluded that several of the mechanisms might be present in a single system, either as competing effects or working in combination.

## 4.2 Mechanisms for hydrogen embrittlement

---

The most advanced atomistic mechanisms for hydrogen embrittlement are hydrogen enhanced decohesion (HEDE), hydrogen enhanced localized plasticity (HELP) and hydrogen-induced embrittlement (HIE). In this section these will be presented individually and discussed in general.

### 4.2.1 Hydrogen enhanced decohesion

---

Initially introduced by Troiano (6) and further developed in detail by Oriani (7), this mechanism assumes a reduction in the interatomic cohesive forces due to the presence of interstitial hydrogen, which accumulates within the lattice itself. When these forces are reduced, tensile separation is preferred to slip as the local tensile stress exceeds the local atomic cohesive strength. The hydrogen fracture sites can be found at the sites with the maximum hydrogen concentration, which according to both Sun et al. (8) in single fcc crystal and Gao (9) in low-alloy steel, either is in the immediate vicinity of the crack tip or at a distance from the crack tip, respectively corresponding to the locations of the maximum equivalent strain and maximum hydrostatic stress. In order to be able to predict this we need to know the concentration of hydrogen located at the fracture site and how the crack tip stress is distributed. The former is dependent on how soluble the hydrogen is at the tip of the crack.

### 4.2.2 Hydrogen enhanced localized plasticity

---

Due to the presence of hydrogen, there is a reduction in the interaction between dislocations and elastic obstacles. This means there will be enhanced dislocation mobility (thus an enhanced plasticity). This enhancement in localized plasticity indicating plastic failure is quite different from what is normally viewed as the embrittling effect of hydrogen.

This increase in localized plasticity, enhancing plastic failure because of hydrogen interaction was also suggested by Beachem (4). His suggestion was that the hydrogen would enhance the dislocation processes so that the localized plastic deformation would be sufficiently large to lead to a crack growth, which macroscopically would be brittle.

### 4.2.3 Hydrogen-induced embrittlement

---

This mechanism is in place when several small hydride fields nucleate and grow together ahead of the crack tip, as documented by Robertson and Birnbaum (10). Their observations showed the hydrides to nucleate in the stress-field of the crack by several small hydrides growing together to form larger hydrides. This combination of hydrides has appeared to be the main cause for embrittlement, especially for elements known for hydride forming such as Nb and Ti. Chan (11) added that the tensile ductility would decrease according to how continuous the hydride network was, and the most damaging hydride network would be the one placed along the grain boundaries.

#### 4.2.4 Mechanisms evaluation

---

HEDE, HELP, and HIE are the three most agreed upon atomic mechanisms for describing how hydrogen embrittlement takes place within a metal. Gangloff (12) concluded in 2003 that the emerging consensus was that HEDE is the main damage mechanism for both internal hydrogen assisted cracking as well as for hydrogen environmentally assisted cracking for high strength alloys. His conclusion was supported by the fact that only the HEDE model had been developed into models which were capable of predicting macroscopic hydrogen cracking properties for the use of structural integrity modeling.

Lynch (13) in 2007 concludes with that there are four mechanisms of hydrogen-assisted cracking, for which there is significantly experimental and theoretical support. These are the three already discussed here and a mechanism named adsorption-induced dislocation-emission (AIDE). This last mechanism is just like HEDE based on hydrogen-induced weakening of interatomic bonds, but more like HELP the crack growth is occurring by localized slip. Hydrogen is absorbed by the surface and by weakening the inter-atomic bonds, facilitates the dislocation-emission. Lynch continues by stating that the HEDE mechanism most likely predominates for fractures occurring intergranularly, especially for high hydrogen concentrations. HELP is attributed to localizing slip in stainless steels, but only a minor role in other fracture modes.

### 4.3 Hydrogen transport and trapping

---

The mode and degree of seriousness of hydrogen damage are dependent on a number of factors. These include what source of hydrogen there is (whether gaseous or dissolved in the material), alloy specifications, surface treatment, exposure time and temperature. These factors influence how fast the hydrogen transport into the material is and possibly how much hydrogen trapping takes place. Whereas a high hydrogen transport rate can be damaging, an increased hydrogen trapping can help in decreasing the hydrogen damage. The inclusion of Titanium and Niobium is potentially an important aid for increasing hydrogen trapping. The addition of a carbide forming element such as Titanium or Niobium (or Chromium, Molybdenum, Tungsten or Vanadium (14)) is therefore being considered to use for an increased resistance to hydrogen damage.

As described by Pressouyre and Bernstein (15), a quantitative measure of hydrogen traps in a metal alloy can be done, but requires knowledge of the number of different trap types. The traps can be analyzed and identified by quantitative metallography. They also suggested that being able to choose trap types would become an important factor for designing alloys able to resist hydrogen damage. The nature of a Ti carbide particle trap is an irreversible one under room temperature. Pressouyre (16) also describes how the initial state of the material can affect the traps, depending on whether the hydrogen embrittling effect is internal or external. Describing the traps as either sinks or sources, sinks will help catch the hydrogen and hinder its flow to potential crack initiation sites, and sources will facilitate hydrogen transport in the material and thus increase the risk of hydrogen damage. The nature of hydrogen-deformation interactions and how opposite effects can be observed was reviewed by Brass and Chene (17), pointing out that both plasticity and embrittlement could be increased in alloys due to hydrogen.

More recently, hydrogen trapping sites in Ti carbides precipitation-hardening steel has been directly observed through 3-dimensional atom probe tomography by Takahashi et al. (18).

#### **4.4 Hydrogen embrittlement test methods**

---

There have been a number of suggested methods for testing how susceptible a material is to hydrogen embrittlement. Non-destructive methods have been proposed in the purpose of quantifying hydrogen attack, such as the use of ultrasonic equipment. In 1989 Turnbull et al. (14) recommended that using advanced ultrasonic backscatter techniques was the best method for detection of hydrogen damage. The most relevant inspiration for this thesis is that of Jules Dake (19), in which a method combining in situ electrochemical nanoindentation with micropillar compression is described.

Standardized tests are rare but the American Society for Testing and Materials (ASTM) have two tests for investigating the embrittlement caused by hydrogen gas (20). “Standard Test Method for Determination of the Susceptibility of Metallic Materials to Hydrogen Gas Embrittlement (HGE) Test” involves a diaphragm loaded with differential pressures and quantifies the susceptibility of metallic materials to hydrogen embrittlement. The second, “Standard Test Method for Determination of Susceptibility of Metals to Embrittlement in Hydrogen Containing Environments at High Pressure, High Temperature, or Both” is a method which uses a hydrogen-pressurized chamber containing a cylindrical tensile specimen.

#### **4.5 Electron Backscatter Diffraction**

---

Electron backscatter diffraction (EBSD) is a method used for examining the crystallographic orientation of a material. It is an increasingly good tool for quantitative metallography in materials with fine grains, as evaluated by Humphreys (21). The necessity for adjusting the initial software-set parameters was reviewed by Palizdar et al (22). The process is usually conducted using a scanning electron microscope (SEM) equipped with an additional EBSD detector. The material sample is inserted into the microscope chamber before the chamber is pumped to vacuum. The sample is then tilted to a high angle relative to the normal, such as 70°, in order to increase the contrast of the resulting EBSD pattern.

When the electron source fires electrons on the sample surface, some of the backscattered electrons will be registered onto the EBSD detector, or more precisely a phosphor screen. Inside the detector, behind this screen, is a camera which is able to capture the backscattered electrons on the phosphor screen.

When several different planes diffract different electrons an electron backscatter pattern (EBSP) is created, such as the ones illustrated in Figure 3 and Figure 4. The bands which are visible in both figures are called Kikuchi bands, and have their origin from the Japanese

physicist Seishi Kikuchi. The Kikuchi band corresponds to each of the lattice diffracting planes, and depending on the expected crystal phase and orientation of the material the system will attempt to relate these bands to the bands which are present in the expected EBSP's of the material.

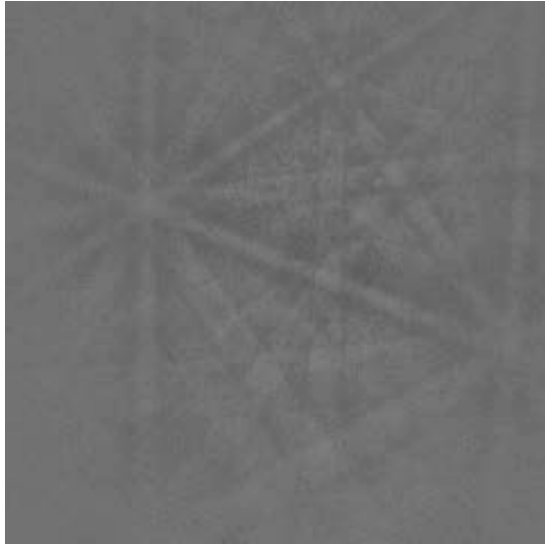


Figure 3 - EBSP #1, sample 1200M

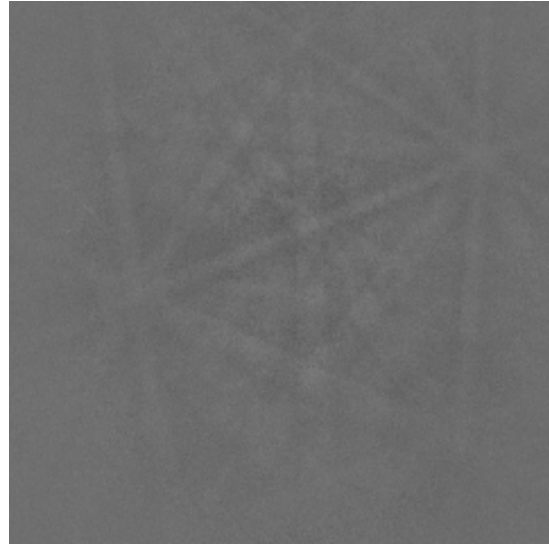


Figure 4 - EBSP #2, sample 1200M

Each EBSP represents a single data point in a scan over the area of which one is obtaining an EBSD map. Selecting the step size will determine the number of EBSP's. More EBSP's will mean a more detailed EBSD map, but will also result in a longer computational time. This is because each EBSP has to be indexed, meaning identifying the crystal orientation in that point. This is done successively for all the patterns, where the bands of each pattern are indexed by Miller indices from the diffracting planes which created it. In order to have a unique solution, three intercepting bands are normally sufficient.

#### 4.6 Focused Ion Beam

---

The focused ion beam (FIB) system is a great tool for manipulating matter on the nanometer scale. The FEI Helios Nanolab DualBeam FIB at NTNU Nanolab, shown in Figure 5 has both imaging capabilities through a scanning electron microscope (SEM) as well as machining capabilities. The system contains two beams, one electron beam which is mostly used for imaging and one ion beam which is used for characterization of the sample.

Both beams are based on a stream of charged particles which is focused by several lenses and apertures onto a test sample. When the sample holder is calibrated to the eucentric height and tilted to  $52^\circ$  relative to the normal, the SEM can be used to image the sample even as the FIB is milling out a pattern. Although this only works for low currents, it can be highly advantageous to be able to watch the process live, for instance verifying that the FIB hits the intended location on the sample.





Figure 5 - FEI Helios DualBeam at NTNU Nanolab

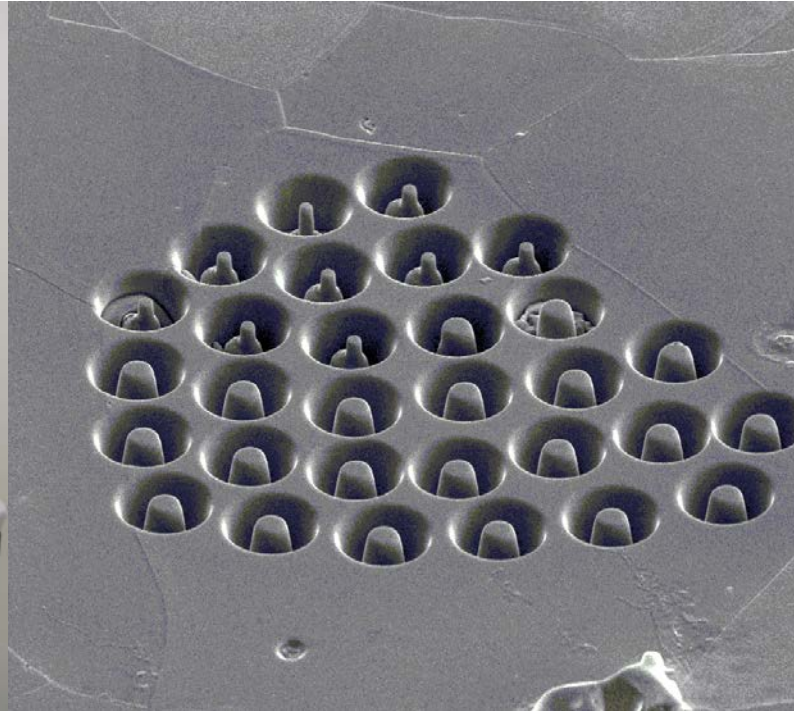


Figure 6 - FIB-milled structures on a pure Fe sample

The machining capabilities of the FIB include milling (illustrated in Figure 6), deposition and implantation of ions. In short the FIB system is manufacturing and directing a stream of high-energy ionized atoms towards the sample surface. As the ions are significantly more massive than the electrons ( $Ga^+$  ions, used in the NTNU Nanolab, are around 130 000 times larger (23)), they can more easily expel atoms on the sample surface from their original position. This milling function has been used in the work with this Master thesis. To ensure that only the sputtering interaction is achieved, as opposed to inelastic interactions and trapping of the ions, it is important to use the correct energy level, which is normally in the range of 10 to 100 kV.

There are several difficulties associated with the usage of FIB. In addition to milling out nanostructures there is the risk that the remaining structure is damaged by the ion milling, or in fact that some of the ions have been implanted in the structure. Both these cases will inevitably result in affected test results from the following structure. Another risk is that of redeposition, where some of the milled away material sticks to another part of the already-milled structure, changing the desired outcome. These effects have been evaluated with respect to nanopillar production by Ali et al. (24), who concluded that the FIB is both feasible and efficient for pillar production. The damaging effects can be reduced by milling in several steps, and using lower currents for producing finer structures, as this means less ion damage to the final structures.

## 4.7 Nanomechanical indentation

---

Nanomechanical indentation has in the last few decades become increasingly relevant as a tool for examining material properties on a nano scale and relating them to the macro. Although some deformations and fracture mechanisms reported on the nanoscale might not be observed on the macro because of their dimensions, reviews such as Palacio and Bhushan (25) conclude with nanoindentation's continued necessity.

As the tools become more and more precise performing in situ experiments is facilitated. In this thesis a Triboindenter TI950 with a Performech controller in the Nanomechanical lab at IPM, NTNU has been used for both surface indentations and pillar compressions. The Triboindenter is used for scanning the surface and indenting, and it is also equipped with an optical microscope, allowing the user identification and visualization of the sample prior to testing.

Choosing the tip is an important step and depends on several factors such as the material, type of test and indentation depth. For surface indentation there are several possibilities, and the most frequently used is the Berkovich indenter tip. This tip has the shape of a three-sided pyramid and maintains a similar geometry down to very small scales. Typical indentations, a total of six of them from this tip can be seen in Figure 7. One of the indents is highlighted by a red circle.



Figure 7 - Berkovich indentations in sample 1200TM

For pillar compression testing the tip has to be large enough to cover the top of the pillar, and at the same time small enough to not hit the walls of the crater surrounding the pillar. The natural choice is to use a flat tip in order to hit the top of the pillar as uniformly as possible.

Upon compiling the load-displacement curves from pillar compression there are a number of ways to analyze the data. The data are converted to stress and strain values depending on each of the pillars' diameter and height according to the following equations.

$$\sigma = \frac{F}{A} = \frac{F}{\pi r^2} \quad (1)$$

$$\epsilon = \frac{\Delta l}{l_0} = \frac{d}{l_0} \quad (2)$$

In Equation 1,  $\sigma$  is the stress, F the force and A the area over which the force is applied and r the radius measured from the pillar images. In Equation 2,  $\epsilon$  is the strain,  $\Delta l$  and d is the displacement and  $l_0$  the initial height of the pillar. The height and diameter are measured from SEM-images, taking into account the tilt of 52°. After the data have been converted as stress and strain they are plotted. In order to compare different sets of data to each other it can be very beneficial to find a mean plot for each data set. A modified Voces relation has been used in this thesis.

$$\sigma = A - Be^{-C\epsilon} + D\epsilon \quad (3)$$

In Equation 3, A,B,C and D are global constants which by the help of a program like Sigma Plot are calculated by means of a curve fitting based on a data set. The last element including the constant D is added for better stress-values for high strain. This proved to be a good basis for comparing the results of the differing data sets. An example of a curve fitted plot is seen in Figure 8, where the dotted lines are the data set and the blue line is the curve fitted plot. As the unloading part of the curves do not provide needed information and are quite varying, they are excluded from the curve fitted model.

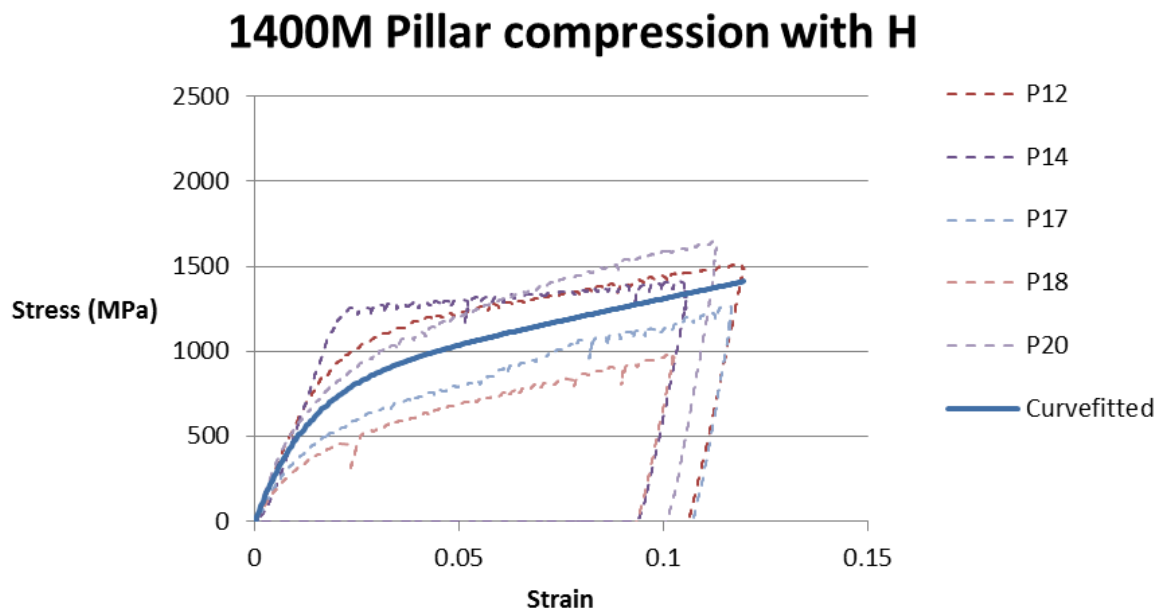


Figure 8 - Curve fitted plot along with data set from sample 1400M

## 5 Experimental

This chapter is devoted to explaining all the experimental work performed in this thesis, from sample preparation through EBSD-mapping, milling nanostructures, indentation and post-compression images and analysis.

### 5.1 Sample data

The samples used in this thesis are provided by ThyssenKrupp Steel Europe AG and are made of sets of two samples with the same heat treatment where one contains 0,13% titanium and the other contains no titanium. All the samples were received in October of 2012 and were cut into round samples of approximately 12mm diameter by post doc. Afroz Barnoush. There were a total of 8 samples, which are 4 sets of samples with and without Ti. The different heat treatments are shown in Figure 9.

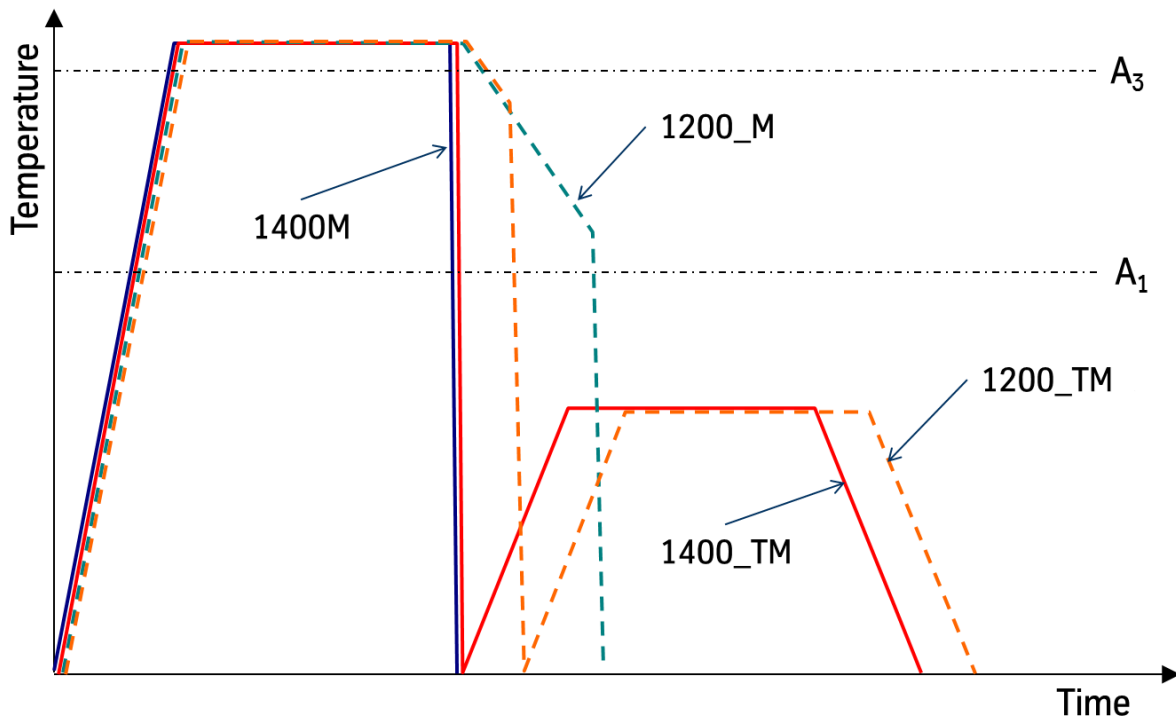


Figure 9 - Heat treatment curves for ThyssenKrupp samples

As the heat treatment diagram shows, all of the samples were warmed before being quenched in different speed. The samples 1400TM and 1200TM were reheated in order to achieve an additional tempering of them. In Table 1 a summary of all the samples used in this thesis is shown, and the types of tests performed on each sample set is also provided. As the table shows, 3 of 4 sample sets have been used for testing.

Sample	Microstructure	Ti content	Tests performed
1200M_Ti	Dualphase	0,13%	Pillars compressed in ferritic grains
1200M	martensite & ferrite	0	
1400M_Ti	Martensitic	0,13%	Pillars compressed & surface indentations
1400M		0	
1200TM_Ti	Tempered dualphase	0,13%	Surface indentations
1200TM	martensite & ferrite	0	
1400TM_Ti	Tempered	0,13%	
1400TM	martensite	0	

Table 1 - Samples summary

## 5.2 Sample preparation

When performing material testing on a nanometer scale it is imperative to have the sample surface as clean as possible. To achieve this, a thorough sample surface preparation must be done before the testing can begin. Several techniques, such as ion milling was initially tested (1) before settling on a method involving grinding in two steps followed by an electropolish.

When the samples had been cut into approximately 12mm diameter round pieces they were mechanically grinded. In the first step both sides of the samples were grinded with 800 silicon carbide (SiC) paper. The back of the sample was grinded to ensure conductivity all through the sample. This grinding was done by using double-side tape to stick the samples to a finger so as to apply an appropriate light pressure while grinding. Likewise the samples were then grinded even finer using 1200 SiC paper. Between each grinding the samples are thoroughly washed with ethanol using an ultrasonic bath before drying the samples using a hairdryer.

The final step of the sample preparation is electropolishing. The method is performed using a Struers LectroPol-5 at the Metallurgy lab in IPM, NTNU. With the help of PhD. Adina Basa an electrolyte consisting of 95% methanol (CH<sub>3</sub>OH) and 5% sulfuric acid (H<sub>2</sub>SO<sub>4</sub>) was mixed. Following some initial scans, the samples were polished at 14V with a flow rate of 13 for 40 seconds. After the electropolish is completed, the samples are quickly washed in the same manner as after the grinding steps. The electropolishing process is illustrated in Figure 10.

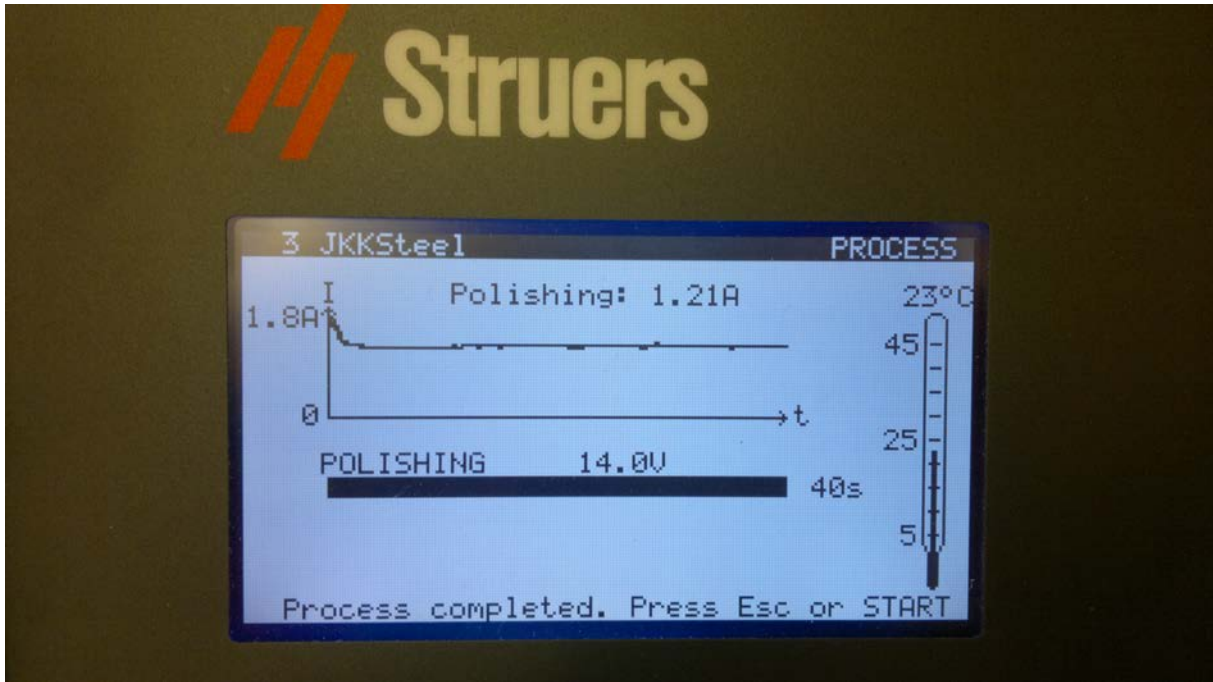


Figure 10 - Completed electropolish using Struers LECTROPOL-5

## 5.3 Electron Back-Scatter Diffraction

### 5.3.1 System specifications

After the surface is well prepared the next experimental step is examining the crystallographic orientation of each grain of an area on the sample surface. This was done using the Hitachi SU-6600 at Materialteknisk, NTNU. The SEM is first calibrated by adjusting the beam alignment, choosing acceleration voltage and focusing on the sample surface. The sample stage is then tilted to 70°, before the EBSD detector is inserted.

Further the area of interest is selected and scanned using the software Nordif. From the pre-scanned area the system further requires five calibration points and one acquisition point with good Kikuchi patterns. To assure that the resulting EBSD maps are reliable these calibration patterns need to be as clear as possible. The software provides a confidence index number for each point, indicating the certainty of a correctly calculated orientation. After much experimentation with the values in the software, Table 2 shows the experimental setup used here.

Parameter, Nordif 1.4.0	Value
Working distance	25 mm
Tilt angle	70°
EBSB detector	UF-1000
Acquisition frame rate	450 fps
Acquisition resolution	120x120 px
Acquisition exposure time	2172 $\mu$ s
Acquisition gain	2
Calibration frame rate	100 fps
Calibration resolution	240x240 px
Calibration exposure time	9950 $\mu$ s
Calibration gain	4
Acquisition points acquired	1
Calibration points acquired	5

Table 2 - EBSD parameter in Nordif

When the scan from Nordif is completed, the software TSL OIM Data Collection 6 is used to index the scan. Upon completion of the indexing, the map is finally visible using TSL OIM Analysis 6. There are several options available on how to read the data, including confidence index and image quality maps. These provide an extra insight when reviewing the quality of the maps, and are illustrated respectively in Figure 11 and Figure 12. In both illustrations brighter means better and darker worse EBSP's in this point.

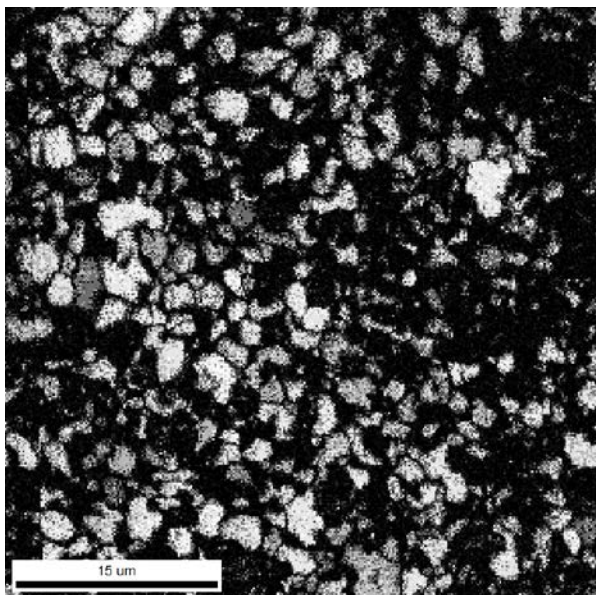


Figure 11 - Confidence index from sample 1200M\_Ti

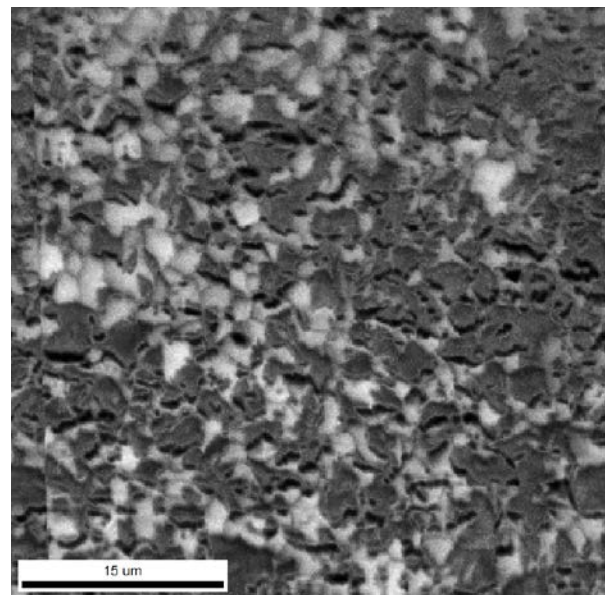


Figure 12 - Image quality from sample 1200M\_Ti

The most conventional map to use is however an inverse pole figure, shown in Figure 13. This map clearly shows the difference between grains, each color representing a crystallographic orientation. In the bottom right corner the legend indicates the extreme orientation in each direction. The map quality is sufficient for locating specific grains where further testing can be performed. Employing a script it is possible to ask the system to

highlight the grains which are within a given deviation of  $5^\circ$  from a specific orientation. Figure 14 is an illustration of this done for the orientation (5 2 11).

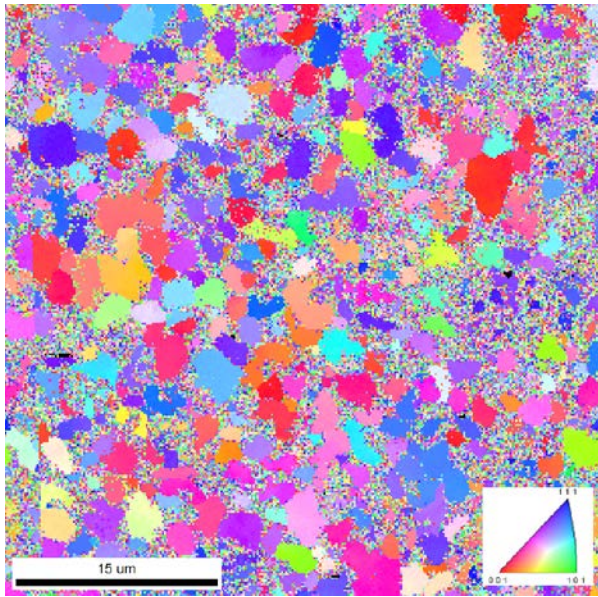


Figure 13 – Inverse pole figure from sample 1200M\_Ti

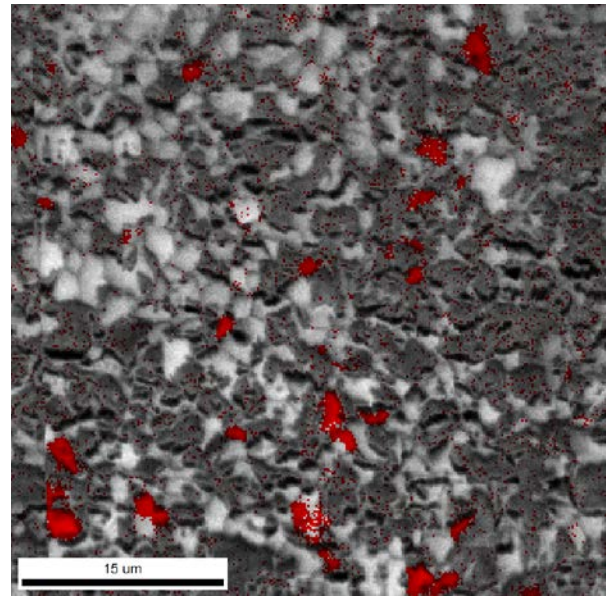


Figure 14 – (5 2 11) orientated grains from sample 1200M\_Ti

### 5.3.2 Orientation selection process

The choice of which orientation the nano-structures are to be made in is an important choice for ensuring the tests can give proper results. The orientation of choice would be one to provide single-slip mechanisms during compression testing. Using software provided by Post Doc. Afrooz Barnoush, GrainFinder and ShowSlipSystem, the maps are exported into files where the orientation in each point is enumerated. Inserting these numbers in ShowSlipSystem, a visualization for the slip-systems in the grain in Figure 15 is shown in Figure 16. The crossroads indicate the possible slip systems, and the color of the bands indicates the stress level in each point. The crossroad on the bottom right is notably redder than the others, indicating that this slip system should be activated before any other, meaning single slip. As this was found to be the case for all the (5 2 11) oriented grains these were selected for the production of nano-specimens.



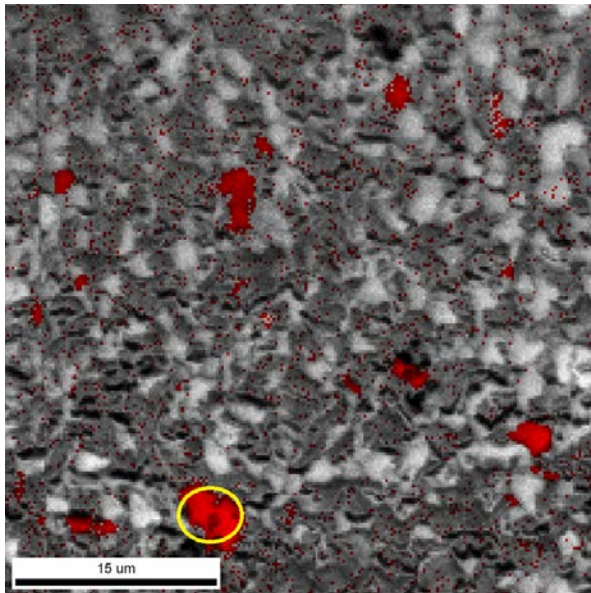


Figure 15 – (5 2 11) grain from sample 1200M\_Ti

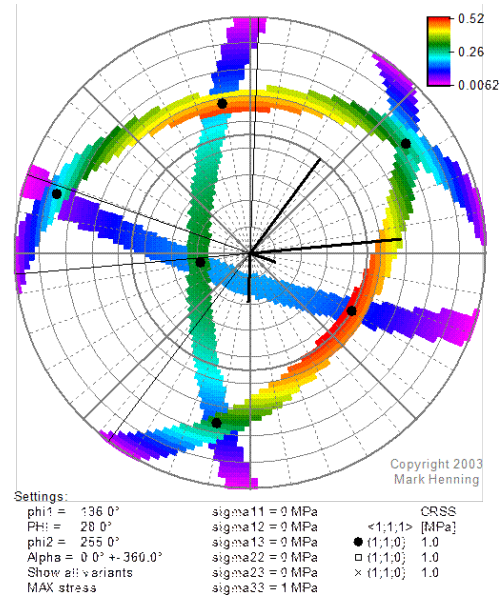


Figure 16 – ShowSlipSystem 2D for selected grain from sample 1200M\_Ti

## 5.4 Focused Ion Beam pillar milling

Once the EBSD maps have been analyzed and the grains for pillar production have been selected, it is time for the milling of the pillars. This has been performed using the FEI Helios DualBeam FIB at NTNU Nanolab. The sample is stuck to a FIB stub using carbon tape, which is used for its conductivity. Then it is mounted on the stage and inserted into the chamber, which is next pumped to a vacuum state. Similar to the tool used for EBSD, an initial calibration of settings such as the acceleration voltage is made. Next the system is calibrated such that both beams are directed at the same point on the sample surface, independently of how much the stage is tilted. This specific height is known as the eucentric height, and allows the user to view an area with the SEM before machining it with the FIB.

First, the scanned area where the EBSD maps have been made must be found. The scanned area from the EBSD is shown in Figure 17, where the selected grains have also been marked. In Figure 18 the same area has been relocated using the SEM of the DualBeam. The same grains have been marked with the number of the pillar which is about to be milled. The surface is tilted 52°, and navigating the maps is made possible by going from one characteristic grains to another.

When the grains have been found and the beams are well aligned, the next step is deciding the milling parameters. These are the acceleration voltage in kV, the beam current in nA, outer and inner diameter of the pattern in μm, the z value in μm which specifies how deep the milling will be, choosing whether the milling direction is from the inner or the outer diameter and finally the dwell time of the beam in seconds. Depending on what material and microstructure the sample has, these differ a lot, and must in general be adjusted to each type of grain. Even for the same orientated grains milling with the same parameters might result in different looking pillars. This effect is shown in Figure 19, Figure 21 and Figure 22, where the same parameters were used. Figure 20 also illustrates that additional steps can be

taken to clean up around the pillar, but this increases the chance of ion-damage to the resulting pillar.

The risk of having ions damage on the surface increases with higher beam currents, which is why the current is lowered for the final step of pillar production. It also depends on how the lattice structure is oriented, as there in some cases are easier for the  $\text{Ga}^+$  ions to penetrate deep into the material (known as tunneling), rather than having a good sputtering effect near the surface. A third factor which affects ion damage to the pillar is how accurate the FIB itself is focused. The correct focus must be found for the relevant current both to achieve cleaner structures and to minimize ion damage to the structures.

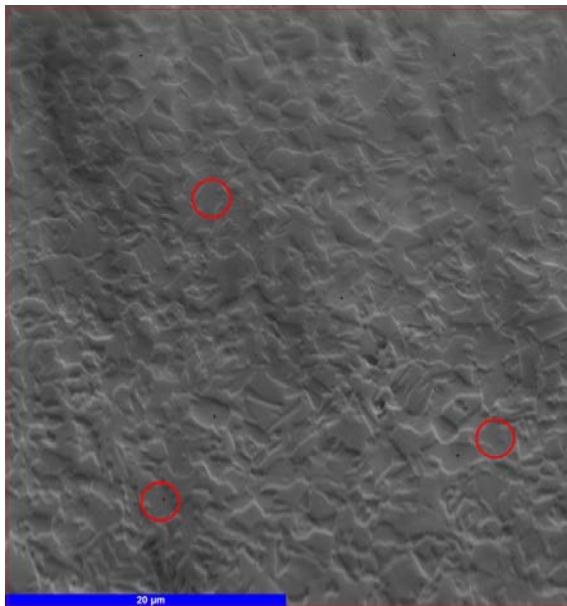


Figure 17 - EBSD-scanned area from sample 1200M\_Ti

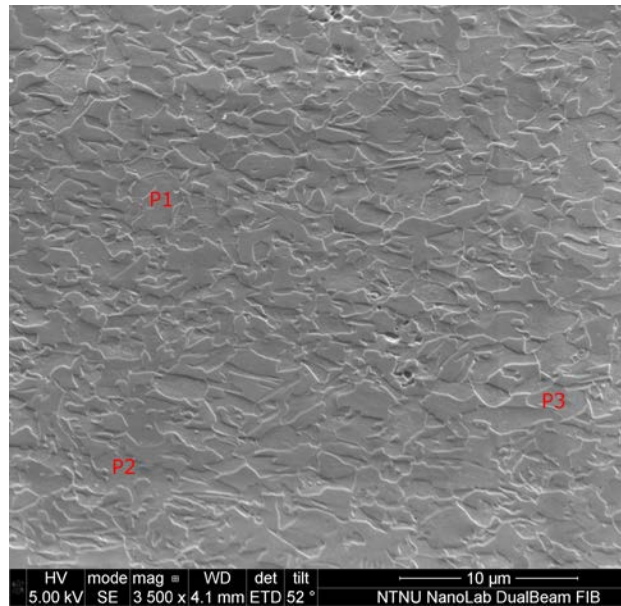


Figure 18 - Same area, tilted 52° in FIB from sample 1200M\_Ti

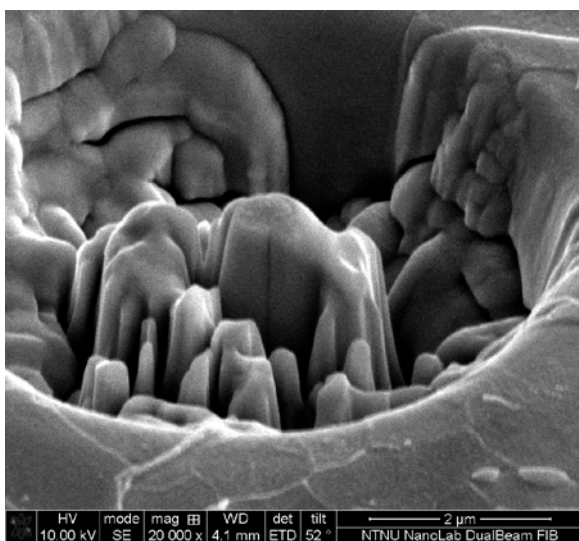


Figure 19 - Pillar G1 from sample 1200M

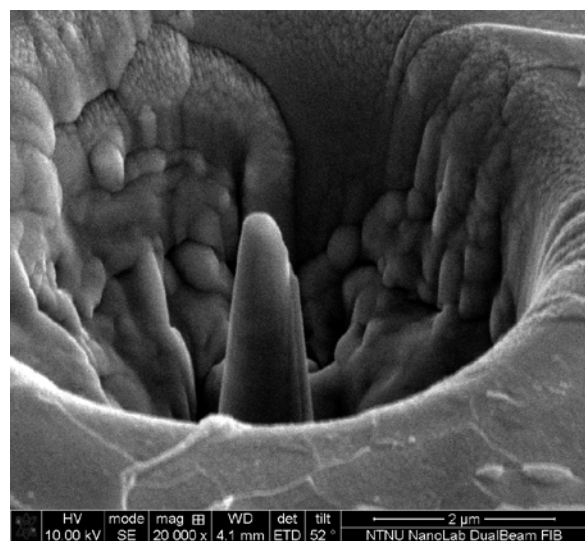


Figure 20 - Pillar G1 after cleaning steps

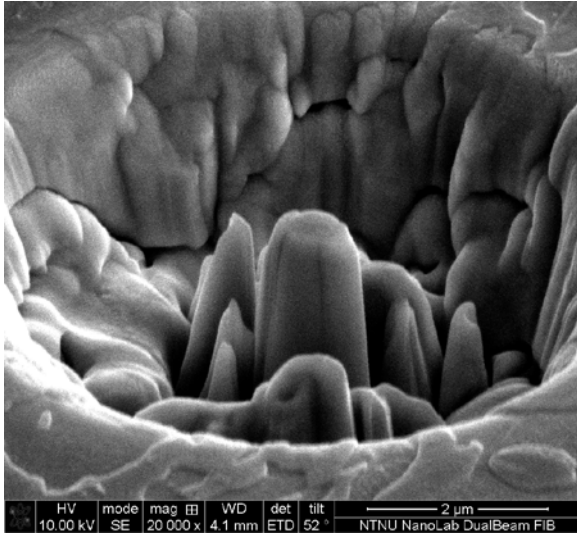


Figure 21 - Pillar G2 from sample 1200M

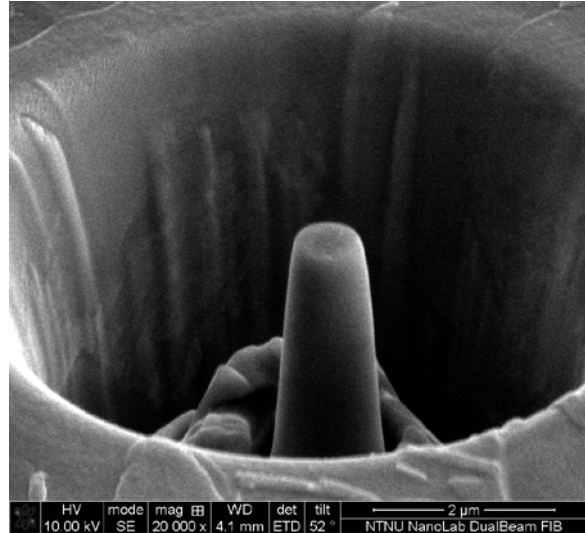


Figure 22 - Pillar G5 from sample 1200M

The main reason for the difference between these three pillars is that they are made in different grains, although all in ferrite. As grains are three-dimensional and the EBSD maps only shows two dimensions, there is always an uncertainty of how the grain continues under the surface. In order to minimize the risk of a grain ending immediately below the surface, it is beneficial to select larger-looking grains. In some cases the surrounding grains will also decide how deep the crater around the pillar will be. This effect can be seen in Figure 21 and Figure 22, where the former display a lot of material still present and the latter a deeper crater.

Another way to reduce this problem of varying grain properties is of course to choose grains with the same crystallographic orientation. As explained in the previous section about EBSD the (5 2 11) orientation of ferrite grains was selected for nanopillar production. After some testing, the parameters in Table 3 were chosen to use for pillar production, as they resulted in pillars with a good height to diameter ratio of between 2 and 2.5. An example of these pillars is provided in Figure 23.

Step	Voltage (kV)	Beam current (nA)	Outer (μm)	Inner (μm)	z (μm)	I/O	Dwell (ms)
I	30	9.3	15	4	1.34	IO	0.001
II	30	0.28	6	1.2	0.17	OI	1
III	30	0.28	4	1.2	0.17	OI	1

Table 3 - Pillar production parameters used for samples 1200M's and 1400M's

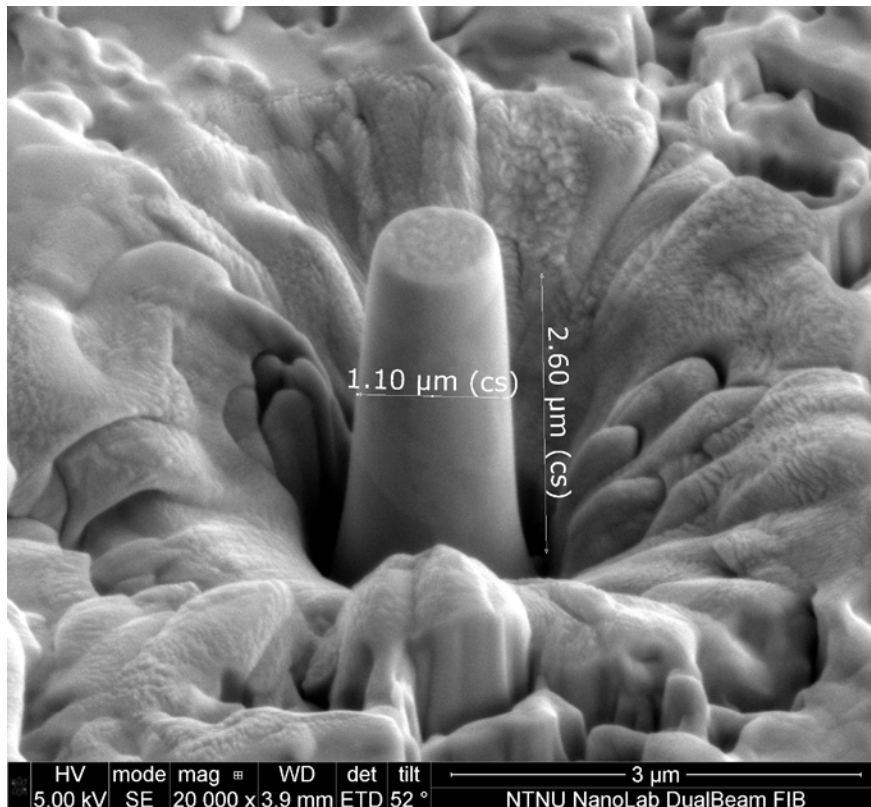


Figure 23 - Correctly milled pillar from sample 1200M

## 5.5 Nanomechanical indentation

### 5.5.1 Indenter setup

Nanomechanical indentation was used for both surface indentations and pillar compressions in this thesis. The samples are placed on the stage inside the Triboindenter TI950, at the Nanomechanical lab at IPM, NTNU. The system has to be calibrated before usage, to check for any drift and confirm a good tip-to-optic calibration is in place. The latter means that viewing a certain point in the optic should result in hitting that exact point with the tip when changing between the optic microscope and the tip. As discussed in the theoretical part, a Berkovich tip is used for the surface indentations while a 3 μm flat tip is used for compression of the approximately 1 μm diameter pillars.

Alongside the choice of tip, choosing the correct load function is an important parameter. Whether the load function should be load-controlled or displacement-controlled depends on how strain-dependent the material is, as some materials show an increase in sensitivity as a result of displacement-controlled testing. Figure 24 displays such a load function, the one used for most of the pillar compression testing throughout this thesis. A maximum displacement of 300 nm is chosen as this is just above 10% strain in the pillars. The load function used for surface indentations was on the other hand load-controlled, as shown in Figure 25. This test is performed quite quickly with a high maximum load of 10 000 μN. There has also been added an additional segment where the load is kept constant before the final unloading. This is done so that any drift can be seen directly in the resulting load-displacement curve. In both figures, the loading part of the curve is colored red.

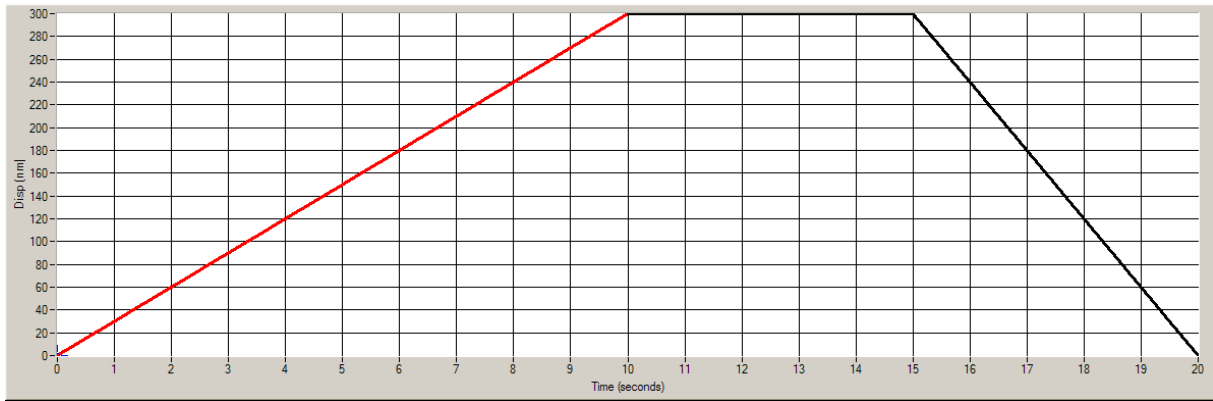


Figure 24 - Load function used for pillar compression, displacement-controlled

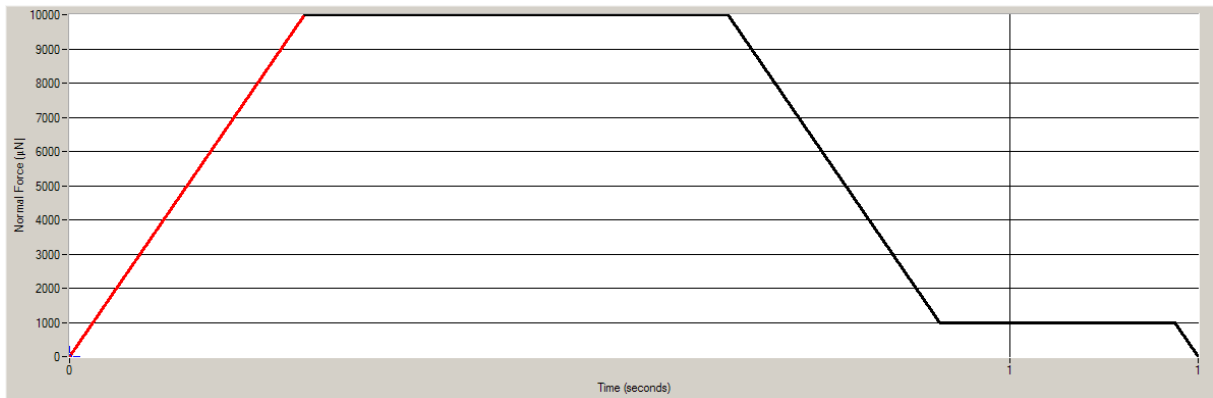


Figure 25 - Load function used for surface indentations, load-controlled

Locating and hitting the pillars is another challenge, where the main objective is avoiding hitting the crater wall around the pillar, and hit only the pillar itself. To achieve this, a good tip-to-optic calibration must first be performed. Then the pillar can be well centered from the optics before switching to the tip. Next a scan can be done by the tip itself to verify the pillar is in the center of where the indentation will be done. A complete scan like this is represented in 3D in Figure 26. As the crater around the pillars have been made approximately  $15\mu\text{m}$  in diameter and the tip is  $3\mu\text{m}$  this centering should be adequate.

A problem associated with a complete scanning of the pillar, is that it might hurt the pillar edges. This was found in several pillars, and can be seen in Figure 27 at the edges around the tip of the pillar. As this was discovered on several pillars, the solution became to only scan a few lines before compression. This would verify the pillars centration and minimize the damaging effect of the scan to the pillar. Other measures were also taken, such as decreasing the scan speed and lowering the set point of the system.

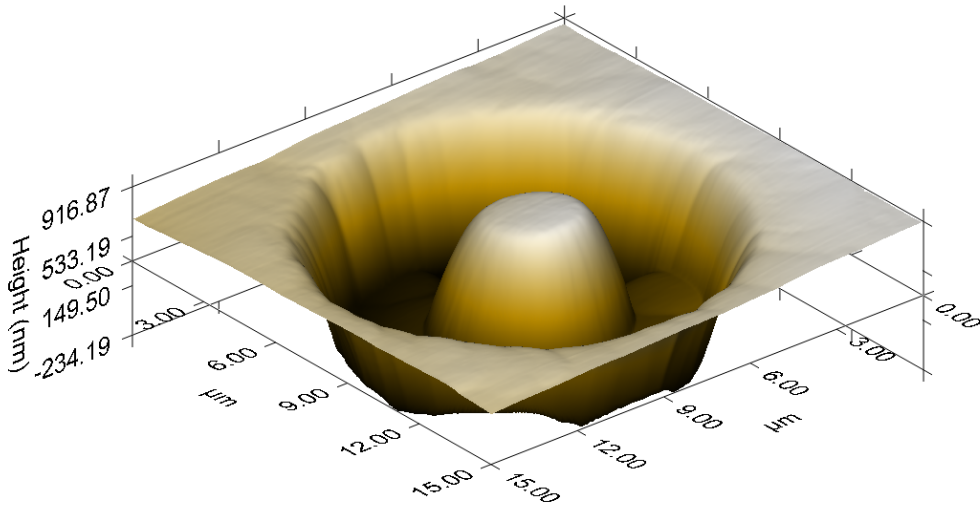


Figure 26 - 3D surface scan of P19 pre-compression on sample 1400M\_Ti

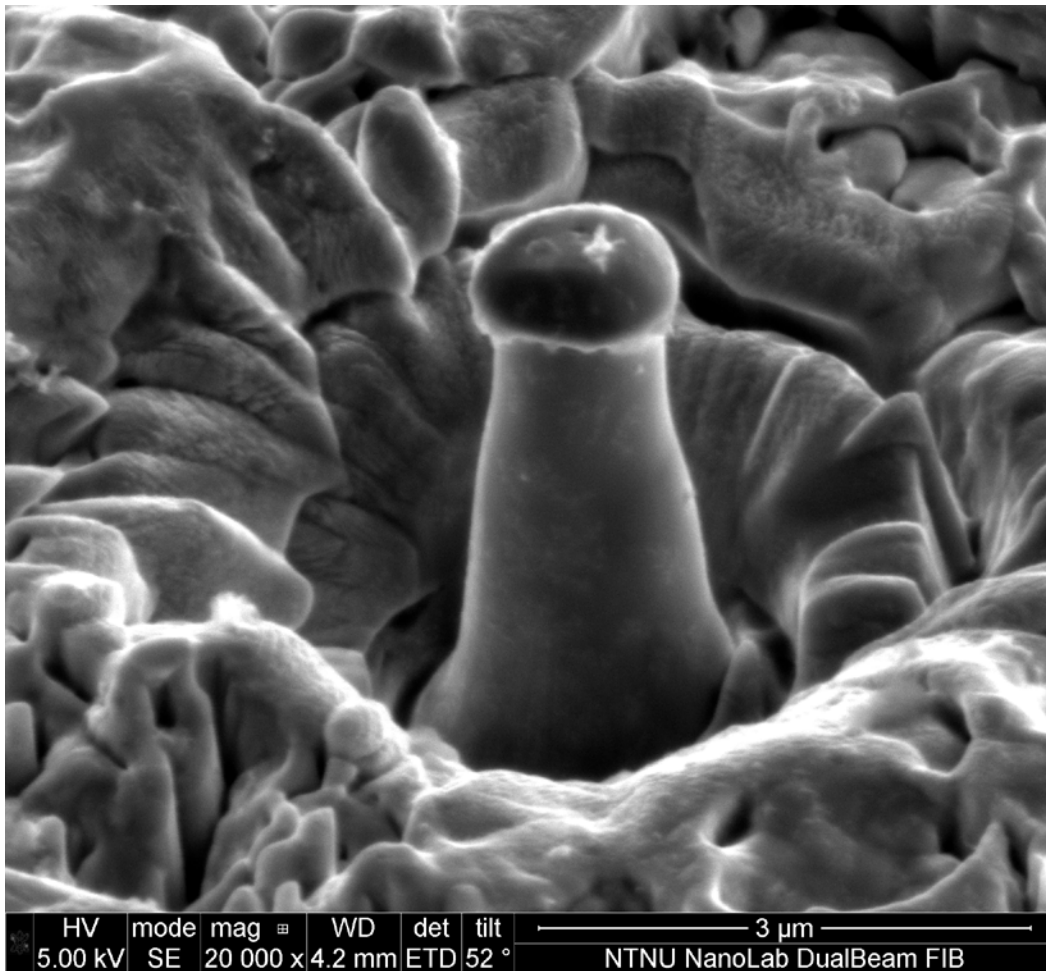


Figure 27 - Pillar P18 after surface scanning and compression of sample 1400M

### 5.5.2 Electrochemical nanoindentation setup

The electrochemical setup was done together with PhD. Adina Basa and Post Doc. Afrooz Barnoush. The setup, a three-electrode electrochemical, is based upon the same method used by Asgari et al (26) and developed at NTNU (27). The counter electrode used was a platinum wire and the reference electrode a saturated calomel electrode. The potentials stated in this thesis are all referenced to this electrode. The working electrode was the sample holder, and for controlling the electrochemical potentials a Gamry Reference 600 Potentiostat was used.

The samples are charged with hydrogen in situ as the sample is completely submerged in an electrolyte. The custom made sample holder for this usage is shown in Figure 28. It has to ensure there is no leakage of the electrolyte onto the stage, while at the same time ensuring that there is current connecting from the metallic part to the sample itself. The tubes which can be seen entering the sample holder are to control the flow of electrolyte, refreshing it when needed and always ensuring the sample is sufficiently submerged. The electrical connections complete the setup with connections to the potentiostat and the reference electrode.

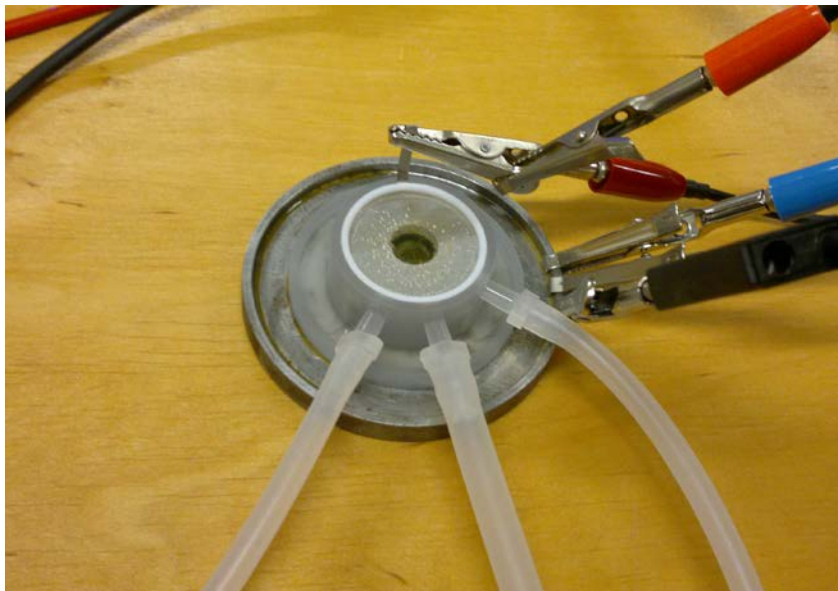


Figure 28 - Custom sample holder complete with tubes and electrical connections

The entire system, including sample holder and tubes, has to be cleaned thoroughly before each set of testing. This is important to avoid contamination which will affect the results. First all of the tubes involved are rinsed with double distilled water several times before they are left to dry. The Teflon piece is first put in a UV-bath containing equal amounts of ethanol and acetone for 5 minutes. Next, it is joined by the O-ring and the platinum plate to be cleaned thoroughly with double distilled water before they are put into  $\text{HNO}_3$ . They are left in the acid for 5 minutes, before they again are cleaned with double distilled water several times. They finally undergo a UV-bath with double distilled water before all the components are dried using a hairdryer.

The choice of electrolyte is important as it affects how much hydrogen that enters the material. For the first sets of surface indentation a Borax buffer was used of 0,05M

$\text{Na}_2\text{B}_4\text{O}_7 \cdot 10\text{H}_2\text{O}$  with a measured pH of 8.09. As the results indicated small or no hydrogen influence, this was replaced by another electrolyte to enhance the hydrogen diffusion into the material. This electrolyte was 0,05M  $\text{K}_2\text{SO}_4$  with a measured pH of 6.22 and was prepared with the help of PhD. Adina Basa.

### 5.5.3 In situ electrochemical testing

The first surface indentation tests were done with the Borax buffer switching between a galvanostatic experiment, that is constant current and potentiostatic, which is constant voltage. The current was switched between -0.65 mA which corresponds to a voltage of approximately -1.7V cathodic potential and a voltage of -0.5V, which corresponds to a current just below 0A, which gives an anodic potential. This provided multiple series of indents performed under both cathodic and anodic charging. As these tests did not demonstrate a hydrogen effect certain changes were made to the setup.

Firstly, the electrolyte was changed from Borax to potassium sulfate to enhance the hydrogen flow into the sample surface. Secondly the samples were left for an hour under cathodic charging to ensure enough hydrogen dissolved into the material. As this appeared to show an effect for the 1400M pillars, this method was used for the 1200M pillars as well.

Lastly a more experimental method was developed and tested in cooperation with Post Doc. Afrooz Barnoush. Using a very slow strain rate (1nm/s) displacement controlled testing was performed on single pillars while switching between cathodic and anodic charging. The load function used is shown in Figure 29. This testing assumes the hydrogen effect to manifest very quickly, but has the advantage of removing any scattering which might be caused by differences from pillar to pillar (such as grain boundaries and pillar geometries).

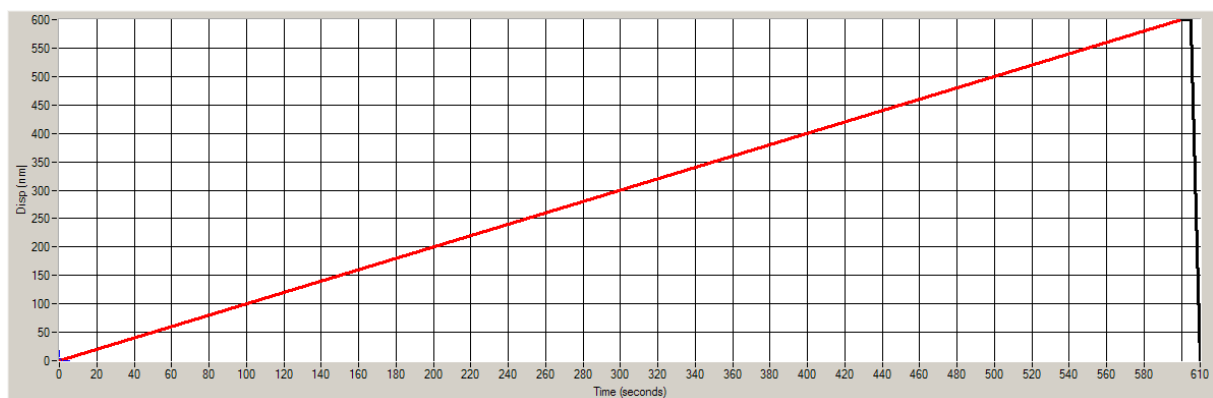


Figure 29 - Load function for slow displacement-controlled pillar compression

Figure 30 shows the stress-strain curve of a pillar on sample 1400M where this method was initially tested. The charging was switched at every 100 seconds, corresponding to each 100nm of the pillar displacement. It started with anodic (around -1V) for the first period, before going to cathodic (-1,6V) and switching back and forth during the compression. In Figure 30 this is represented with a green line for when the anodic potential is applied and a red one for cathodic potential. The intended applied voltage is plotted in Figure 31. There



was however problems with the first version of the software Gamry Instruments Virtual Front Partner, and as a result the switching was not controlled optimally, and the sample corroded in the end. Upon receiving an update from the software producer this problem was solved and an initial round of testing was performed, which will be presented in the next chapters.

The investigation of hydrogen can be performed after the elastic part of the curve, in the strain hardening region. This part is zoomed in on and shown in Figure 32. The compression performed from 100-200, 300-400 and 500-600nm was done under cathodic charging. Although there are no significant changes, there at least appears to be a tendency of a slower loading rate for the cathodic periods, specifically the period between 300 and 400nm, corresponding to the second period of cathodic potential.

### P26 on sample 1400M

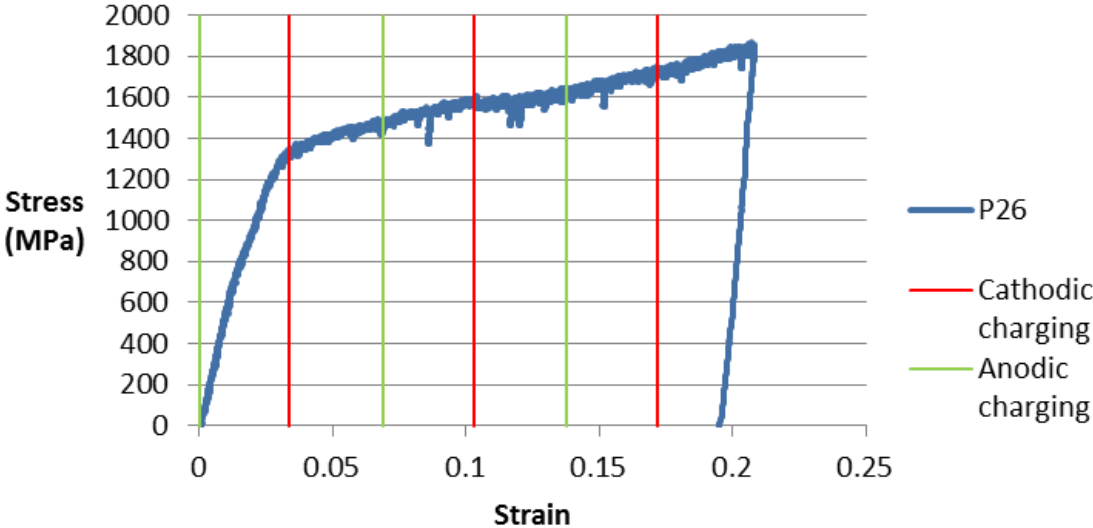


Figure 30 - Load-displacement curve of pillar P26 from sample 1400M

### Voltage during compression of P26

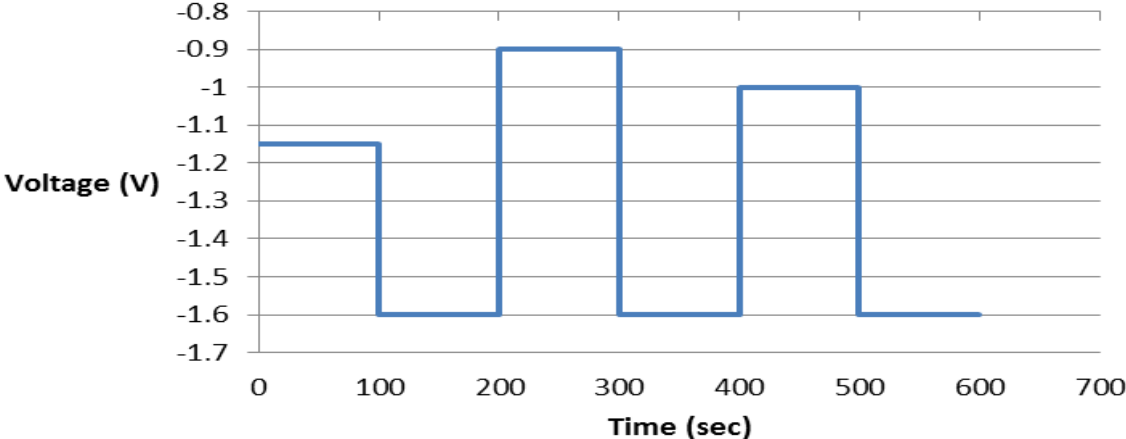


Figure 31 - Applied voltage during compression of P26

## Strain hardening of P26

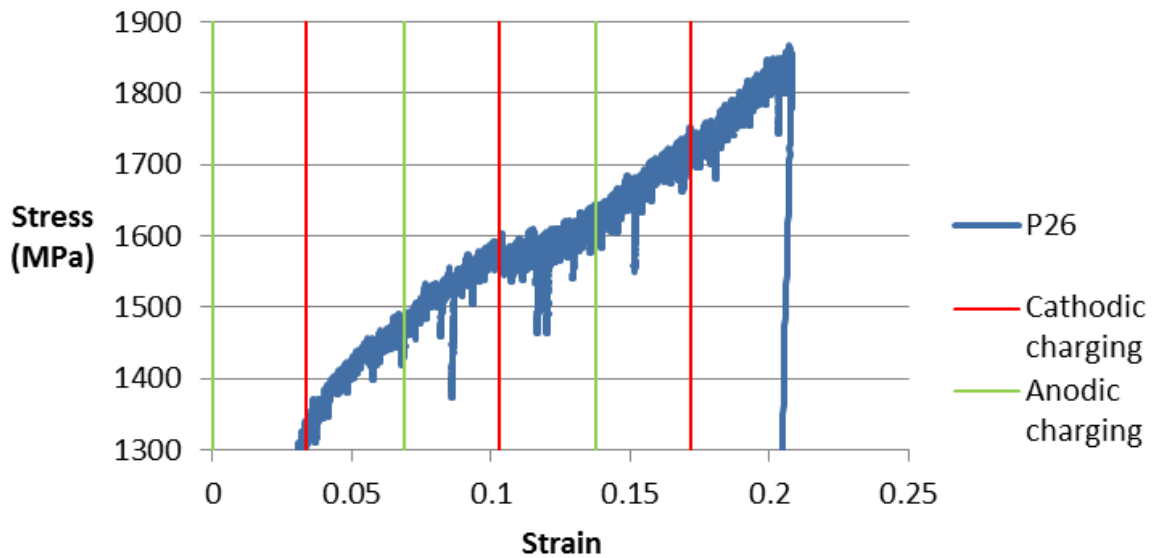


Figure 32 - Load-displacement curve zoomed in for pillar P26 on sample 1400M

In the case that the hydrogen effect doesn't manifest quickly enough another load function was prepared, as shown in Figure 33. This load function has holding segments, marked in green, to allow the hydrogen time to infiltrate/exit the sample each time. This maintains the bonus of receiving results from a single pillar, thus excluding a potential factor for scatter.

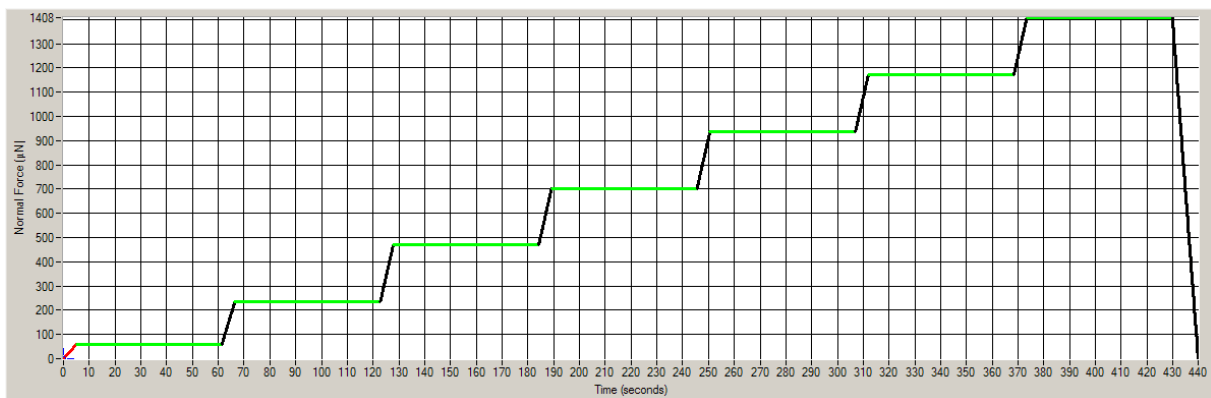


Figure 33 - Load function with holding segments for displacement-controlled pillar compression

All the pillars compressed using this method, are represented in the Appendix by their stress-strain curves including the markings of when the potential is anodic and when it is cathodic. All pre- and post-compression images are also included there.

## 5.6 Post-compression imaging

For investigation of the deformed pillars, images are captured using the SEM of the FIB used for milling the pillars. Once the samples have been submerged in electrolyte, they are contaminated and require a thorough cleaning immediately after testing. This notion was verified after compression of the first pillars. Figure 34 and Figure 35 both show the same area for before and after compression, respectively. From the post-compression image a charging on the surface is visible which, in addition to hindering the view physically, causes an effect where the SEM-images are inaccurate. This effect is illustrated by Figure 36 where the lower part of the image is clearly distorted. This is due to the effect that the charged surface has on the secondary electrons used for imaging.

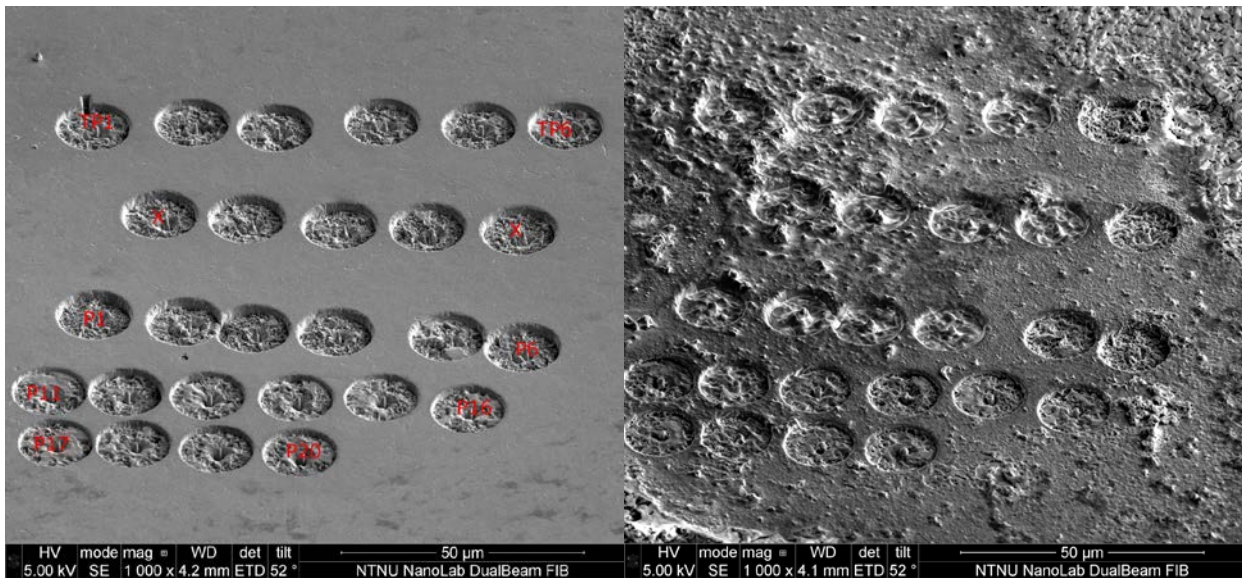


Figure 34 - Sample 1400M\_Ti surface before compression testing

Figure 35 - Sample 1400M\_Ti surface after compression testing

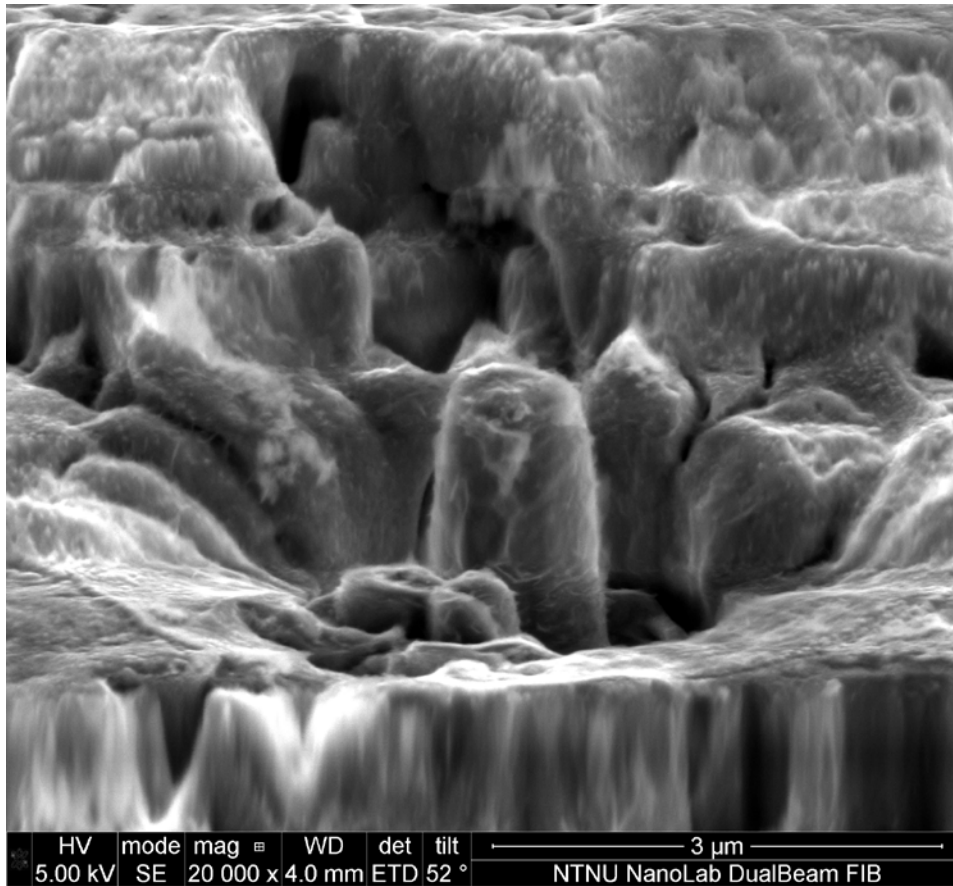


Figure 36 - Distorted image from pillar on sample 1400M\_Ti

When the sample is cleaned well enough, the post-compression images can provide valuable information, both in the case where the indenter tip did not hit exactly on the pillar top, and also reveal the slip mechanisms activated in the pillar. Figure 37 and Figure 38 are post-compression images of the correctly milled pillar in Figure 23, which shows the importance of imaging the pillars from several angles in order to get the most complete view.

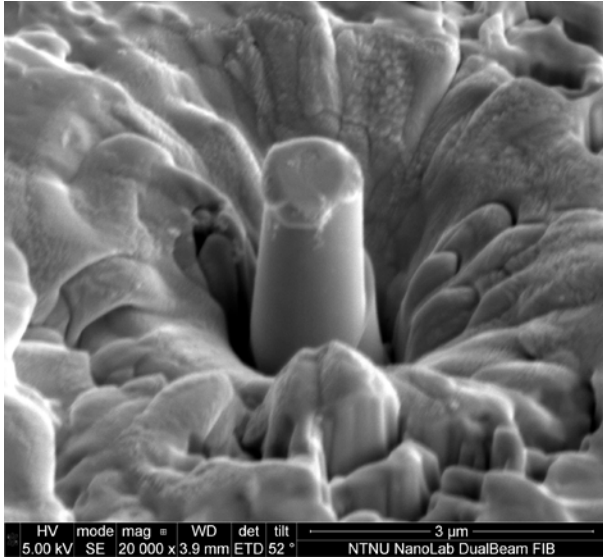


Figure 37 - Post-compression image of pillar from sample 1200M04

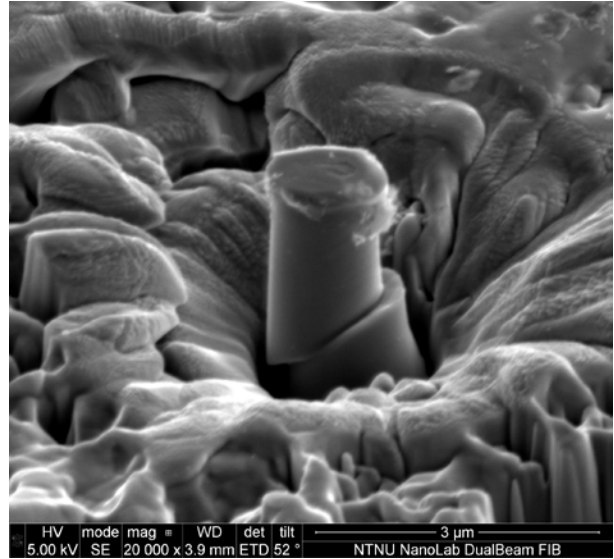


Figure 38 - Rotated view of compressed pillar from sample 1200M04

# 6 Results

---

This chapter will present the results of the work executed during this thesis. The results are related to indentation testing with and without hydrogen charging, and will be further discussed in the next chapter.

## 6.1 Surface indentations on samples 1400M

---

### 6.1.1 Indentation in air

---

Series of 100 indents were performed in air on both 1400M samples. Figure 39 provides the mean values of the hardness, derived from the unloading curve of each indent's load-displacement curve. The middle point show the mean values and the bars are the standard deviation for the results. The same representation is given in Figure 40 for the reduced modulus of the same indents. The load function used is the one in Figure 25.

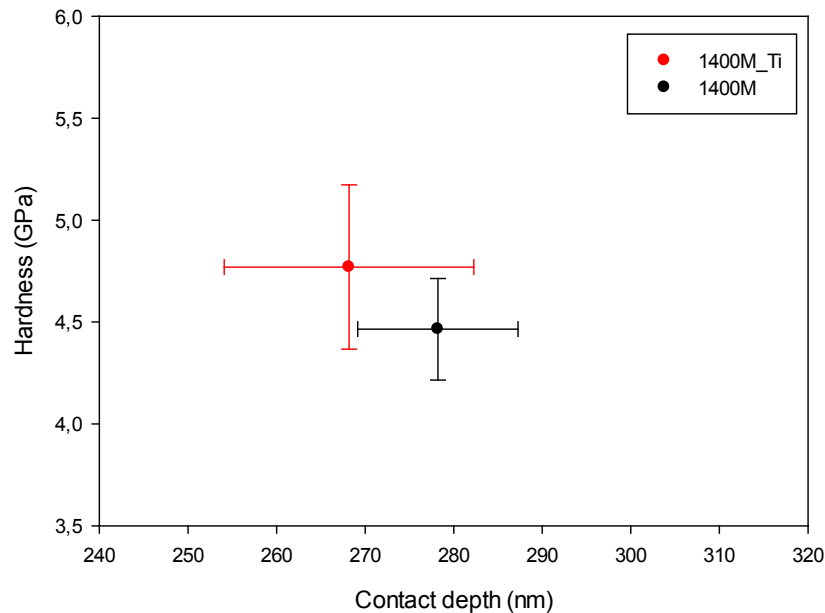


Figure 39 - Series of 100 surface indents on both 1400M samples: hardness

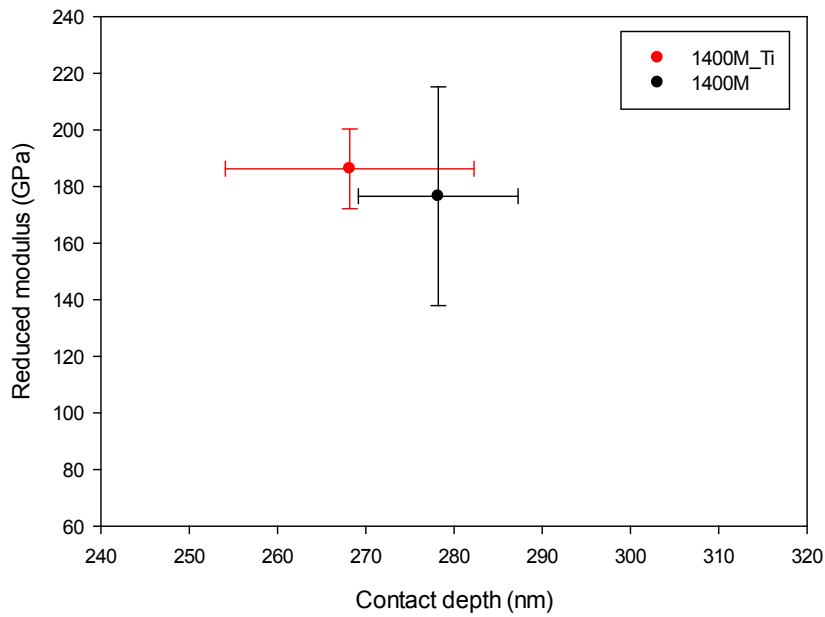


Figure 40 - Series of 100 surface indents on both 1400M samples: reduced modulus

### 6.1.2 Indentations in air and with hydrogen charging

Series of 25 indentations were performed first in air, then with cathodic charging of -1710mV, and lastly with anodic charging of -500mV. The results are plotted as in the previous section, where the mean values are the points and the bars represent the standard deviation of the values. Figure 41 shows the results from sample 1400M\_Ti, while Figure 42 shows the results from sample 1400M. The load function used is the one in Figure 25.

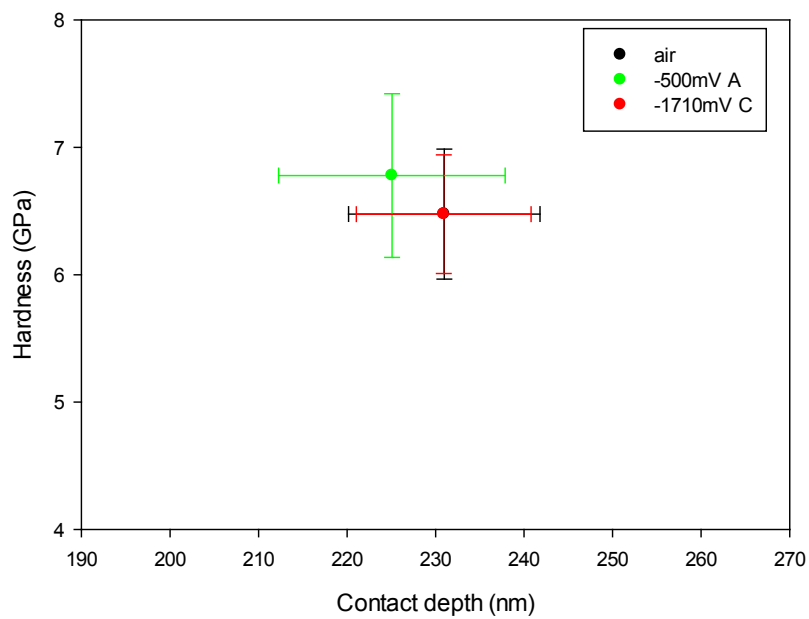


Figure 41 - Series of 25 indents under electrochemical indentation: hardness of 1400M\_Ti

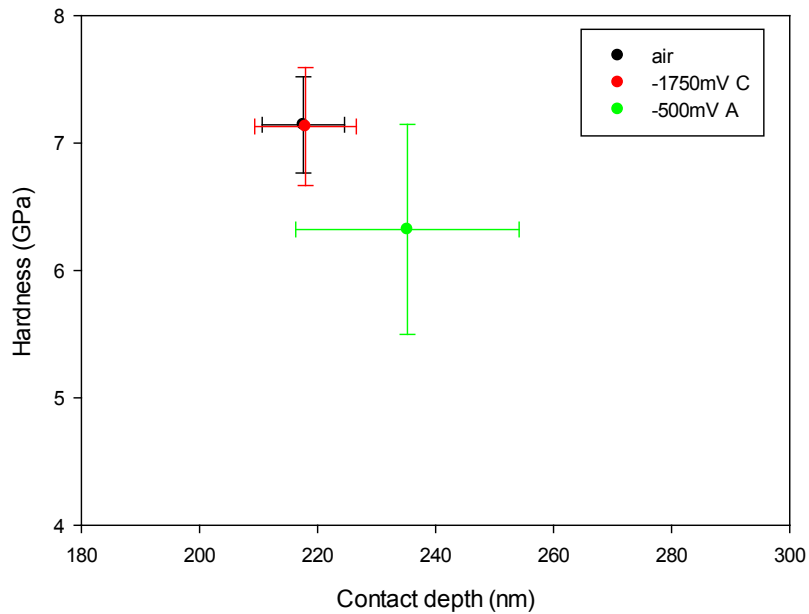


Figure 42 - Series of 25 indents under electrochemical indentation: hardness of 1400M

## 6.2 Pillar compression on samples 1400M

---

10 pillars of diameter  $1\mu\text{m}$  were milled in martensitic grains on both the 1400M samples. Of the 10 pillars 5 were compressed in air and 5 with hydrogen charging. From the resulting stress-strain curves a curve fitting was performed for each set of 5 compressions. The stress-strain curves for each set including the curve fitted plot is included in the Appendix, but for illustration the 1400M\_Ti set is shown in Figure 43. The dashed lines are pillars compressed with hydrogen, and the blue line is the curve fitted plot. The fitting was performed as explained in section 4.7.



## 1400M\_Ti Pillar compression with H

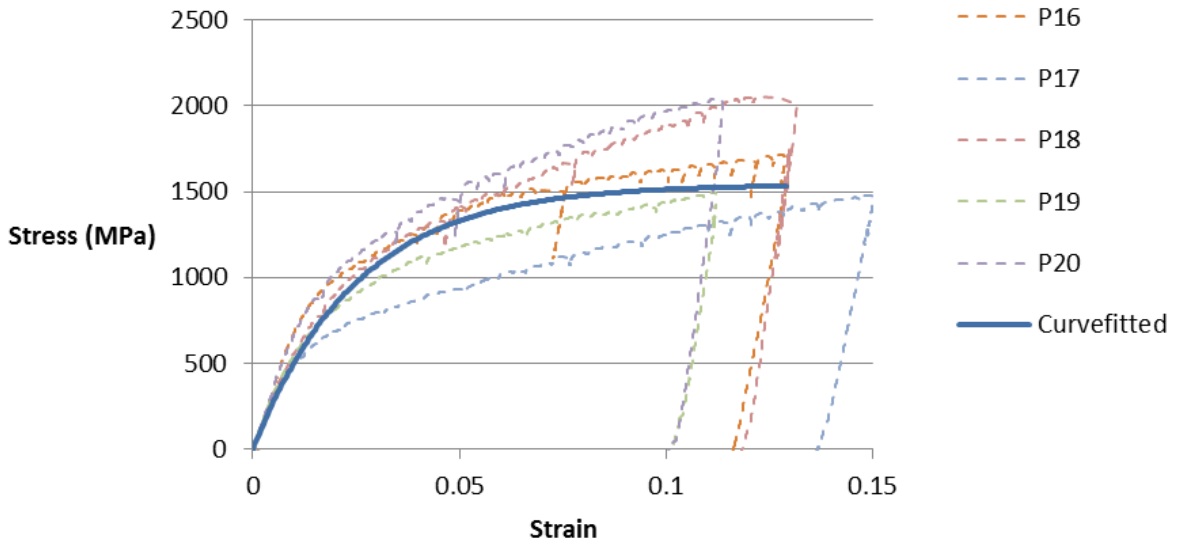


Figure 43 - 1400M\_Ti pillars compressed with H

Figure 44 presents the curve fitted plots for the 1400M samples for both air (straight lines) and hydrogen charging conditions (dashed lines).

## 1400M pillars curvefitted

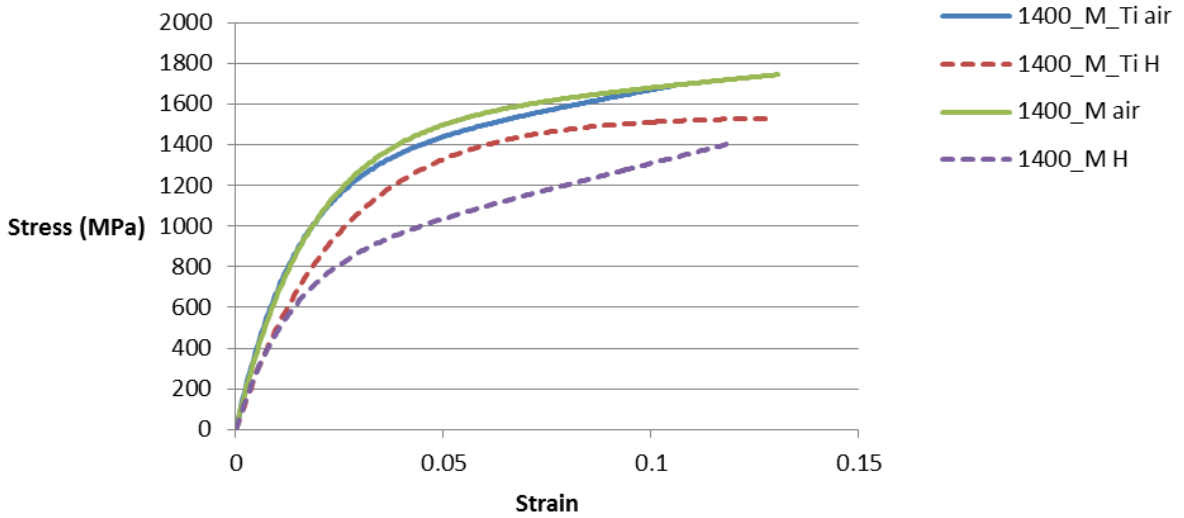


Figure 44 – Curve fitted plots from 1400M pillar compression

From the pillars' stress-strain curves some material properties were extracted and averaged over each set of 5 compressions, as tabulated in Table 4. The yield strength was found by using the data point closest to 2% strain, and the hardening was found by calculating the difference in stress for 2 and 10% strain.

Sample	Yield strength at 2% strain (MPa)	Hardening (MPa)	Condition
1400M_Ti	1073 ± 93	616 ± 65	Air
1400M_Ti	885 ± 122	746 ± 182	H
1400M	1147 ± 106	578 ± 47	Air
1400M	786 ± 264	519 ± 176	H

Table 4 - Material properties for 1400M samples from pillar compression

### 6.3 Pillar compression on samples 1200M

12 pillars of diameter 1µm were milled in grains of orientation (5 2 11) on both the 1200M samples. Half of them were compressed in air and the rest with hydrogen charging. The resulting stress-strain curves included the curve fitted plots are shown in Figure 45 for sample 1200M under hydrogen charging. The blue line is the curve fitted plot, and the other plots are included in the appendix.

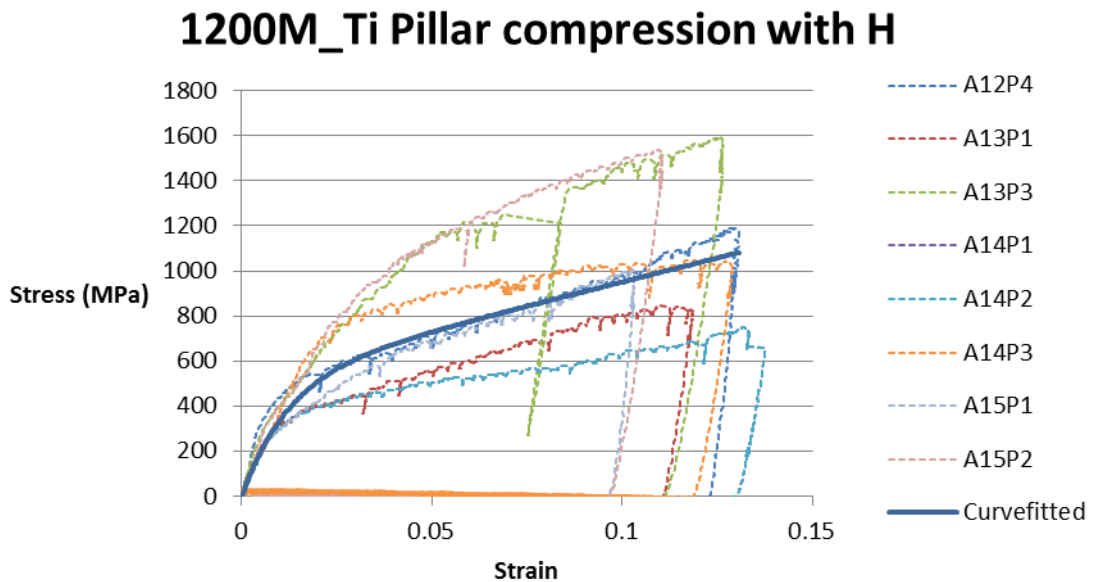


Figure 45 – 1200M\_Ti pillars compressed with H

Figure 46 shows the curve fitted plots for both 1200M samples together, where the dashed lines represent the curve fitted plots of the pillars compressed with hydrogen.

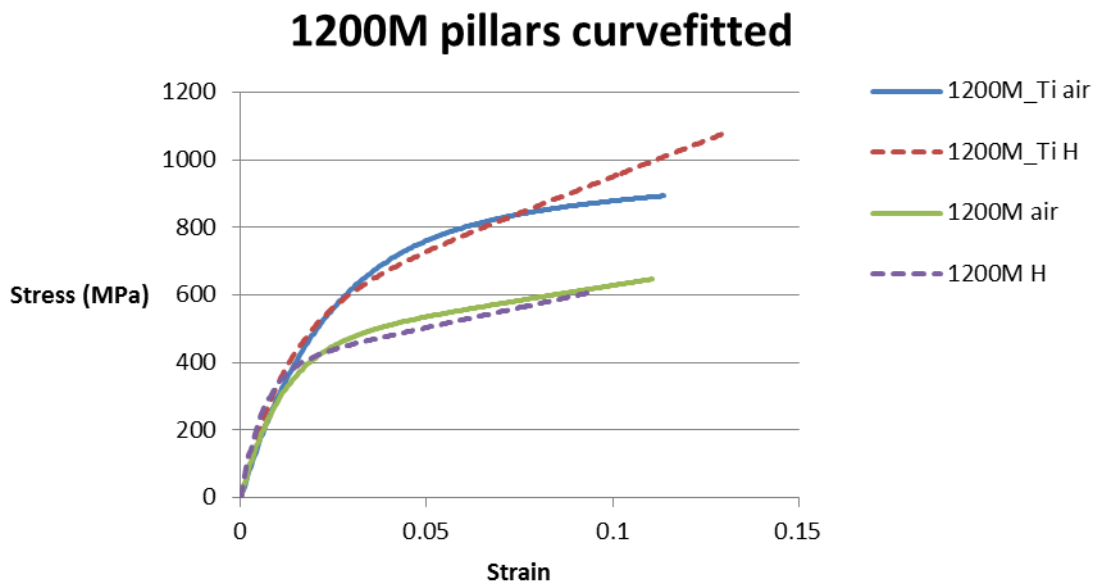


Figure 46 - Curve fitted plots from 1200M pillar compression

Like with the 1400M samples, some material properties have been derived from the stress-strain values of the pillar compressions. Both the yield strength and the hardening values are tabulated in Table 5.

Sample	Yield strength at 2% strain (MPa)	Hardening (MPa)	Condition
1200M_Ti	509 ± 81	435 ± 158	Air
1200M_Ti	510 ± 125	484 ± 215	H
1200M	462 ± 130	230 ± 96	Air
1200M	442 ± 76	208 ± 124	H

Table 5 - Material properties for 1200M samples from pillar compression

#### 6.4 Experimental pillar compression on samples 1400M, changing potentials

As explained in the Experimental chapter, a new method for compressing single pillars with differing potentials was developed in cooperation with Post Doc Afrooz Barnoush. Figure 47 - Figure 52 shows some of the resulting stress-strain curves for the 13 pillars compressed on sample 1400M\_Ti. All the plots are also included in the Appendix. Included in the plots are the switches in potential, marked in green for the start of anodic potential and red for cathodic potential.

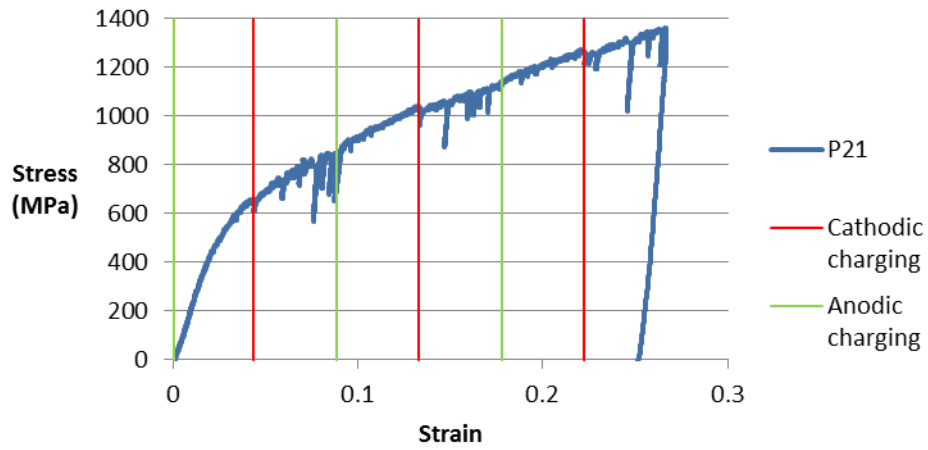


Figure 47 - Stress-strain curve of pillar P21 on sample 1400M\_Ti

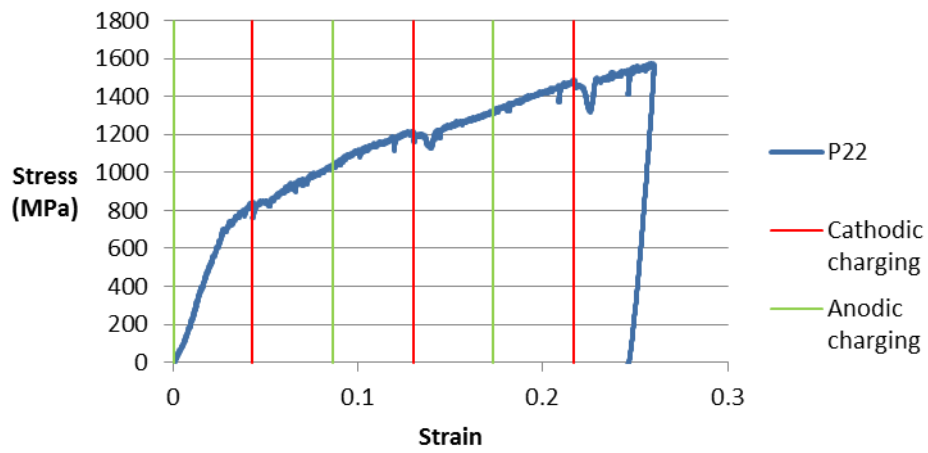


Figure 48 - Stress-strain curve of pillar P22 on sample 1400M\_Ti

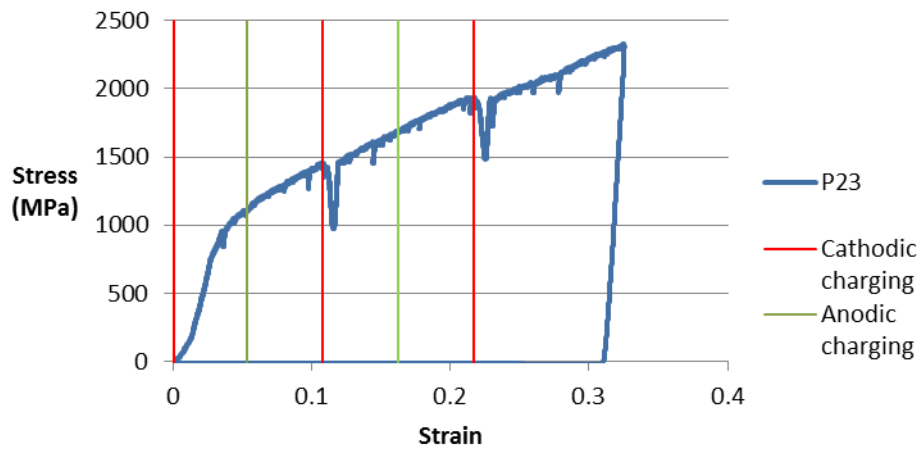


Figure 49 - Stress-strain curve of pillar P23 on sample 1400M\_Ti

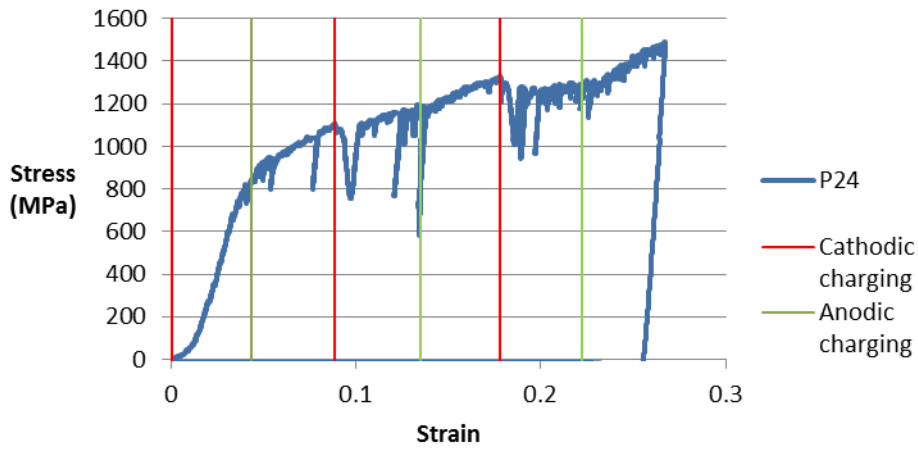


Figure 50 - Stress-strain curve of pillar P24 on sample 1400M\_Ti

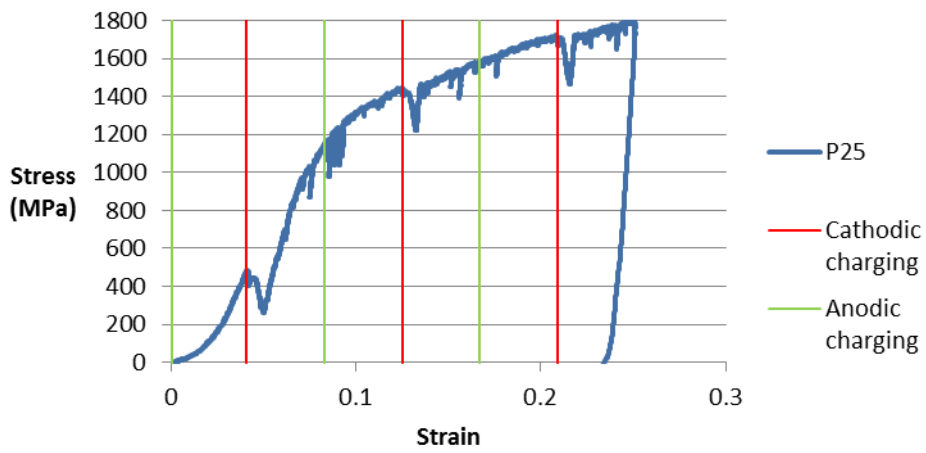


Figure 51 - Stress-strain curve of pillar P25 on sample 1400M\_Ti

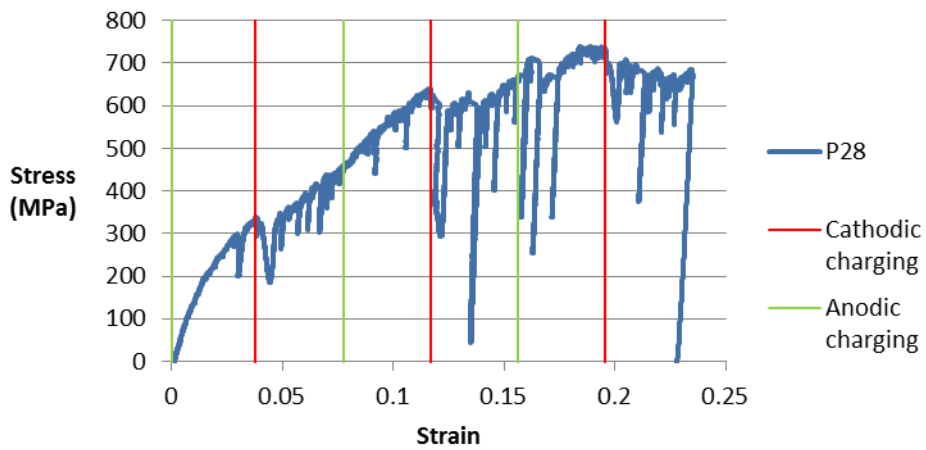


Figure 52 - Stress-strain curve of pillar P28 on sample 1400M\_Ti

Figure 53 and Figure 54 illustrate the voltage and the current as observed using the software Gamry Instruments Virtual Front Partner during the compression testing of pillar P28. The tests were performed potentiostatic; applying a constant voltage and thereby having a corresponding current. To have anodic potential -1.05V was used, and for cathodic -1.75V.

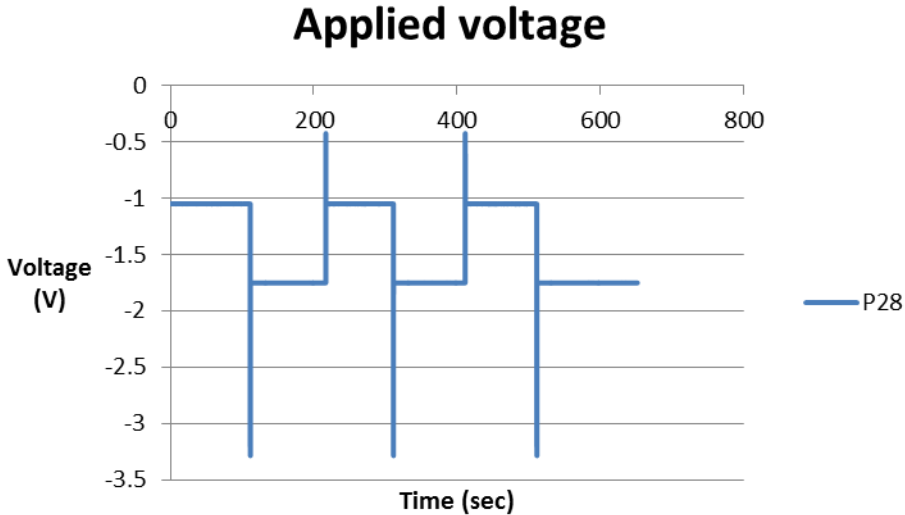


Figure 53 - Applied voltage during compression of pillar P28 on sample 1400M\_Ti

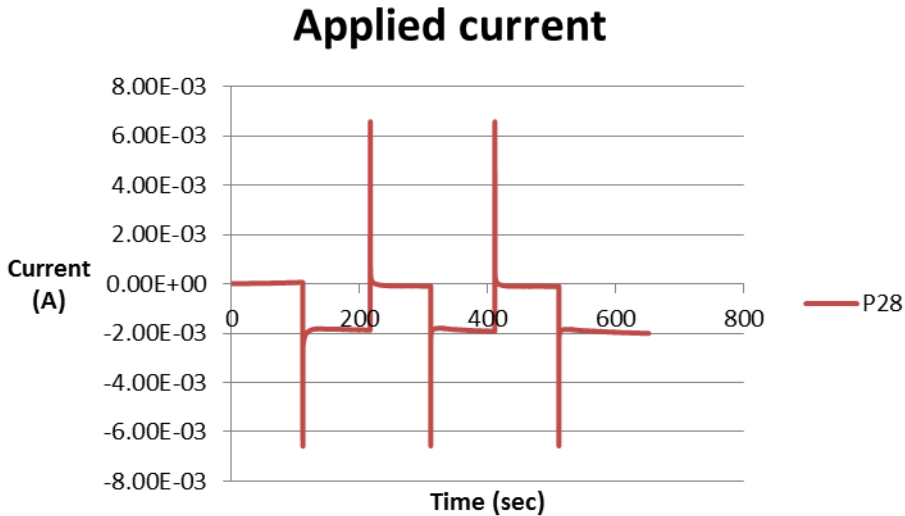


Figure 54 - Applied current during compression of pillar P28 on sample 1400M\_Ti

Figure 55 - Figure 57 shows some of the resulting stress-strain curves from the compression testing of pillars on sample 1400M. This sample had fewer good compression tests, and therefore only three are included here. All the completed tests are however presented in the Appendix.

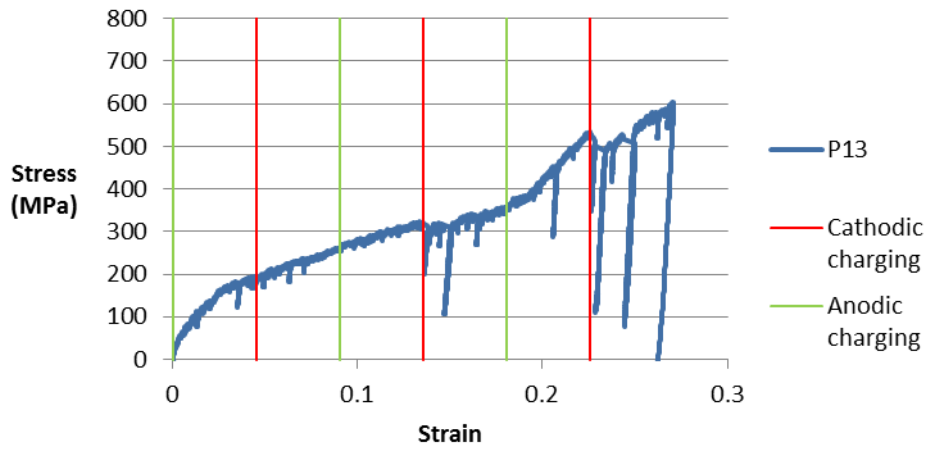


Figure 55 - Stress-strain curve of pillar P13 on sample 1400M

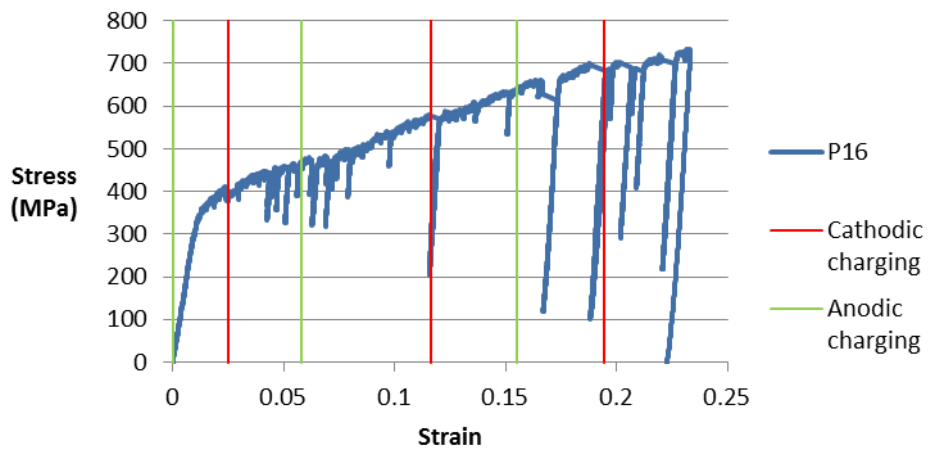


Figure 56 - Stress-strain curve of pillar P16 on sample 1400M

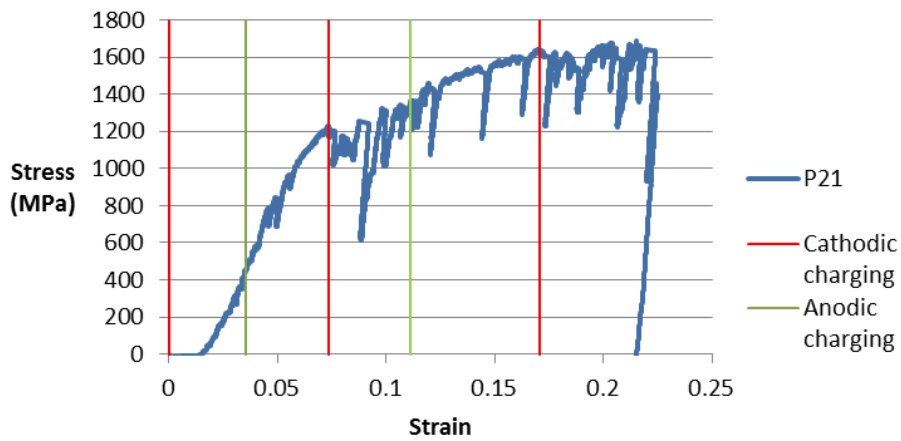


Figure 57 - Stress-strain curve of pillar P21 on sample 1400M

## 7 Discussion

---

In this chapter the presented figures and results from the last chapter will be discussed and evaluated.

### 7.1 Surface indentations on samples 1400M

---

Series of 100 indents were run in order to provide reliable results and also ensure the reproducibility of the results. This was a method for confirming that the surface preparation was done properly. As Figure 39 shows, sample 1400M\_Ti, containing titanium, demonstrates a greater hardness than the sample without titanium, which was expected. The same is shown for the reduced modulus in Figure 40, as the mean value of the sample containing titanium is higher. Although the standard deviation spread was somewhat differing, the load-displacement curves proved a good reproducibility was achieved.

The results from the series of 25 indents in air, anodic, and cathodic potential, proved somewhat unexpected. This can be seen illustrated in Figure 41 and Figure 42, where the testing in air almost exactly corresponds with the indents done while cathodic potential was applied. This would indicate no obvious effect of hydrogen. There are several possible explanations for this, the simplest one being that the hydrogen might not have had time to diffuse into the material yet. These tests were done almost immediately after applying the cathodic potential. Another potential explanation is the use of a Borat buffer, which might not be the best electrolyte for enhancing the hydrogen diffusion into the steel. On the other hand, the results from the indents performed during anodic potential are differing; the sample with titanium shows an increase in hardness and the sample without shows a decrease. This is a surprising observation, as it would be expected to see the difference for the cathodic potential instead.

### 7.2 Pillar compression on samples 1400M

---

Martensitic pillars were milled with a FIB and compressed with a flat 3 $\mu$ m diameter indenter tip. Larger grains were chosen so as to avoid grain boundaries in the pillars, but as described in the experimental part this is no guarantee. Figure 43 is a representative illustration of how the stress-strain curves are spread. The curve fitting is, as shown both here and in the other sets in the appendix a decent mean curve for comparing with the other compression data sets.

Figure 44 shows the curve fitted plots from all sets of pillar compressions, for samples with and without titanium compressed in air and with hydrogen charging. The hydrogen effect appears clearly from this figure, where both sets charged with hydrogen are clearly below the sets compressed in air. This shows they obtain the same strain at a lower stress level, again indicating weakened material hardness. What is even more evident is the difference between the two sets of each sample. Whereas the difference between the two sets compressed on 1400M\_Ti, illustrated in red and blue is visible, there is a difference of



around double magnitude for the green and purple lines, representing sample 1400M. In short, the sample without titanium appears more susceptible to hydrogen embrittlement, which would indicate that the titanium carbides have an effect on reducing the influence of hydrogen embrittlement.

The same tendency can be read and quantified from the yield strength values of Table 4. The difference of the yield strength for sample 1400M\_Ti is 188 MPa when comparing the mean values of the sets compressed in air and with hydrogen charging. The same value for the 1400M sample test sets is 361 MPa, which is 1.92 times the difference for the sample with titanium.

Another interesting notion attainable from Table 4 is the comparison of the strain hardening of the two samples. Where the hardening increases by 130 MPa for sample 1400M\_Ti upon switching from air to hydrogen results, the effect is just the opposite for sample 1400M; it decreases by 59 MPa. This change in strain hardening due to hydrogen was discussed already in 1972 by Louthan et al. (28) .

### **7.3 Pillar compression on samples 1200M**

---

After selecting grains of the same (5 2 11) orientation in the ferrite phase of the 1200M samples, pillars were cut. Ensuring the pillars were of the same orientation should make the resulting scatter less, but the scatter of these pillars proved to be bigger than the same for the 1400M samples, as shown in Figure 45. A factor which could explain this is possible grain boundaries in the pillars.

Upon comparing the curve fitted plots from each of the four sets of compressions, Figure 46 indicated almost no effect of hydrogen as the plots for samples 1200M nearly overlap each other for with and without hydrogen. The dotted lines, indicating hydrogen charging are just below for the first part of the strain hardening, but surprisingly for sample 1200M\_Ti rises above the same samples' pillars compressed in air. This is not visible for the sample without Ti.

Studying the yield strength values of Table 5, the minimal difference of the titanium sample tested in air and with hydrogen is confirmed. The titanium-free sample on the other hand has a weakening of the yield strength of about 20MPa, but given the magnitude of the standard deviation these values give no certainties. The same can be said for the strain hardening values, but here there is a clearer indication. Just like for the 1400M sample, it appears that the titanium sample under hydrogen charging has an increased strain hardening when compared to the titanium sample tested in air. For the titanium-free sample the effect is the opposite, where hydrogen charging leads to a decreased strain hardening.

The difference between the sample containing Ti and the one without is as expected, where the Ti-sample requires a larger stress to obtain the same strain levels as the one with no Ti. It is however much bigger than the corresponding difference of the 1400M samples, where the sample with and without Ti displays almost no difference.

## 7.4 Experimental pillar compression on samples 1400M, changing potentials

---

The same type of martensitic pillars as in section 7.2, were milled with the FIB and compressed using a 3 $\mu$ m diameter flat tip. The load function used is shown in Figure 29; displacement-controlled with a rate of 1nm/sec. Compressing the pillar this slow allowed switching the potential between anodic and cathodic several times. Most compressions were performed starting with anodic, but some was also initially under cathodic potentials. This is illustrated by using red lines for cathodic and green lines for the start of anodic potential in the stress-strain curves.

The first observation made, is that upon switching from anodic to cathodic potential there is an apparent drop in the stress values immediately. This can be seen in Figure 48, Figure 49 and Figure 50 in the plastic region and in Figure 51 in the elastic region. From in situ observation of the live load-displacement curves alongside the voltage and current values, it appears that these drops can be explained by how the potentials behave during the switching. This can be seen clearly in Figure 53 and Figure 54, showing how the voltage and current deviates some seconds before converging towards the wanted value. The deviation is a jump taking both voltage and current outside of the desired range for testing, for instance when the voltage is changed from -1.05 to -1.75V, values of -3.2V are registered during the switch.

When comparing the regions of anodic and cathodic potential in the plastic region of the stress-strain curves, there looks to be more instability during the cathodic regions. This could arguably be said for all the stress-strain figures, but is most easily seen in Figure 47, Figure 49 and Figure 57. Common for these curves are that these are the pillars which were compressed early (compression performed for 1400M\_Ti were started with P21 and ascending, and for 1400M P23 and descending). The testing is done in around 4 hours for 13 pillars, and the later compressions might be influenced of all the switching between potentials. This could be a reason for what appears to be more drifting and instabilities in the later curves, such as Figure 52 (and others which can be seen in the Appendix).

Comparing the sample containing titanium to the titanium free one, there are few obvious differences. The jumps already discussed, supposedly due to the immediate effect of the switching, are more present and clear for the sample with titanium. This is however less relevant, as it appears unlikely this is an effect of hydrogen. Both samples do however display an effect of hydrogen, in the way that the regions of cathodic potential are more filled with instabilities than the ones of anodic potential. No clear reduction of this is found in the titanium-sample when compared against the titanium-free one

## 7.5 Further work

---

Upon reviewing the tests performed in this thesis an experimental method for milling good pillars have been found, as well as good indentation parameters. However, there is always room for improvement and the scatter obtained for some of the pillars are larger than optimal. The new method using extremely slow strain-rate compression is being developed, allowing us to switch between hydrogen and hydrogen-free conditions for one single pillar, thus avoiding the scatter related to different pillars. The first rounds of results are very promising, but there are some factors which need improvement. One of these is achieving better control of the electrochemical switching, avoiding the jumps discussed in the previous section. Another interesting test would be to investigate the effect of this switching on the samples. Achieving better cleaning of the samples after these tests is also needed in order to get better post-compression images of the pillars.

The fact that the experimental method for both milling pillars and in situ switching charging is in place is a good help for the EU-project MultiHy, which will continue. Logical next steps are using the same setup for the newly-arrived niobium-carbide containing samples and investigate whether these carbides have a better effect than the titanium ones in hindering hydrogen embrittlement.

## 8 Conclusions

---

This thesis has investigated the effect of titanium carbides on the nanomechanical behavior of high-strength steel under hydrogen charged conditions. The carbides resulted in the largest difference for the testing of the martensitic samples, where hydrogen damage was seen, and reduced for the sample containing the carbides. This showed the expected effect: adding titanium carbides decreases the hydrogen effect.

On the other hand, the same compression tests were performed on pillars on the ferritic samples without any apparent hydrogen damage to the yield strength. The sample containing titanium carbides proved to have a higher hardness, but did not show any improved property regarding hydrogen as there was no real reduction in the yield strength for the tests performed under hydrogen charging.

For both tests the titanium carbides appeared to have an effect of the strain hardening when comparing compression in air and under hydrogen charging. The addition of carbides seemed to counter the hydrogen effect, as the sample without titanium displayed a decrease in strain hardening when switching to hydrogen. This effect is reversed for the titanium-containing sample which demonstrated an increase in strain hardening when switching to hydrogen.

Finally an experimental method compressing single pillars under varying potentials was developed and tested. Both samples showed an effect of hydrogen, but no clear difference was found between the effects on the sample with titanium compared to the one without. An effect of the switching between potentials was observed, causing a drop in the stress-strain curves when going to cathodic potential.

## 9 Bibliography

---

1. **Kuipers, J.** Project work: Effect of hydrogen on nano-sized specimens of steel. *Internal NTNU*. Trondheim : NTNU, 2012.
2. MultiHy. *About MultiHy*. [Online] 2011. [Cited: October 1, 2012.] <http://www.multihy.eu/about-multihy>.
3. **Cwiek, J.** Prevention methods against hydrogen degradation of steel. *Journal of Achievements in Materials and Manufacturing Engineering*. 2010, Vol. 43, 1.
4. **Beachem, C. D.** A new model for hydrogen-assisted cracking (hydrogen "embrittlement"). *Metallurgical Transactions*. 2. s.l. : Springer-Verlag, 1972, Vol. 3, pp. 441-455.
5. **Birnbaum, H.K.** *Mechanisms of hydrogen related fracture of metals*. Urbana : University of Illinois Materials Research Laboratory, 1989.
6. **Morlet, J., Johnson, H., Troiano, A.** A new concept of hydrogen embrittlement in steel. *Journal of the Iron and Steel Institute*. 1958, Vol. 189.
7. **Wriedt, H.A. and Oriani, R.A.** Effect of tensile and compressive elastic stress on equilibrium hydrogen solubility in a solid. *Acta Metall.* 18, 1970.
8. **Sun, S., Shiozawa, K., Gu, J., Chen, N.** Investigation of deformation field and hydrogen partition around crack tip in fcc single crysta. *Metallurgical and Materials Transactions A*. 1995, Vol. 26, 3.
9. **Gao, H., Cao, W., Fang, C., Rios, E.R. de los.** Analysis of crack tip hydrogen distribution under I/II mixed mode loads. *Fatigue & fracture of engineering materials & structures*. 1994, Vol. 17, 10.
10. **Robertson, I.M. and Birnbaum, H.K.** An HVEM study of hydrogen effects on the deformation and fracture of nickel. *Acta Metallurgica, Volume 34, Issue 3, pp 353-366*. s.l. : Elsevier, 1986.
11. **Chan, K.S.** A fracture model for hydride-induced embrittlement. *Acta Metallurgica et Materialia*. 12th. Texas : Elsevier, 1995, Vol. 43, pp. 4325-4335.
12. **Gangloff, R.P.** Hydrogen Assisted Cracking of High Strength Alloys. *Comprehensive Structural Integrity*. 2003, Vol. 6.
13. *Progress Towards Understanding Mechanisms Of Hydrogen Embrittlement And Stress Corrosion Cracking*. **Lynch, S.P.** Nashville, Tennessee : NACE International, 2007.
14. **Turnbull, A., Carrol, M. and Ferriss, D.H.** Analysis of hydrogen diffusion and trapping in a 13% chromium martensitic stainless steel. *Acta Metallurgica*. 37, 1989, 7.
15. **Pressouyre, G.M. and Bernstein, M.** A quantitative analysis of hydrogen trapping. *Metallurgical Transactions A*. 1978, Vol. 9, 11.
16. **Pressouyre, G.M.** Trap theory of Hydrogen embrittlement. *Acta Metallurgica*. 1980, Vol. 28, 7.
17. **Brass, A.M. and Chene, J.** Influence of deformation on the hydrogen behavior in iron and nickel base alloys: a review of experimental data. *Materials Science and Engineering: A*. 1998, Vol. 242, 1-2.
18. **Takahashi, J., Kawakami, K., Kobayashi, Y., Tarui, T.** The first direct observation of hydrogen trapping sites in TiC. *Scripta Materialia*. 2010, Vol. 63, 3.
19. **Dake, J.** Effects of cathodic hydrogen on the deformation behaviour of micropillars during compression testing. 2008.
20. ASTM (American Society for Testing and Materials. [Online] [Cited: October 20, 2012.] <http://www.astm.org/Standard/index.shtml>.

21. **Humphreys, F.J.** Characterisation of fine-scale microstructures by electron. *Scripta Materialia*. 2004, Vol. 51, 8.
22. **Palizdar, Y., Cochrane, R.C., Brydson, R., Leary, R., Scott, A.J.** Accurate analysis of EBSD data for phase identification. *Journal of Physics: Conference series*. 2010, Vol. 241.
23. **Yao, Nan.** *Focused Ion Beam Systems*. Cambridge : Cambridge University Press, 2007.
24. **Ali, M.Y., Hung, W. and Yongqi, F.** A Review of Focused Ion Beam Sputtering. *International journal of precision engineering and manufacturing*. 2010, Vol. 11, 1.
25. **Palacio, M.L.B. and Bhushan, B.** Depth-sensing indentation of nanomaterials. *Materials Characterization*. 1, 2013, 20.
26. **Asgari, M., Barnoush, A., Johnson, R., Hoel, R.** *Nanomechanical evaluation of the protectiveness of nitrated layers against*. Trondheim : Elsevier, 2012.
27. **Barnoush, A. and Vehoff, H.** Electrochemical nanoindentation: A new approach to probe hydrogen/deformation interaction. *Scripta Materialia*. 2006, Vol. 55, 2.
28. **Louthan, M. R., Caskey, G.R., Donovan, J.A., Rawl, D.E.** Hydrogen embrittlement of metals. *Materials Science and Engineering*. 1972, Vol. 10.

# 10 Appendix

The appendix includes all the pictures and plots left out of the main thesis, and will document all of the experiments performed.

## 10.1 Pillar compression on samples 1400M

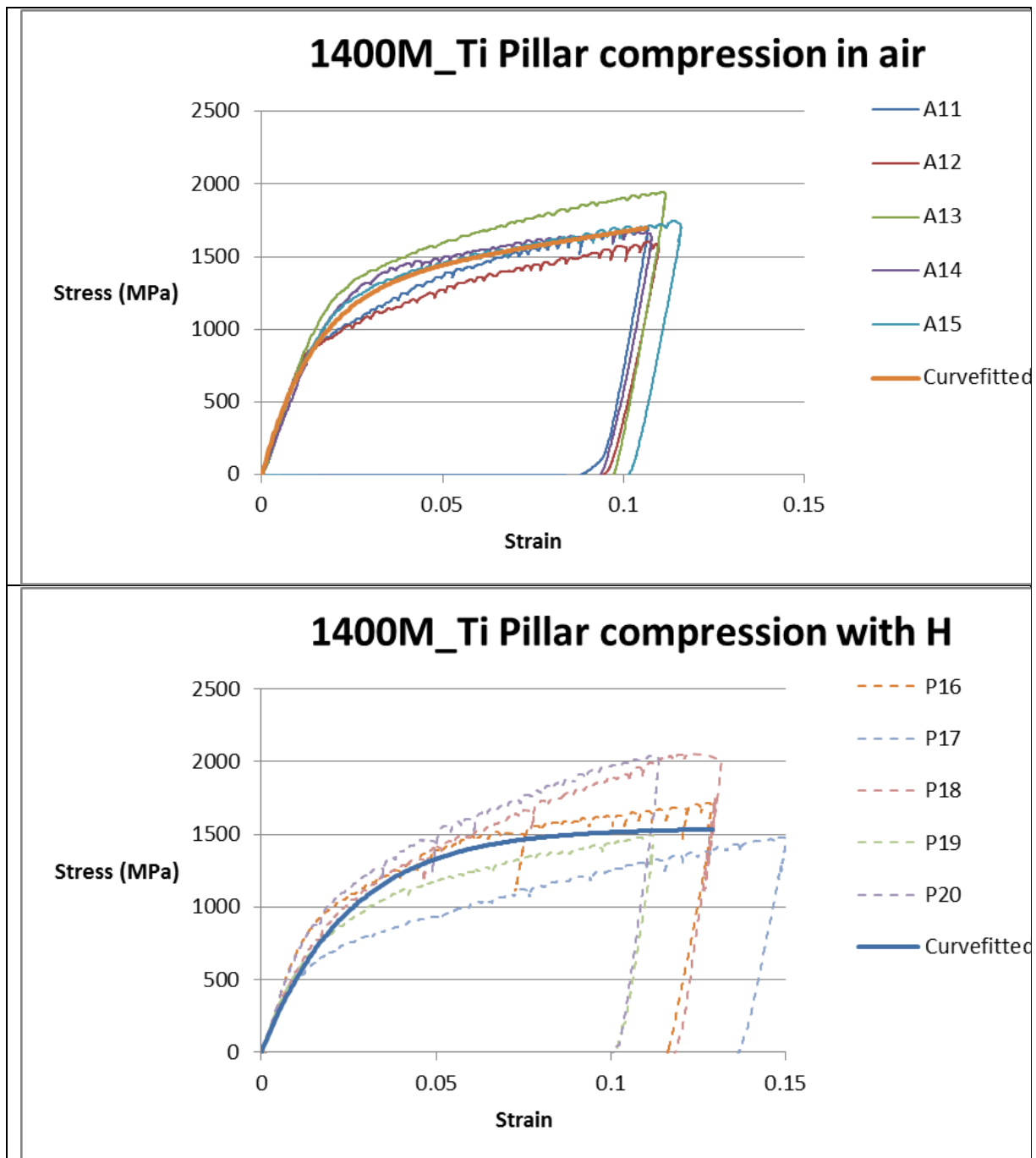
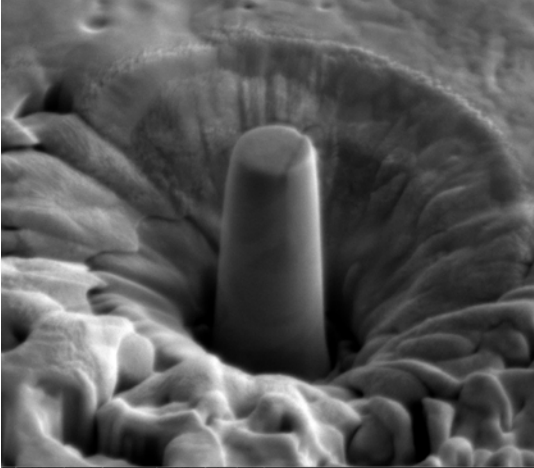
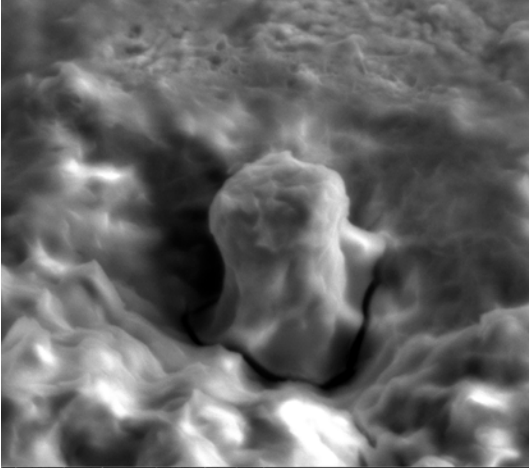
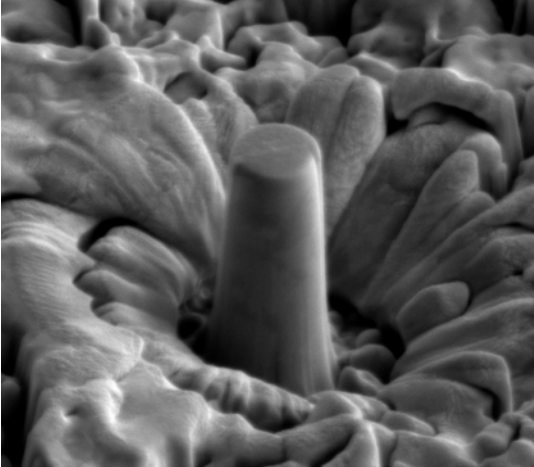
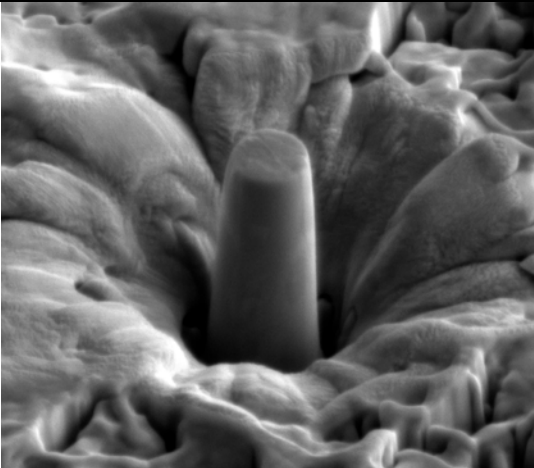
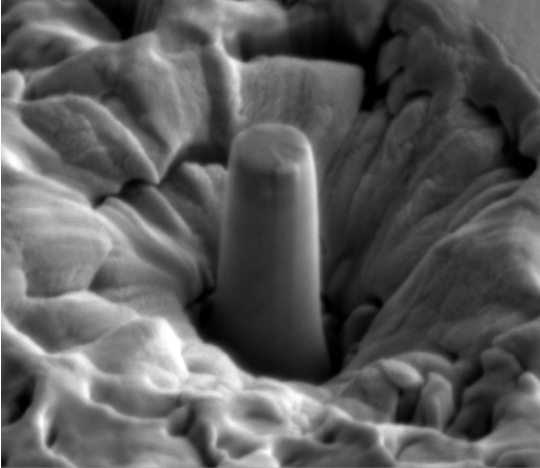
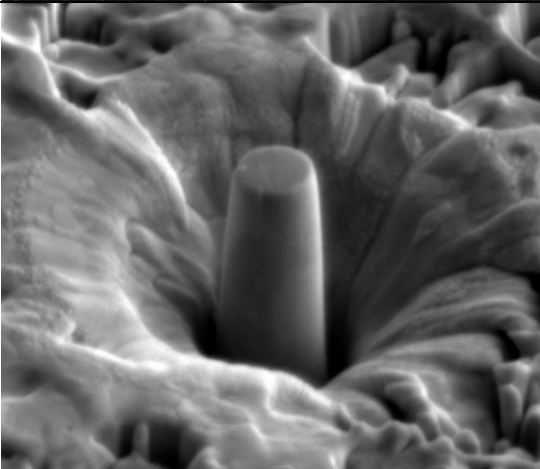
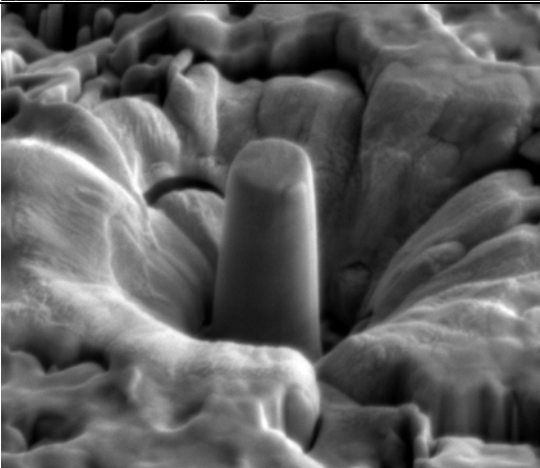


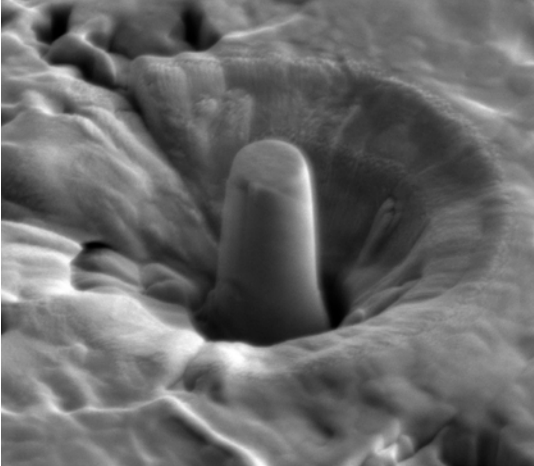
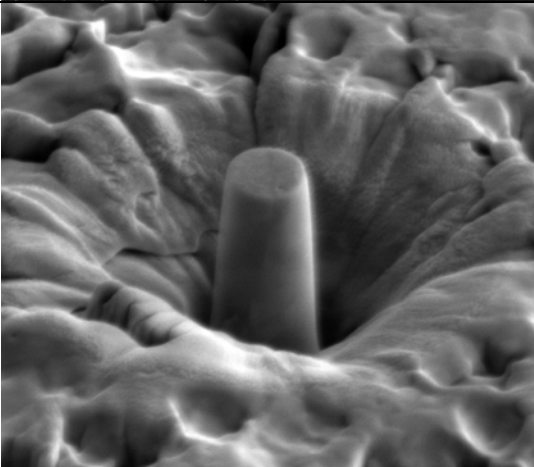
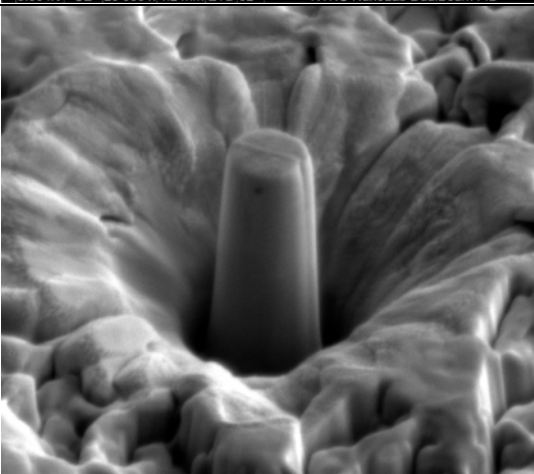
Table 6 - Curve fitted plots from each set of 1400M\_Ti tests

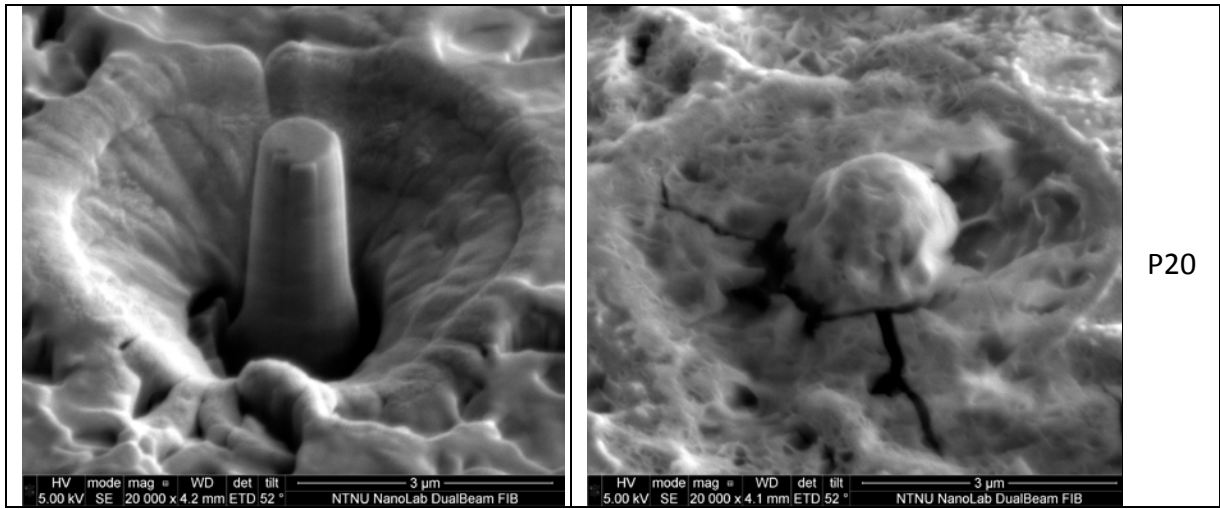
Table 7 shows all pre-compression images of pillars made on sample 1400M\_Ti. Post-images are normally also included, but in the case of this sample the surface was contaminated due to insufficient washing after the sample had been submerged in electrolyte. Examples are included for how the pillars now looked under pillars A11 and P20

 <p>HV mode mag # WD det tilt 3 μm 5.00 kV SE 19 993 x 4.2 mm ETD 52 ° NTNU NanoLab DualBeam FIB</p>	 <p>HV mode mag # WD det tilt 3 μm 5.00 kV SE 20 000 x 4.1 mm ETD 52 ° NTNU NanoLab DualBeam FIB</p>	A11
 <p>HV mode mag # WD det tilt 3 μm 5.00 kV SE 20 002 x 4.2 mm ETD 52 ° NTNU NanoLab DualBeam FIB</p>		A12
 <p>HV mode mag # WD det tilt 3 μm 5.00 kV SE 20 001 x 4.2 mm ETD 52 ° NTNU NanoLab DualBeam FIB</p>		A13



 <p>HV mode mag # WD det tilt 3 μm 5.00 kV SE 19 996 x 4.2 mm ETD 52 ° NTNU NanoLab DualBeam FIB</p>		A14
 <p>HV mode mag # WD det tilt 3 μm 5.00 kV SE 20 000 x 4.2 mm ETD 52 ° NTNU NanoLab DualBeam FIB</p>		A15
 <p>HV mode mag # WD det tilt 3 μm 5.00 kV SE 19 999 x 4.2 mm ETD 52 ° NTNU NanoLab DualBeam FIB</p>		P16

		P17
		P18
		P19



P20

Table 7- 1400M\_Ti pillars pre- and post-compression

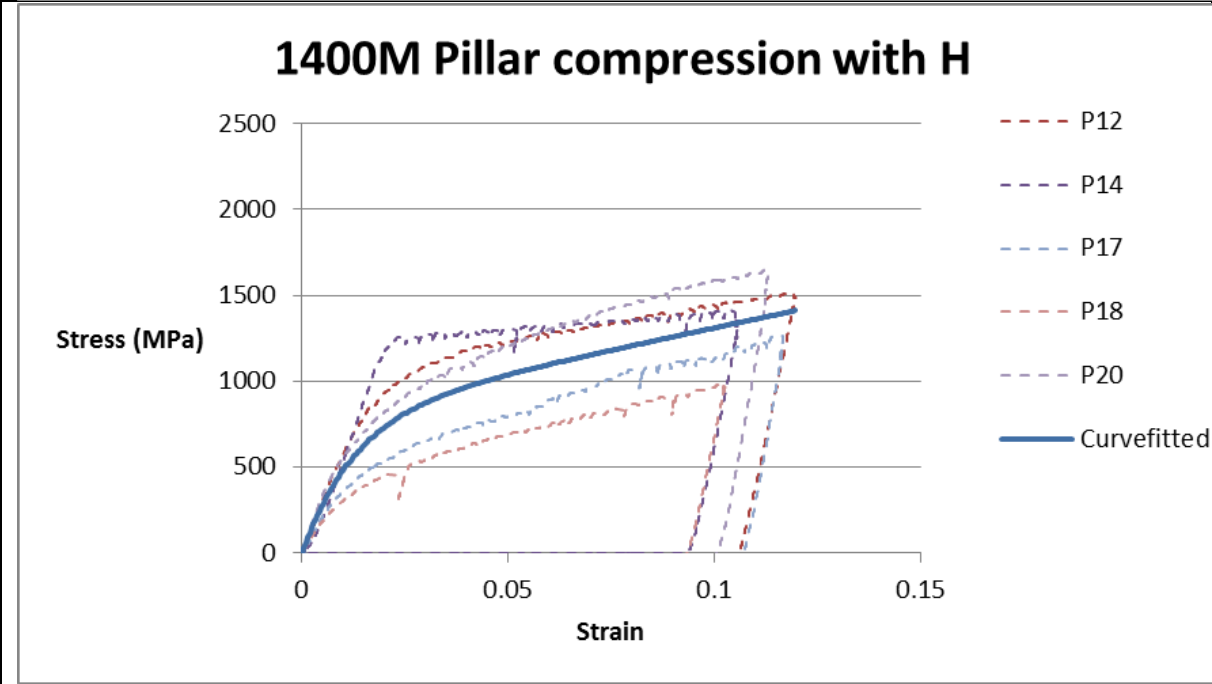
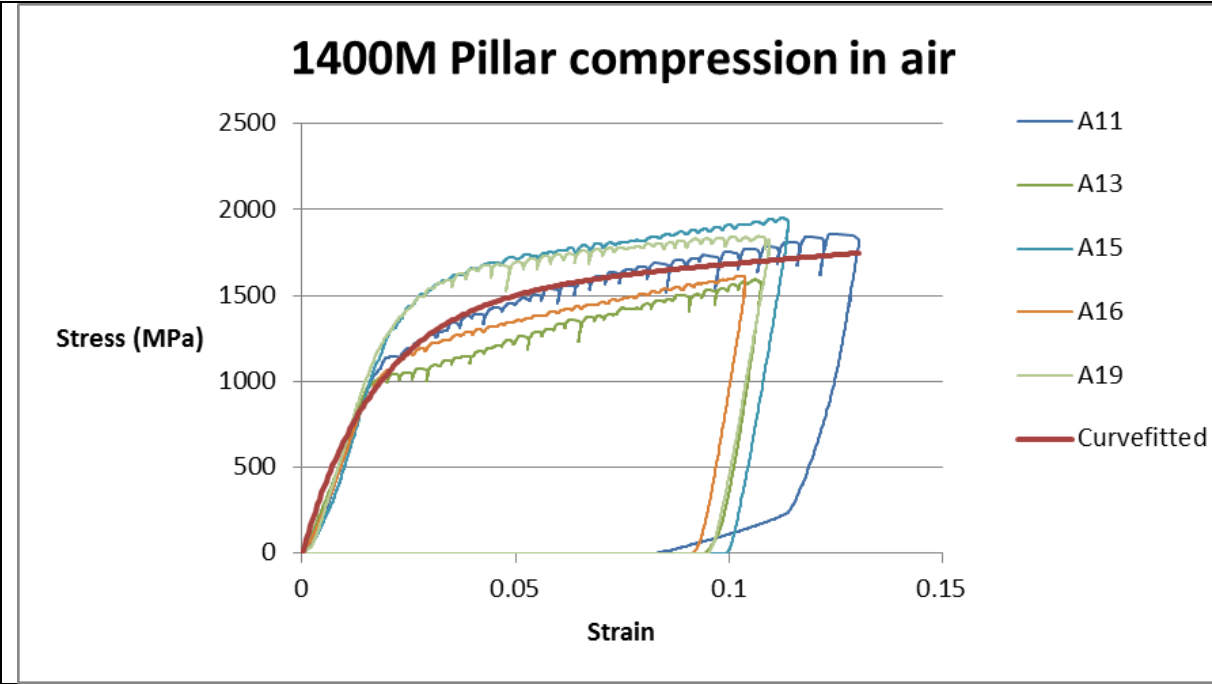
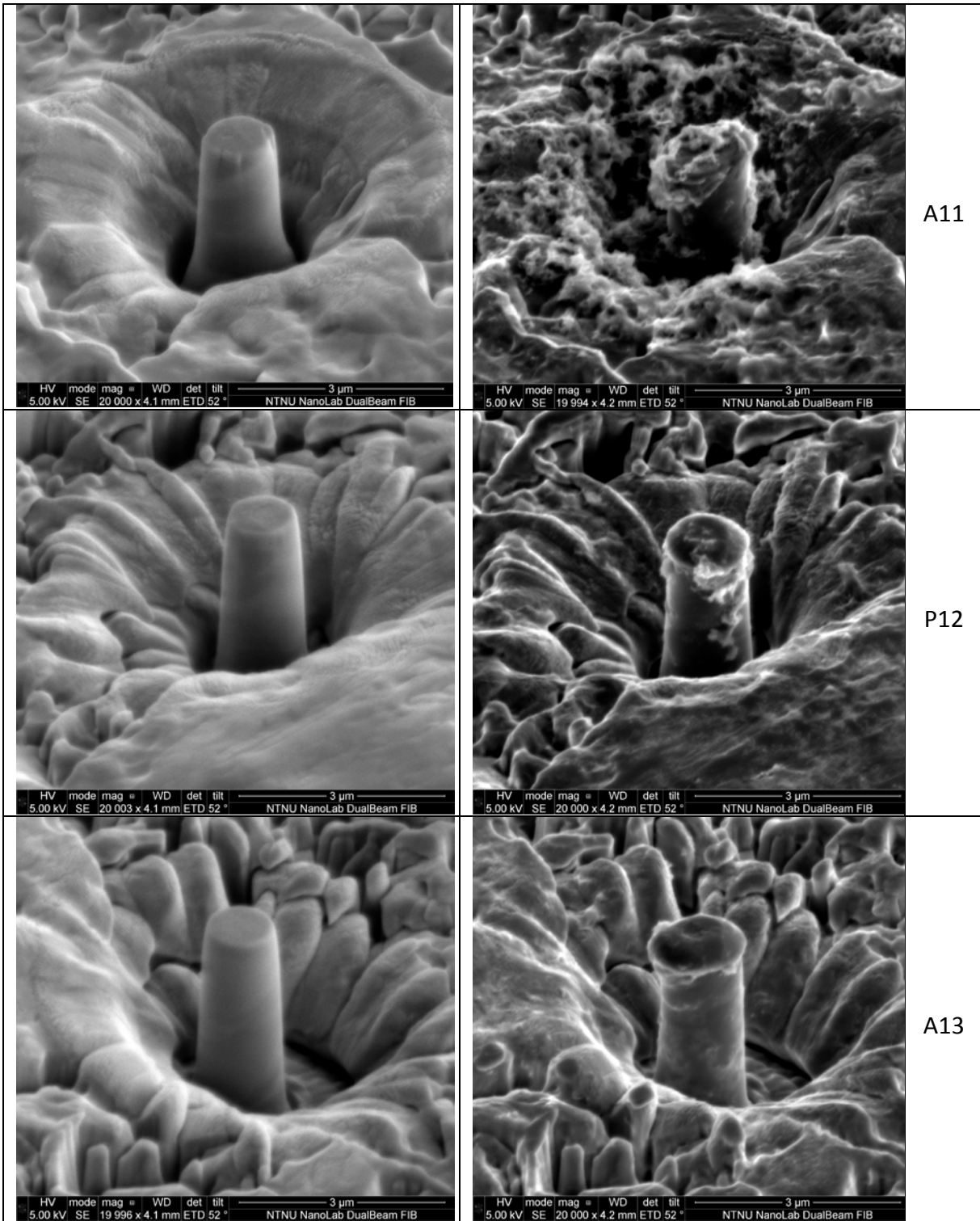
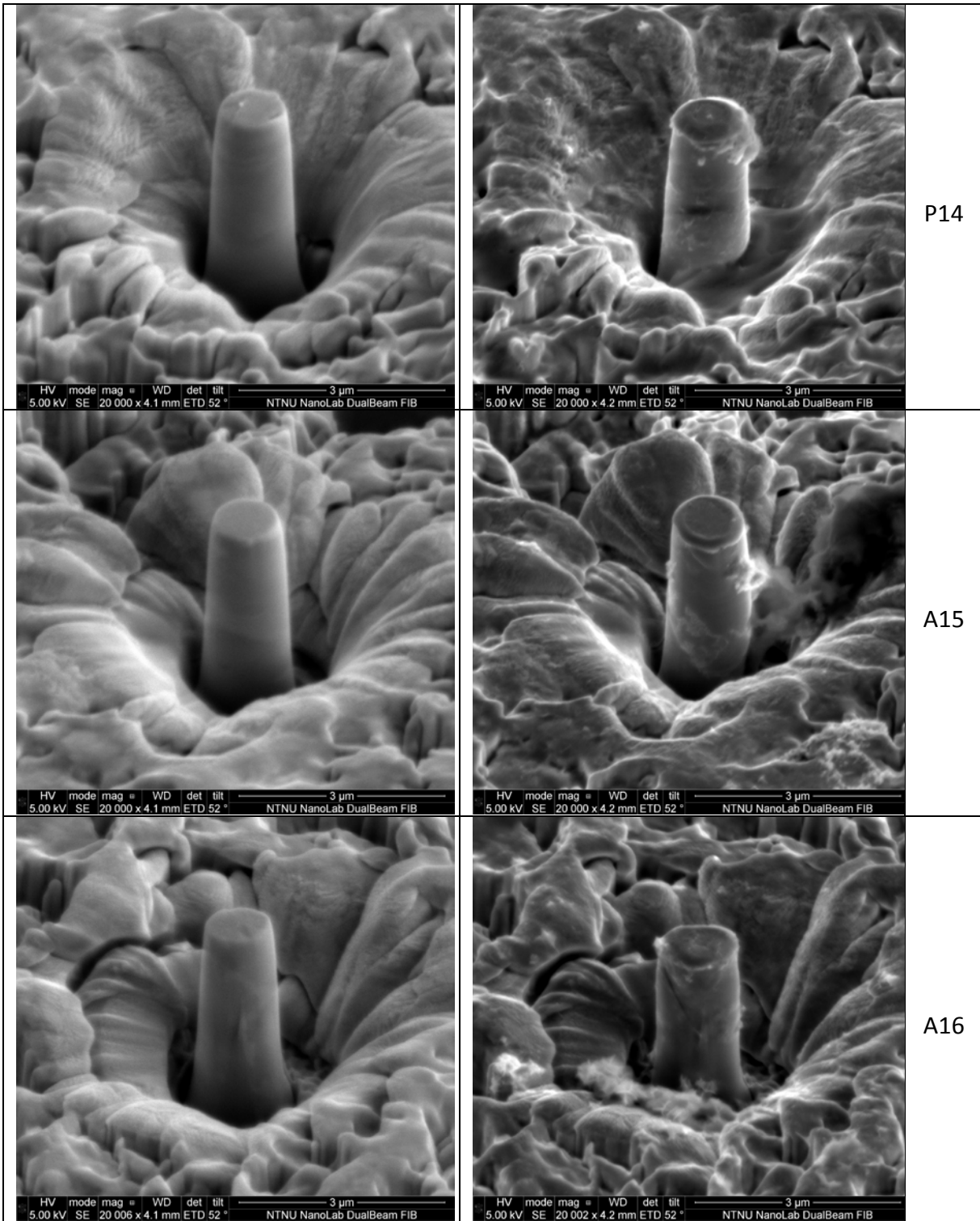
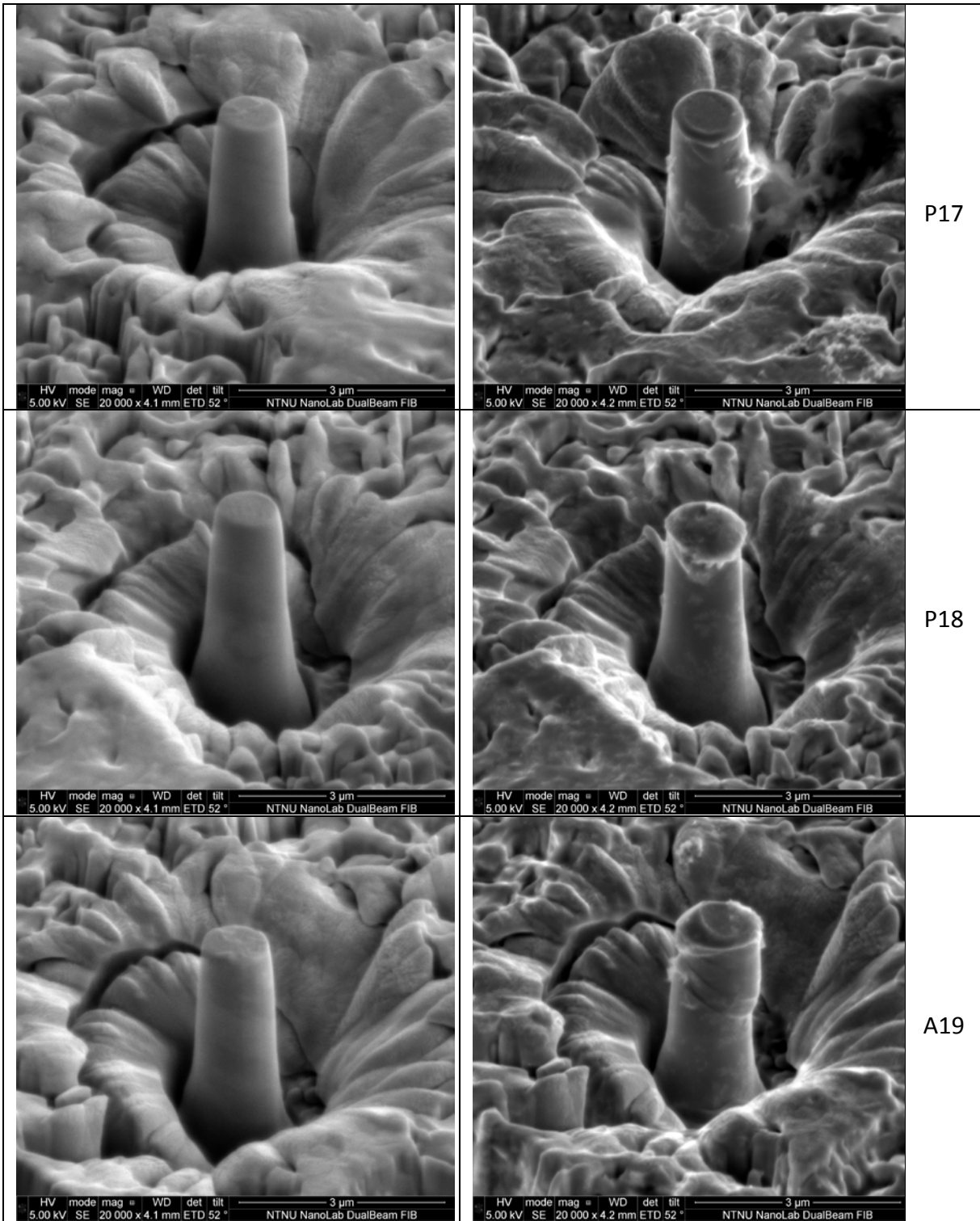


Table 8 - Curve fitted plots from each set of 1400M tests







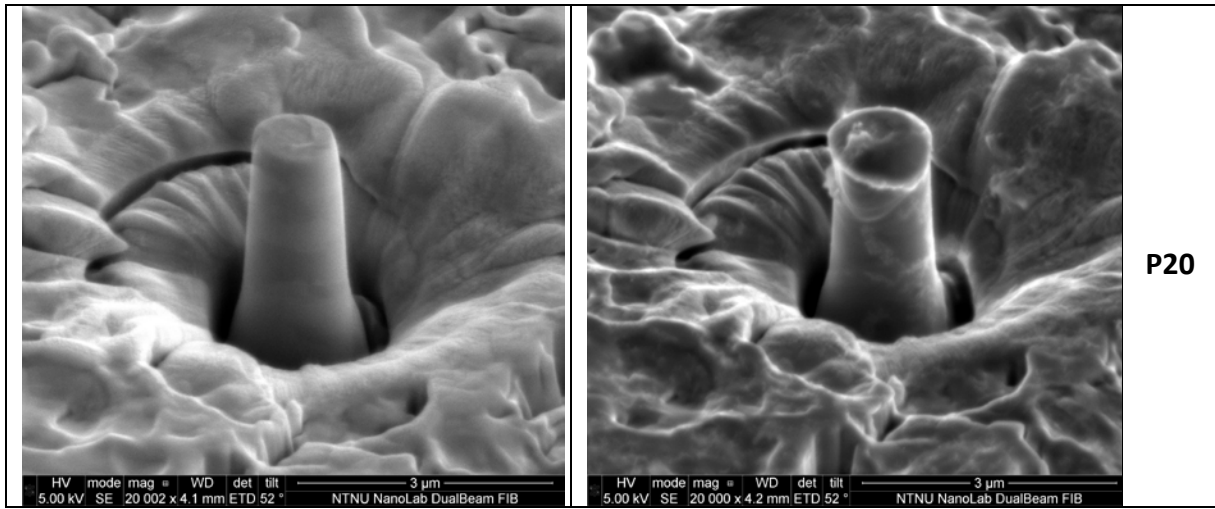


Table 9 - 1400M pillars pre- and post-compression



## 10.2 Pillar compression on samples 1200M

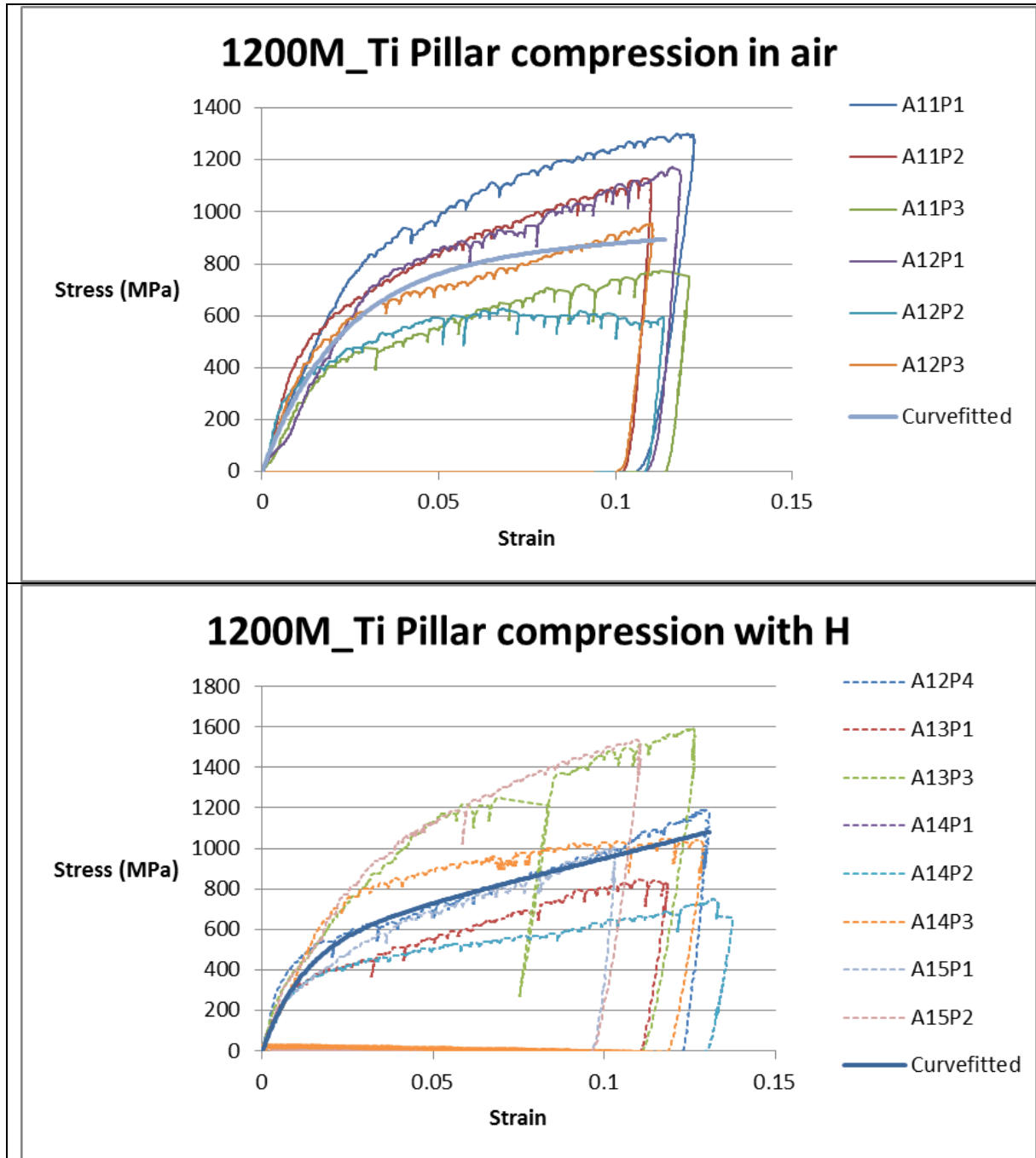
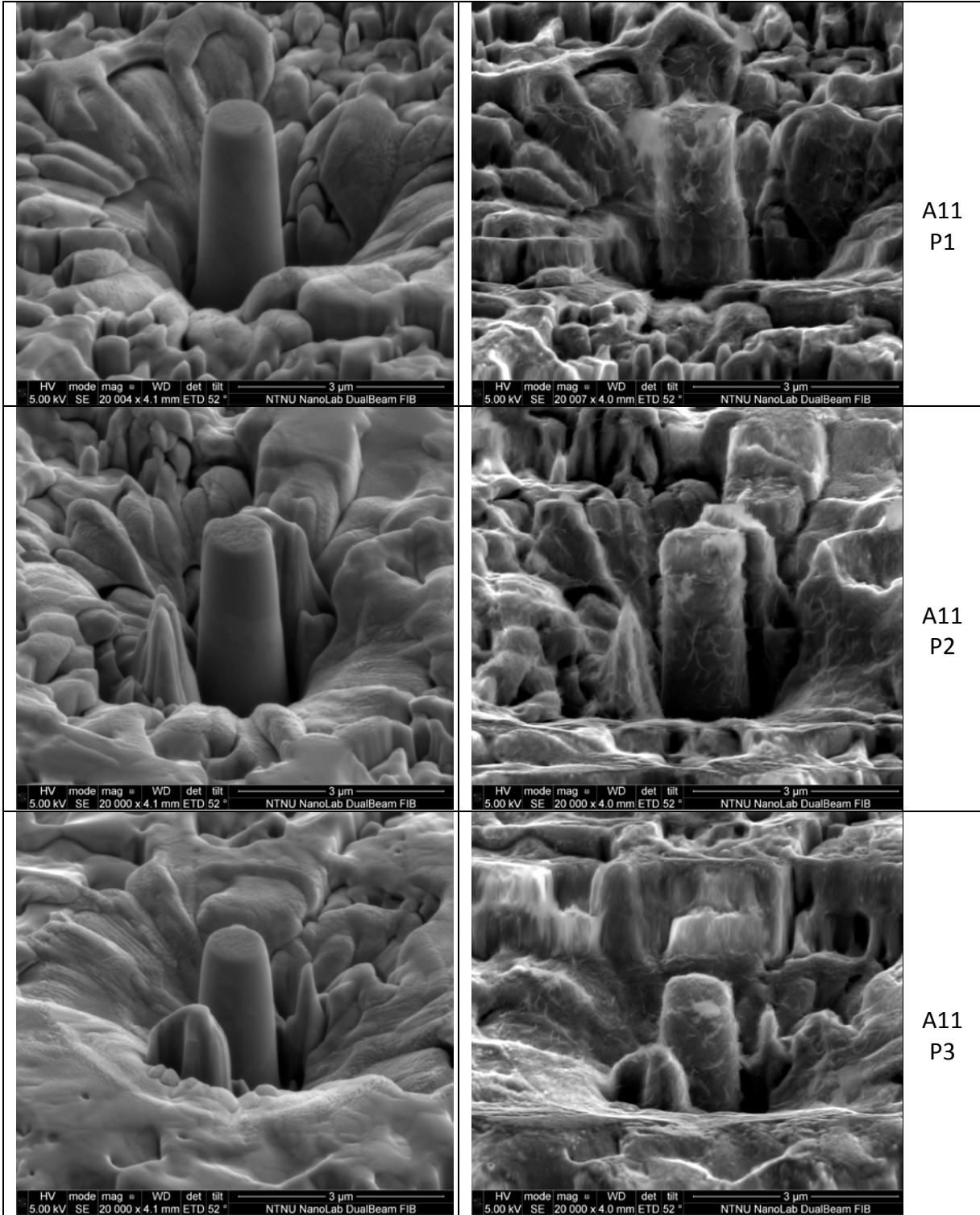
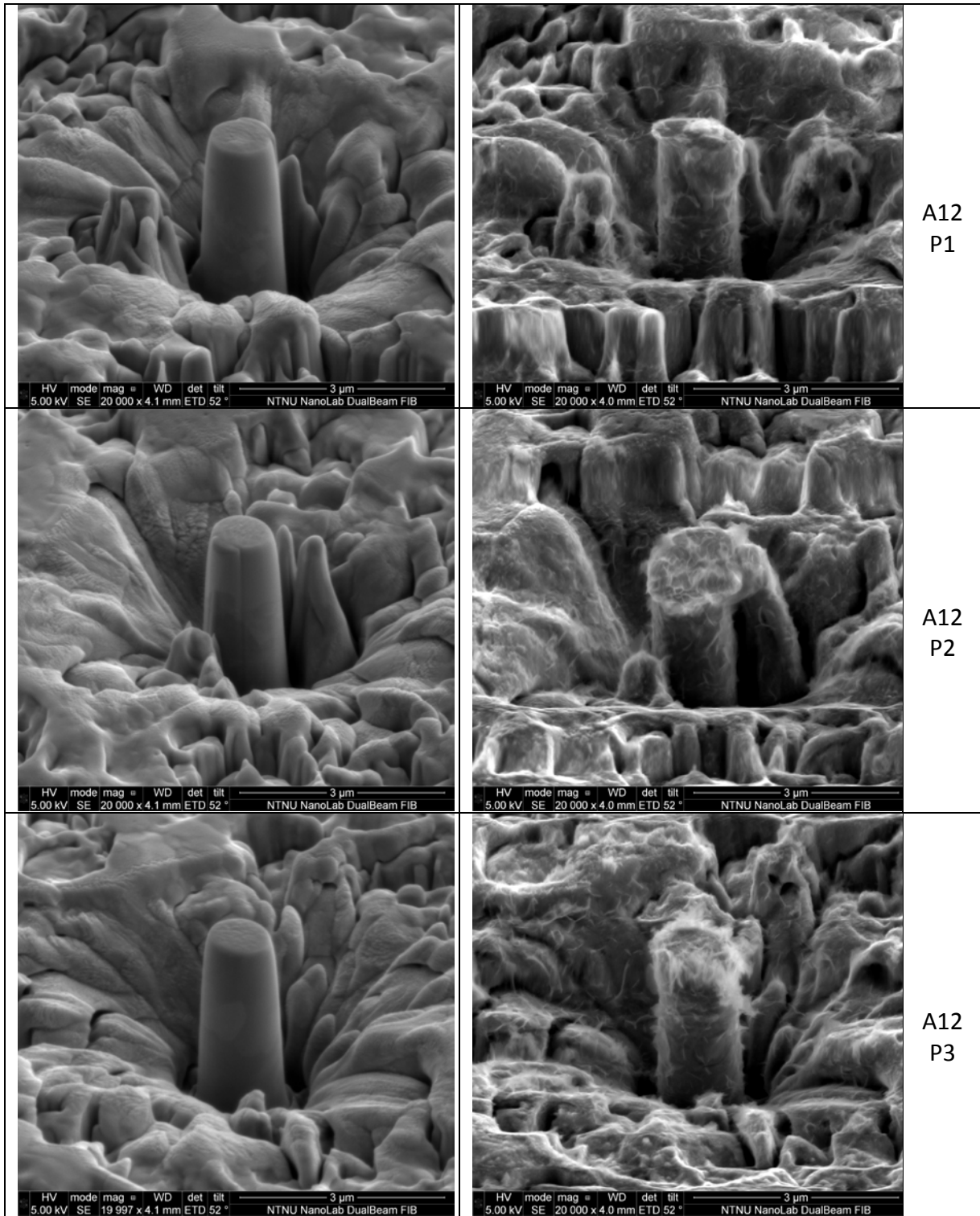
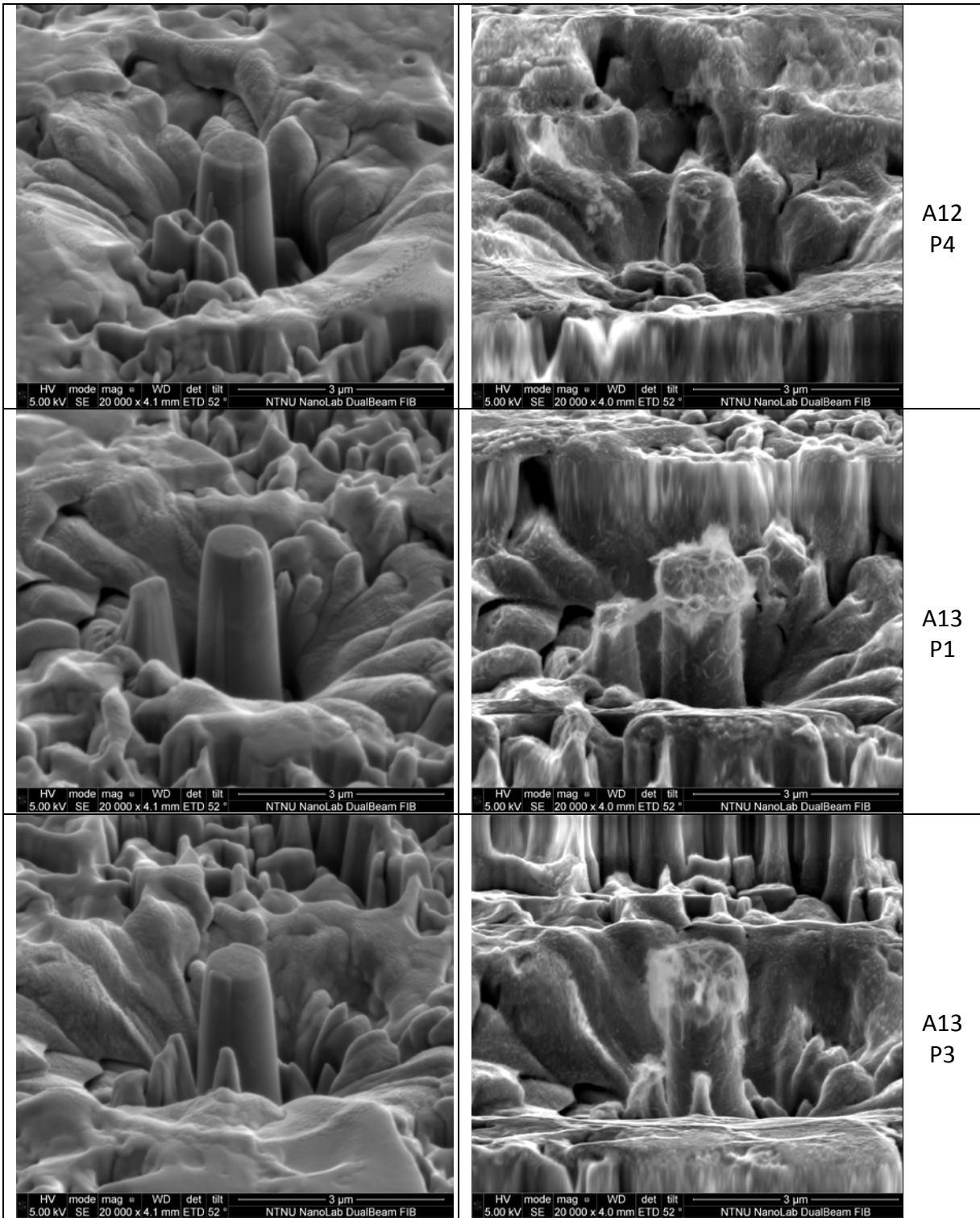
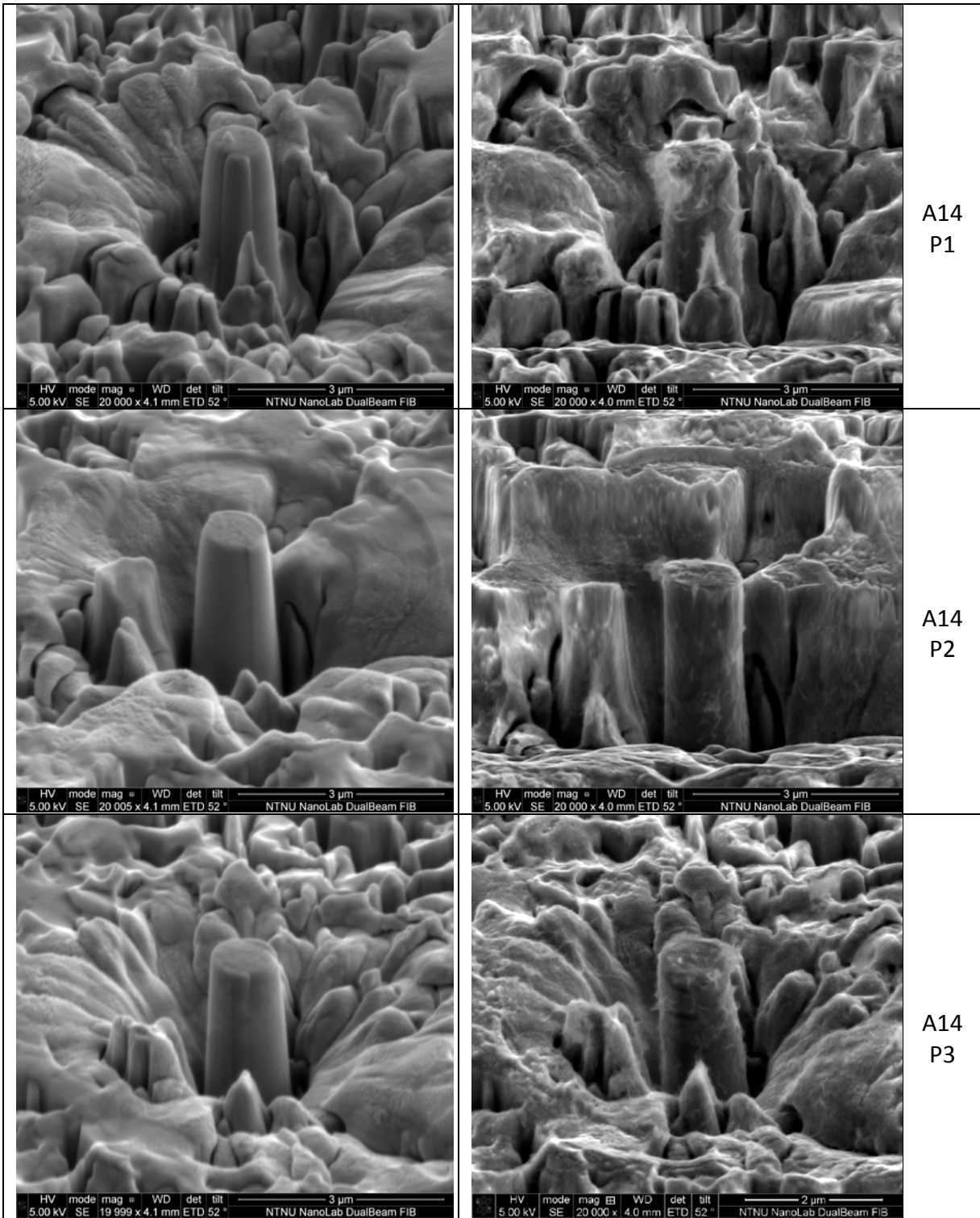


Table 10 - Curve fitted plots from each set of 1200M\_Ti pillars









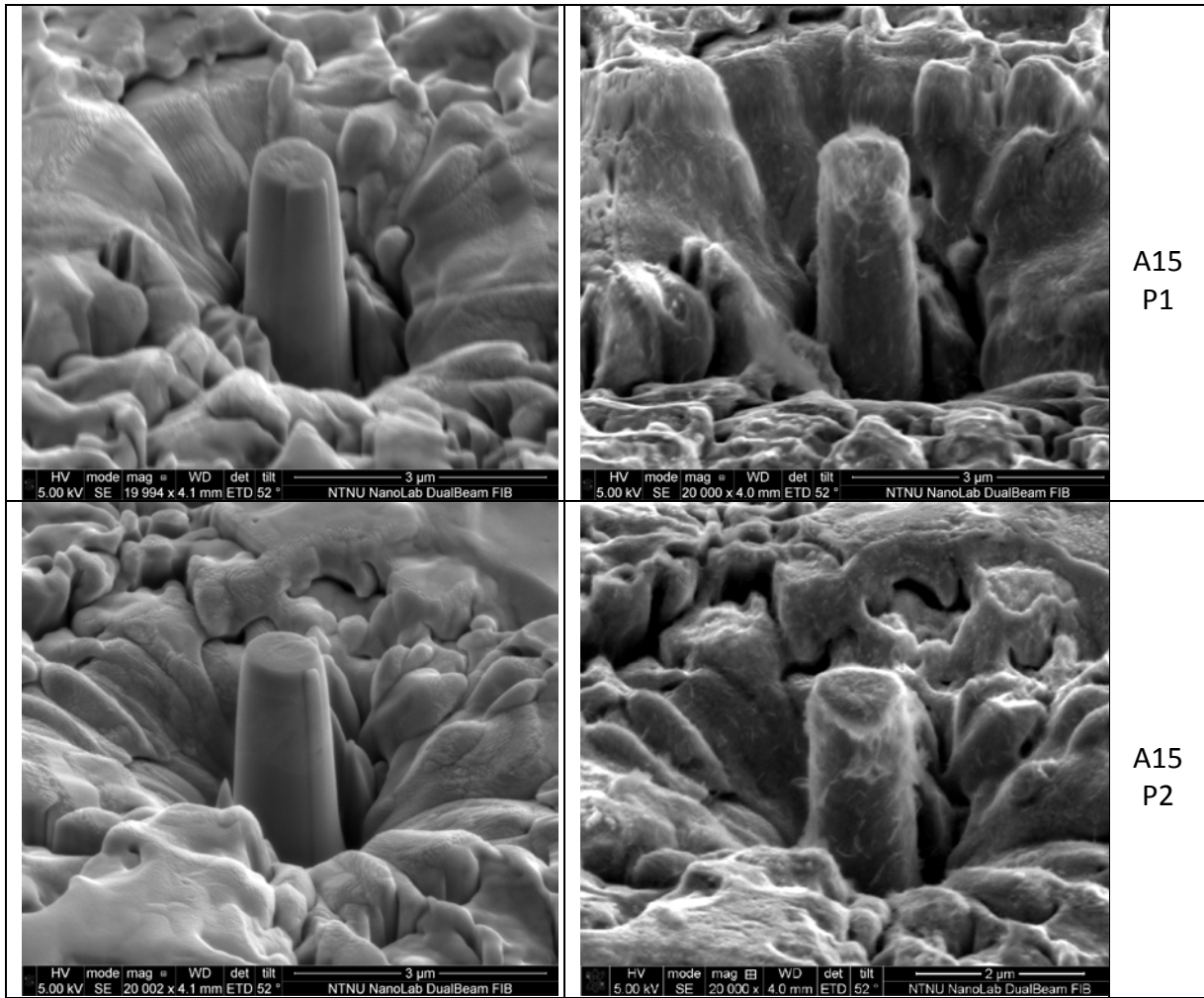


Table 11 – 1200M\_Ti pillars pre- and post-compression

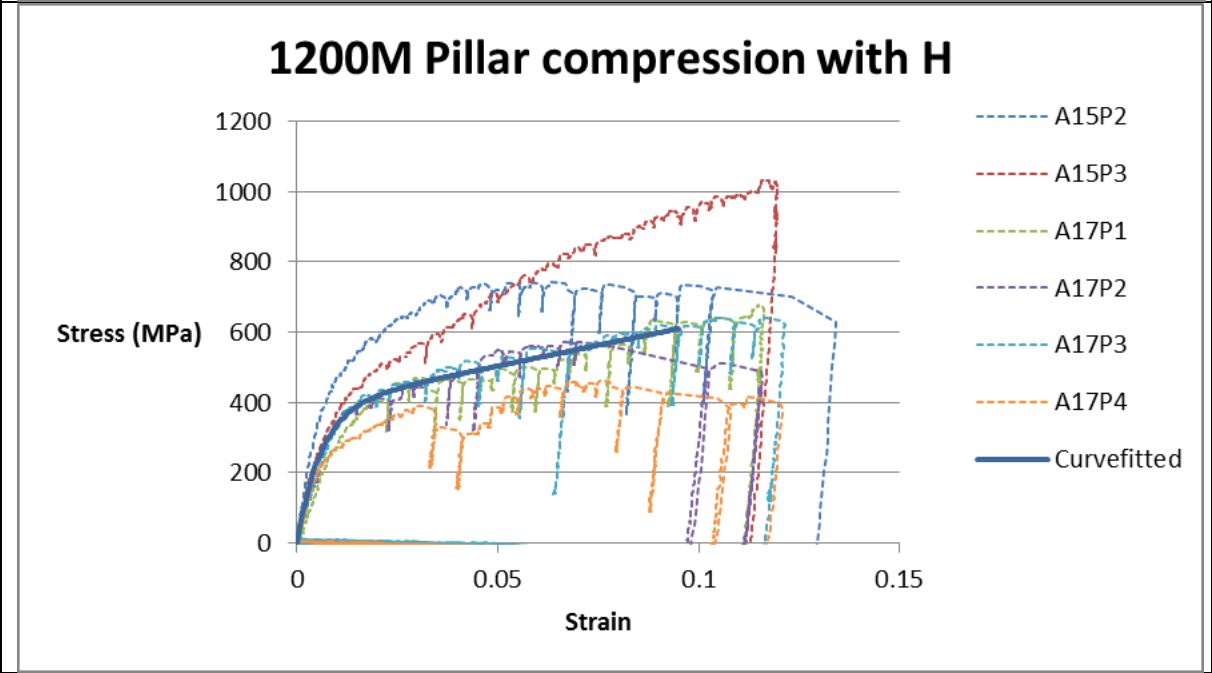
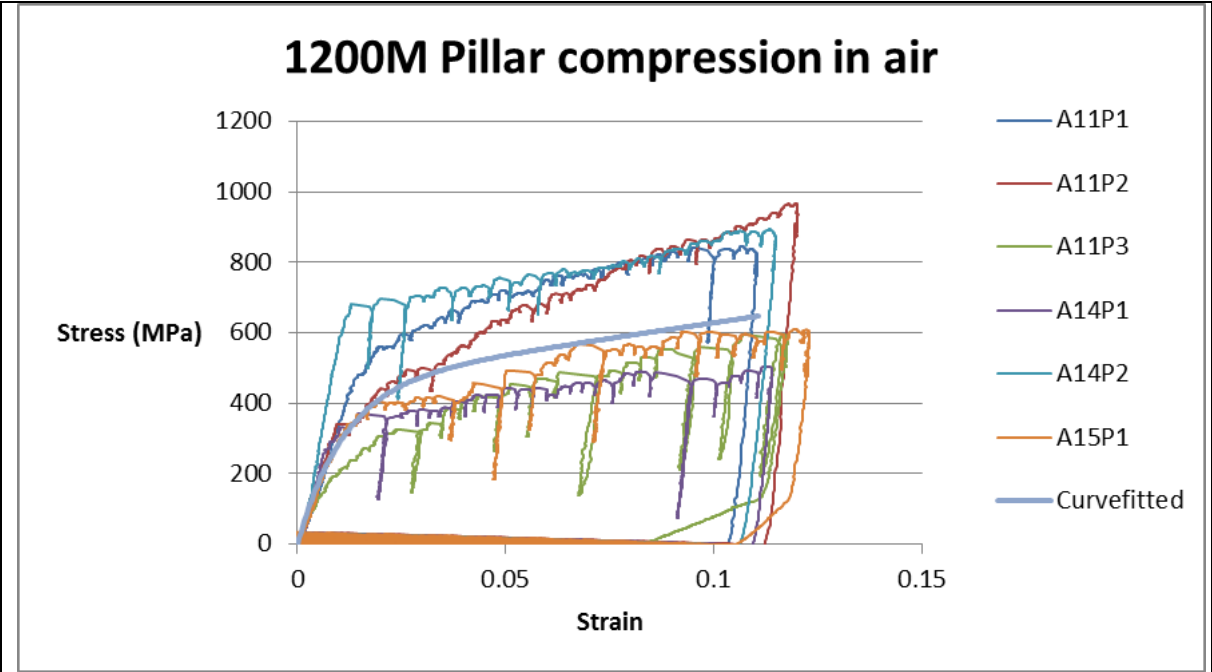
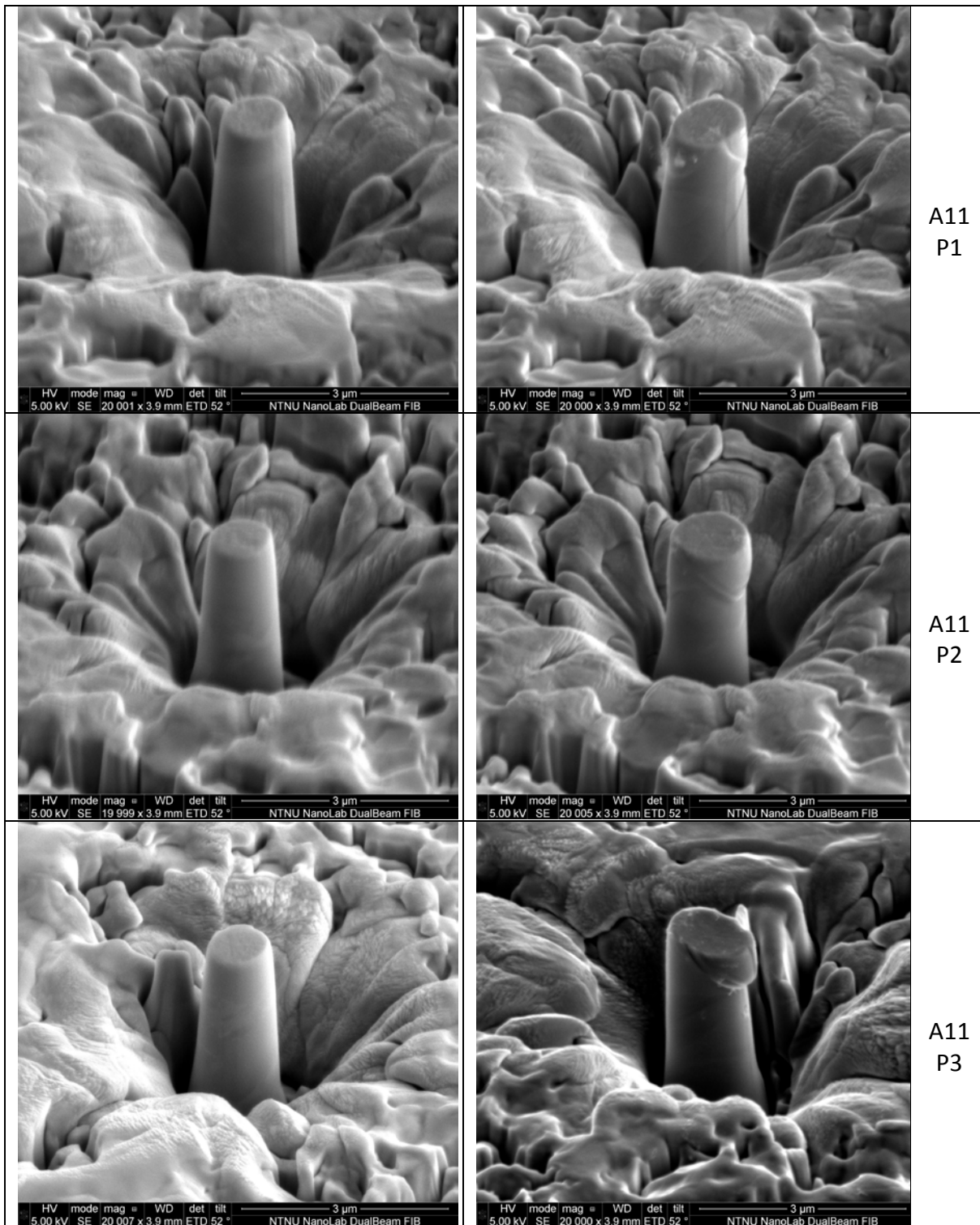
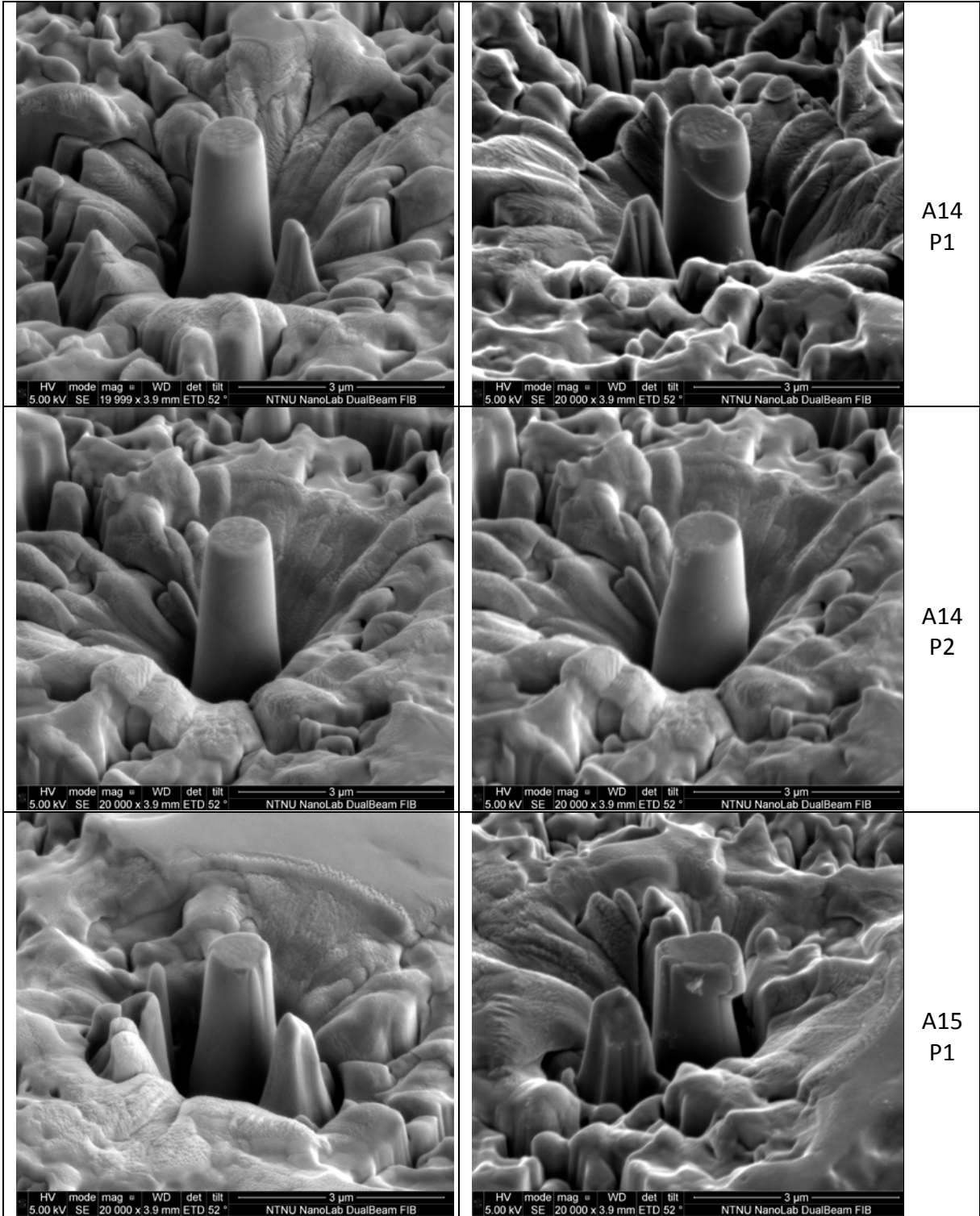
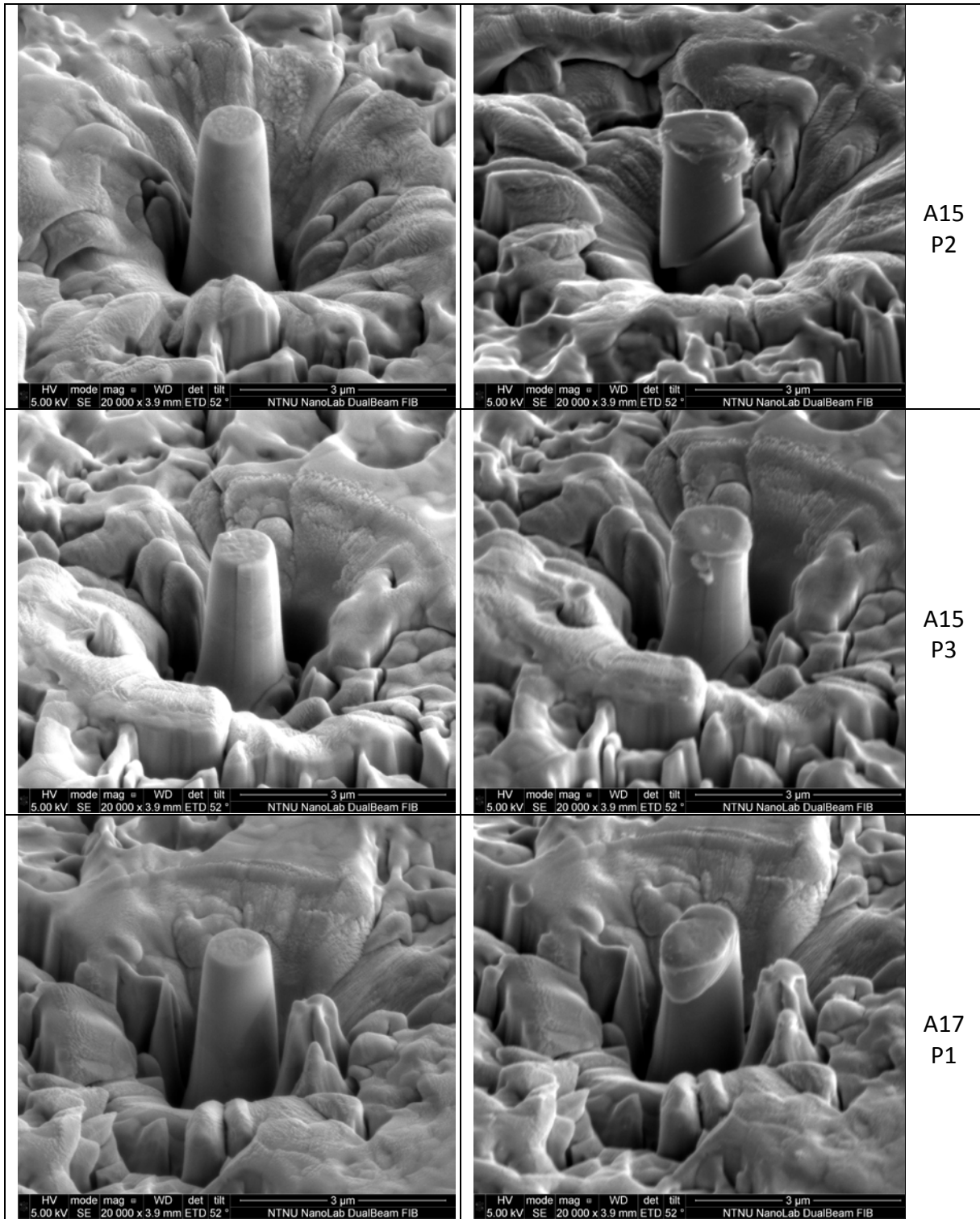


Table 12 - Curve fitted plots from each set of 1200M pillars









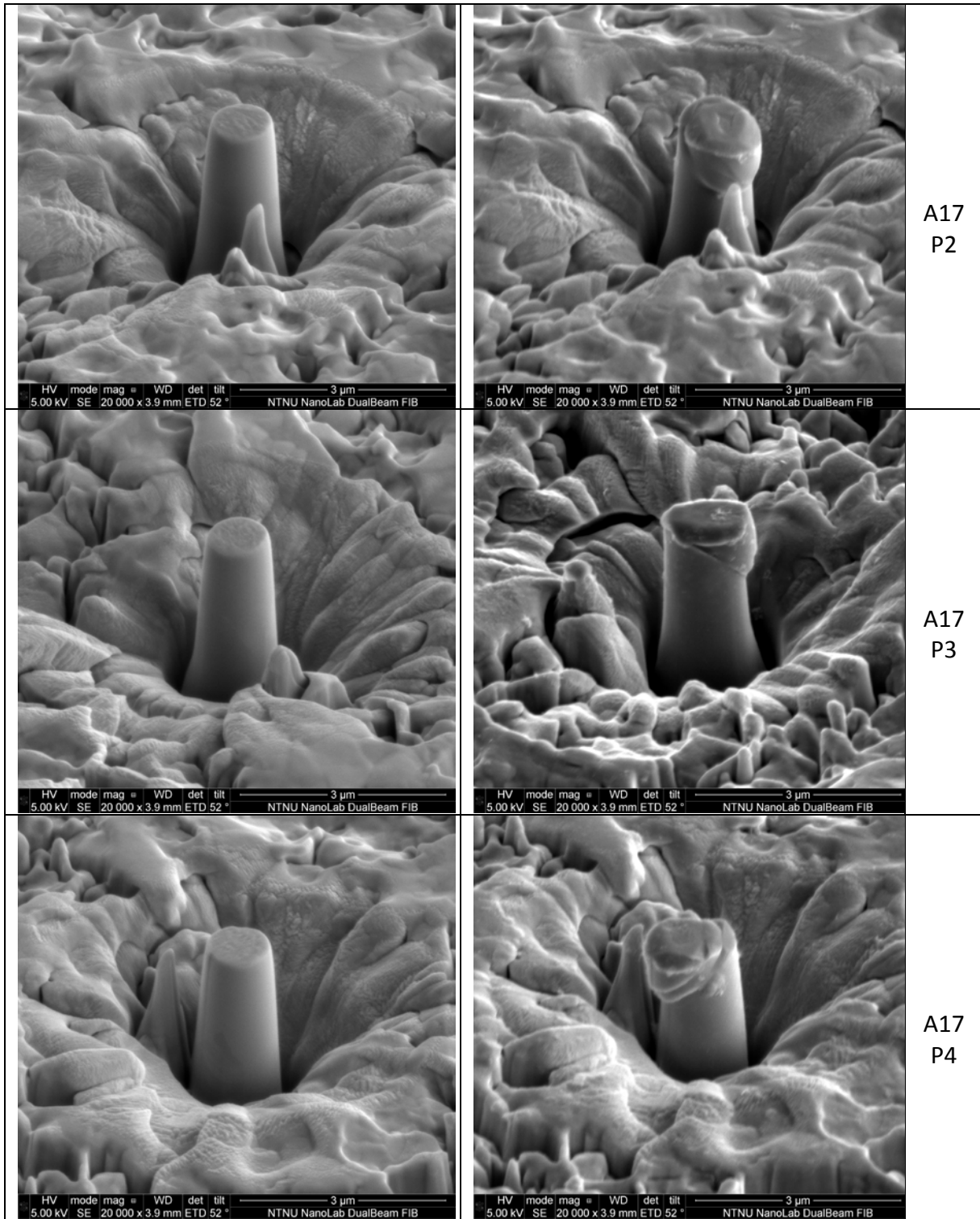
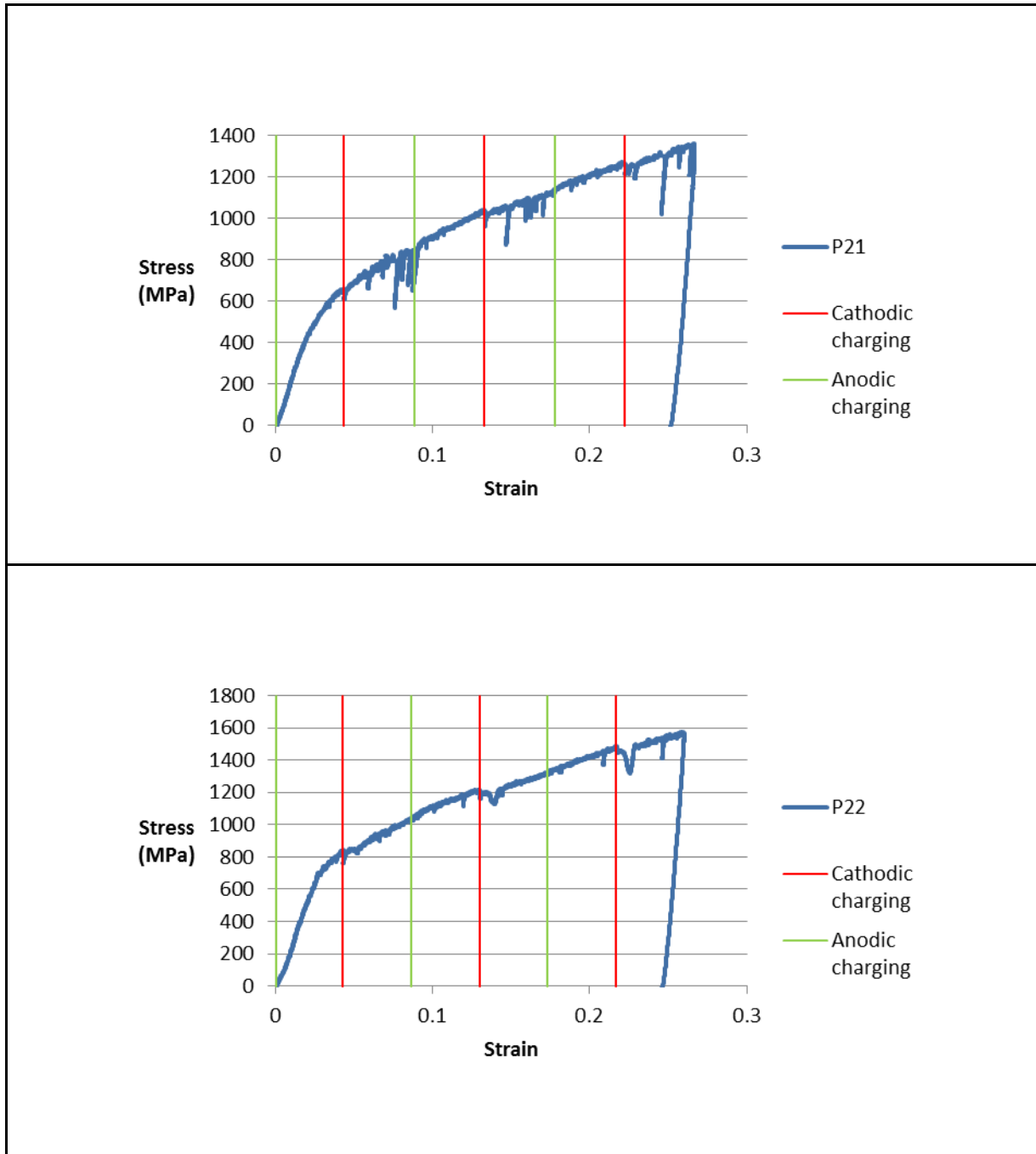
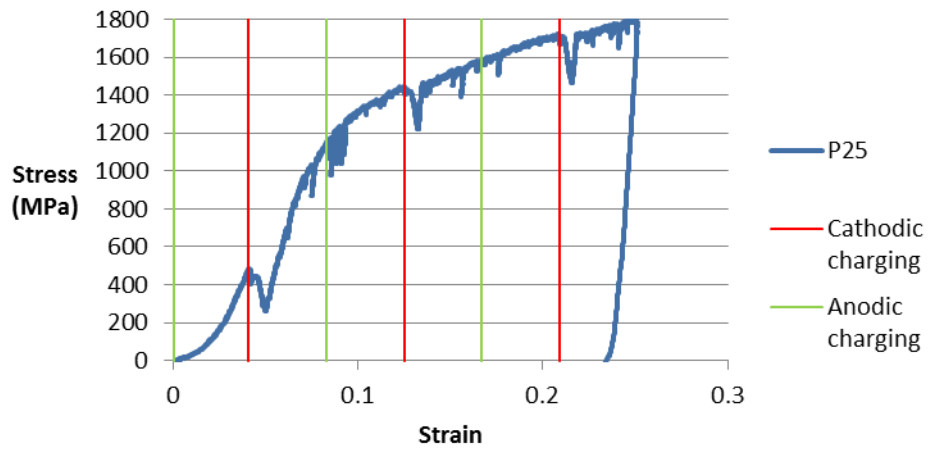
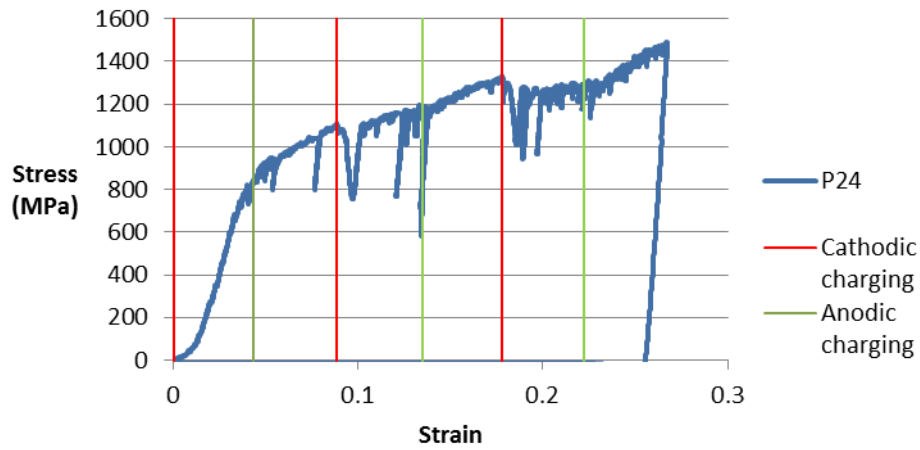
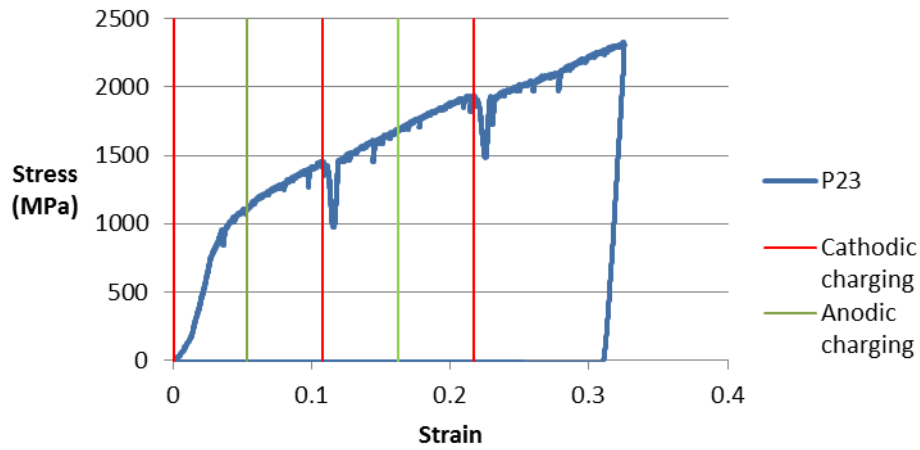


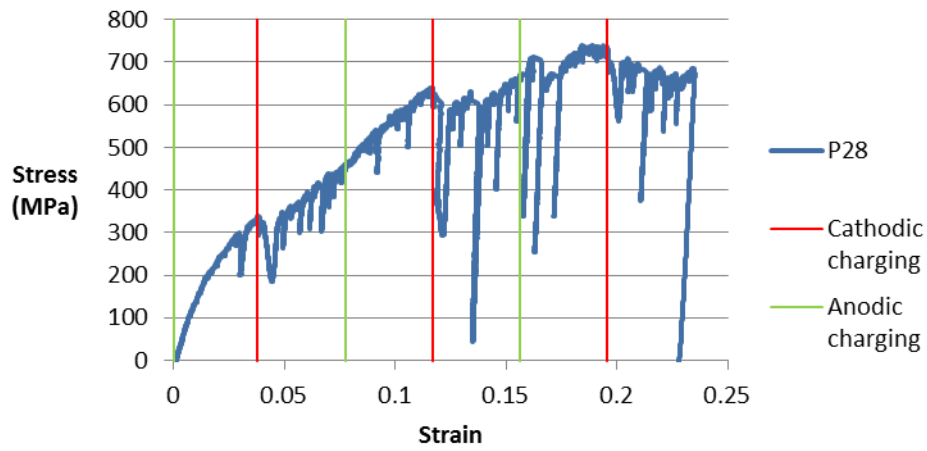
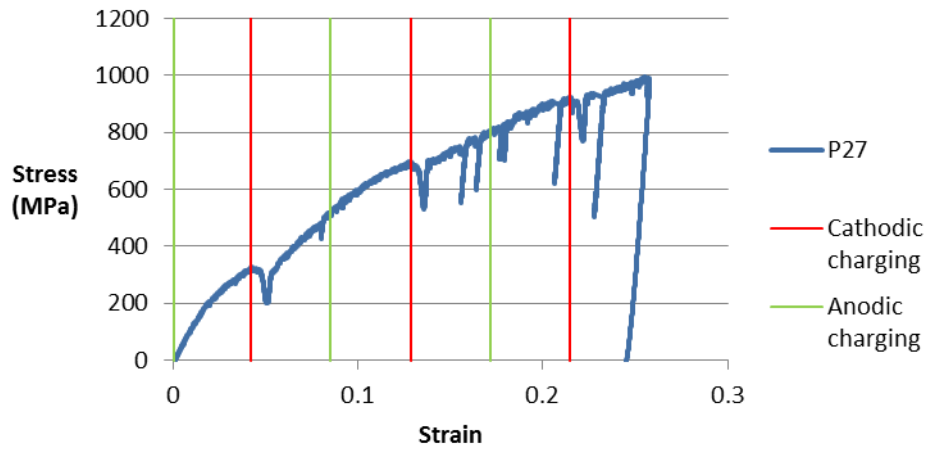
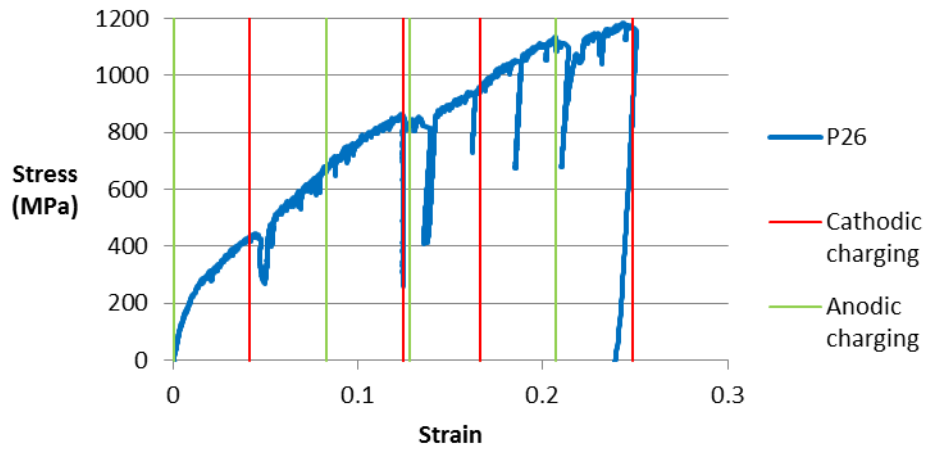
Table 13 - 1200M pillars pre- and post-compression

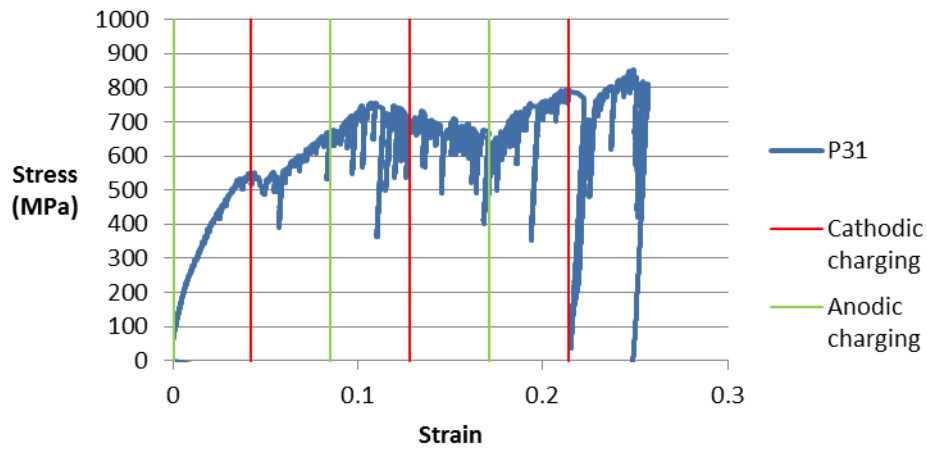
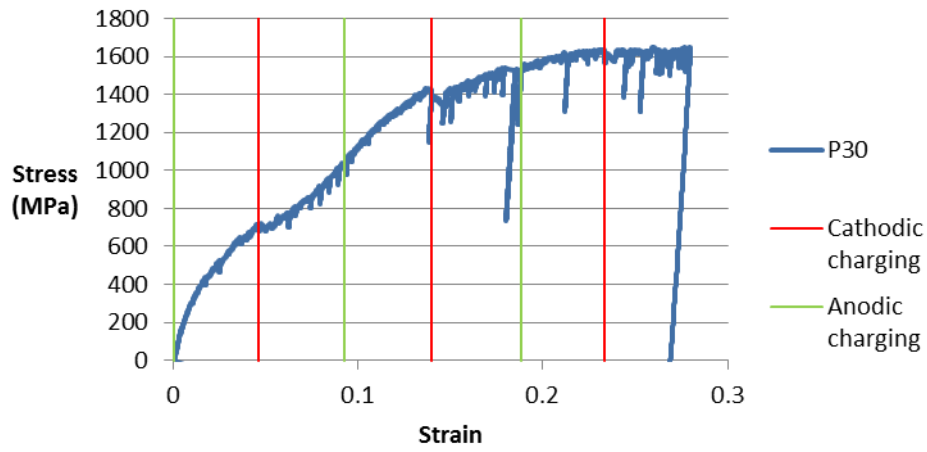
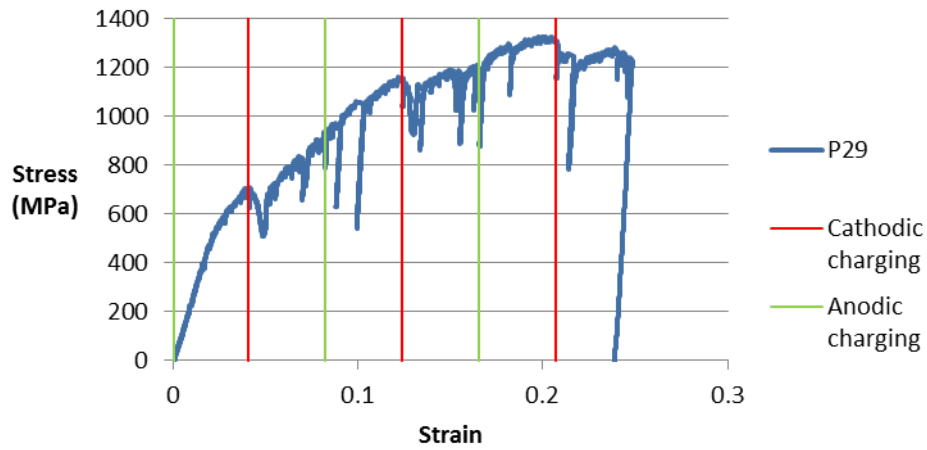
### 10.3 Experimental in situ potential switching

As explained in section 5.5.3, an experimental method involving slow displacement-controlled compression of pillar while switching the potential, was developed in cooperation with Post Doc. Afrooz Barnoush. The resulting stress-strain curves are included in Table 18, where the red and green lines represent the start of applying cathodic and anodic potential, respectively. The load function for all curves in Table 14, Table 16 and Table 18 is the one shown in Figure 24. The only exception is P26 in Table 14, where a holding segment of 200 seconds was applied after 300 seconds.









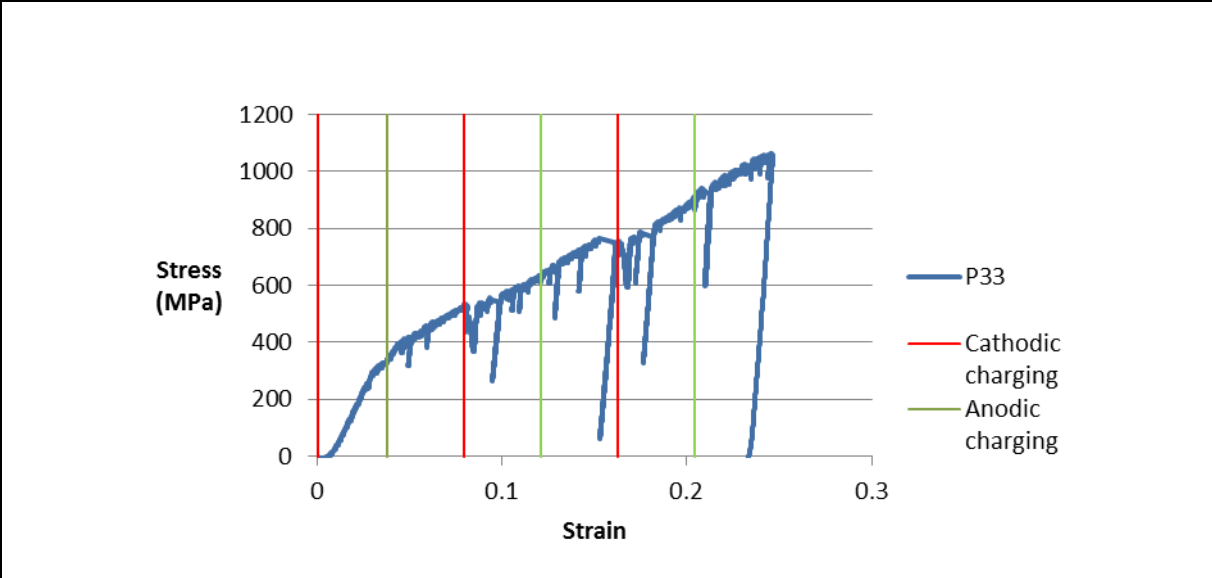
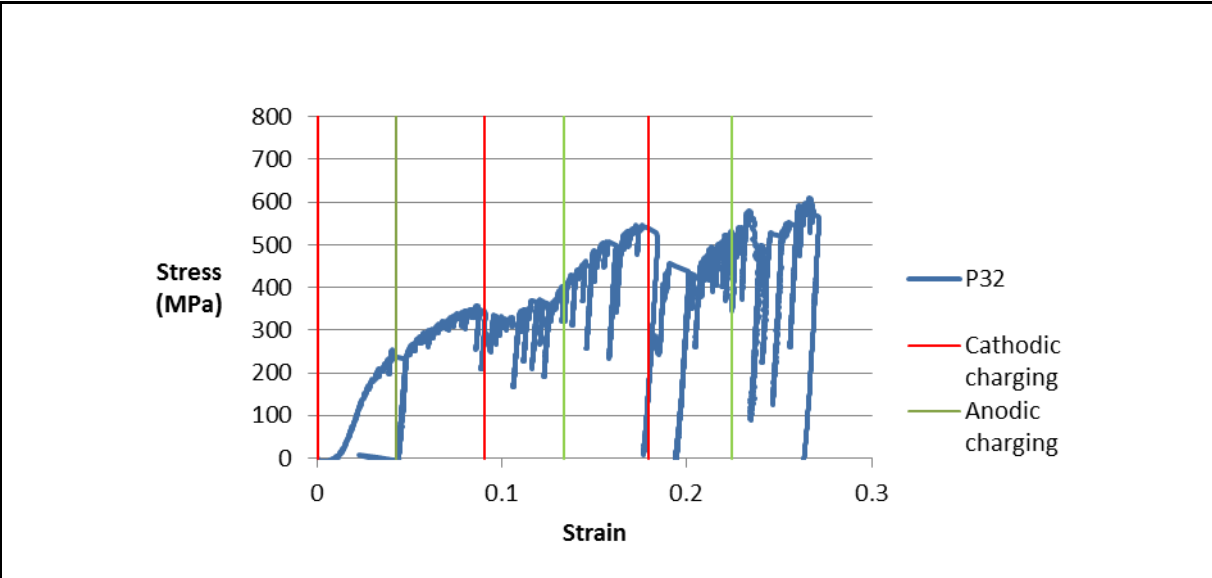
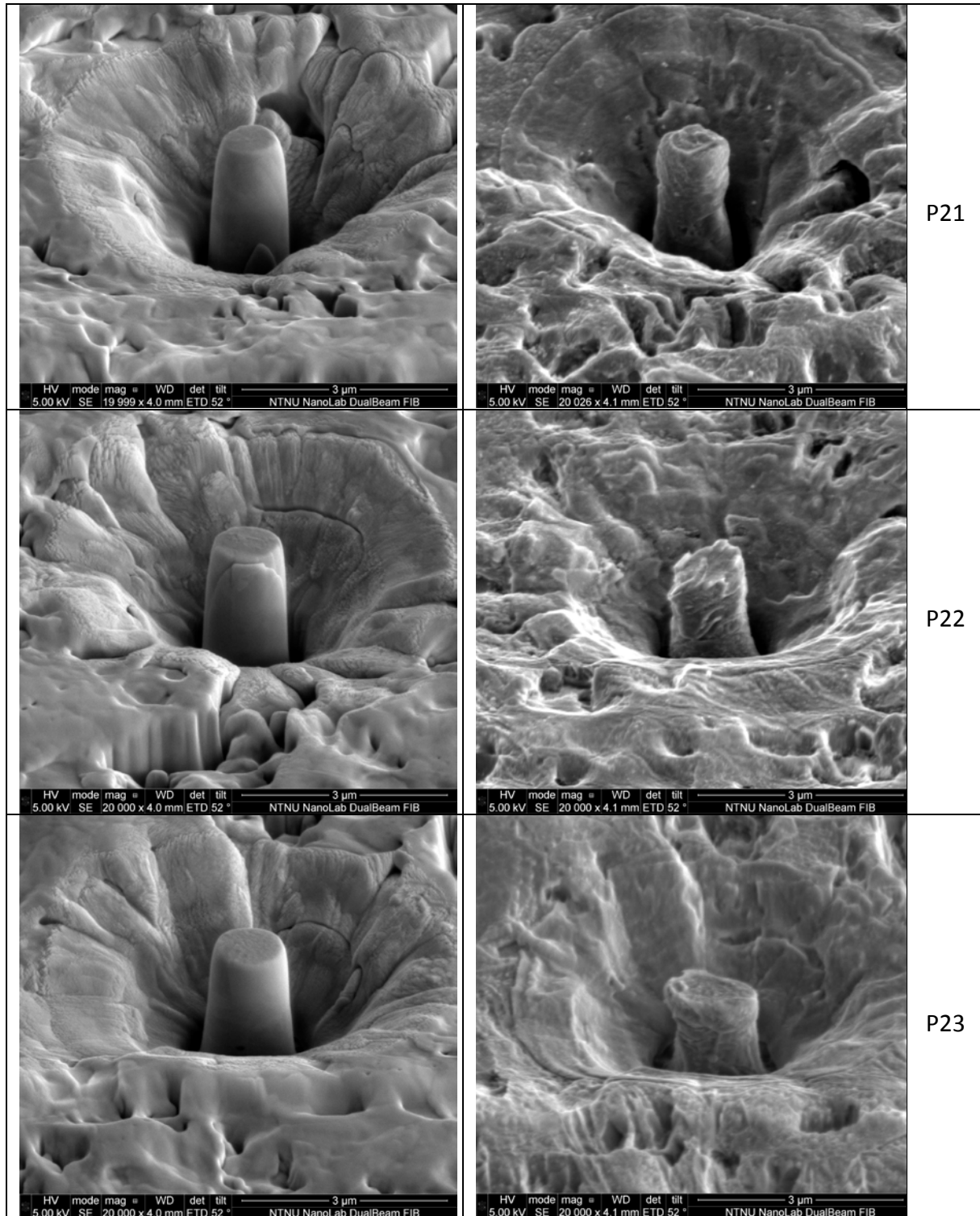
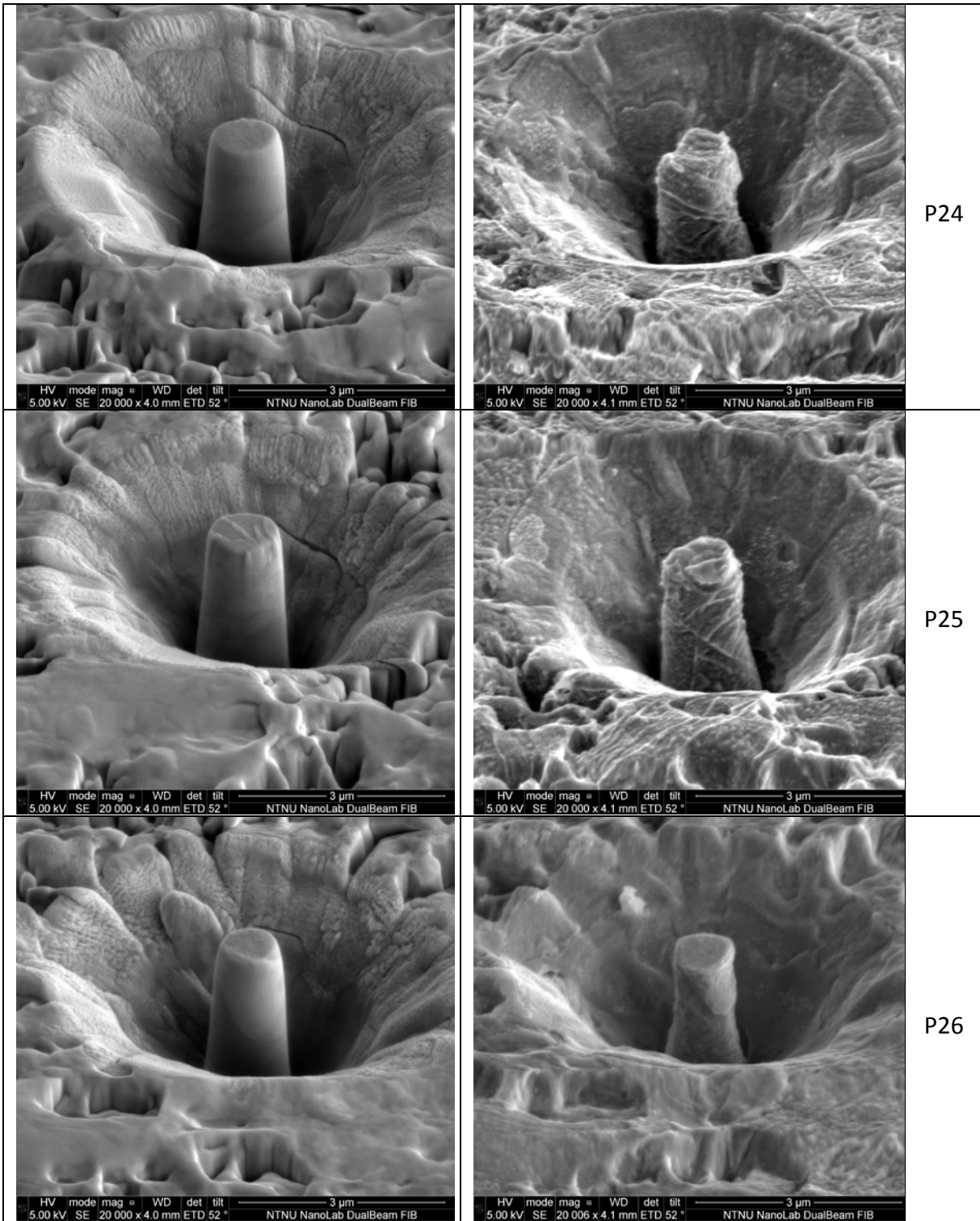


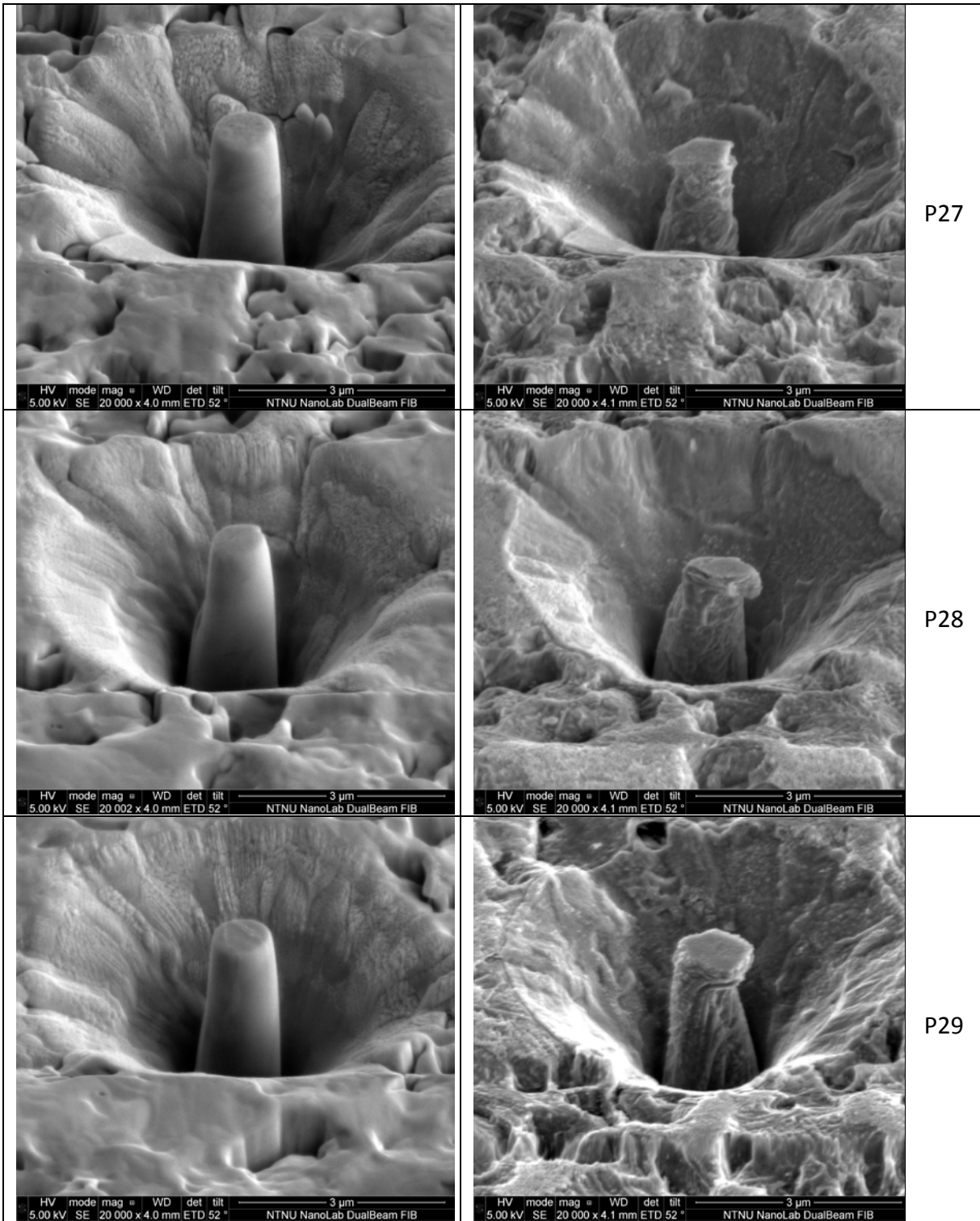
Table 14 - 1400M\_Ti pillars compressed under different potentials

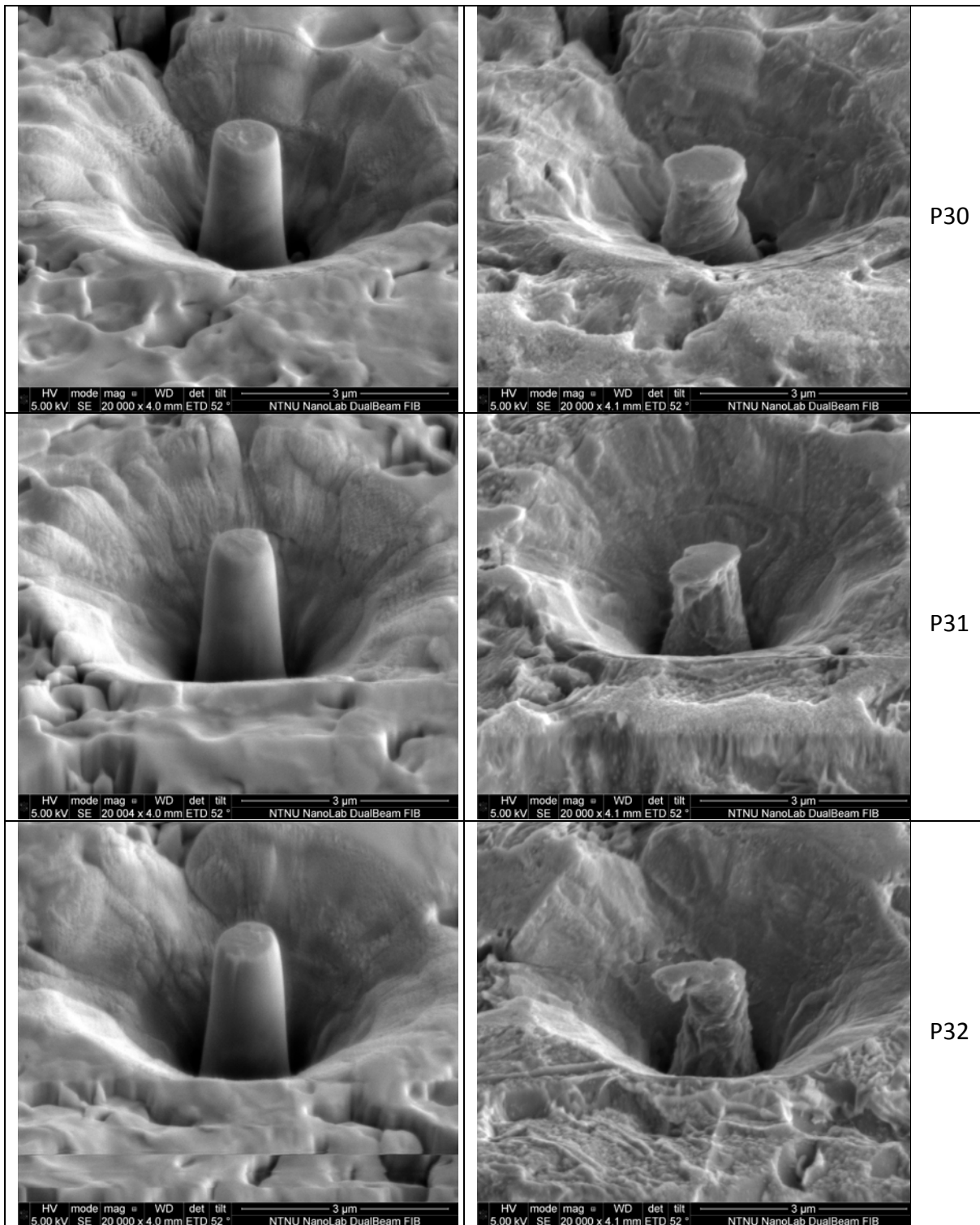


Table 15 shows the pre- and post-compression images of the test pillars from the second set of the 1400M\_Ti sample. The post-compression image is chosen to best show the deformation mechanisms. In the case of this sample the surface was corroded and the post-compression images are therefore suboptimal.









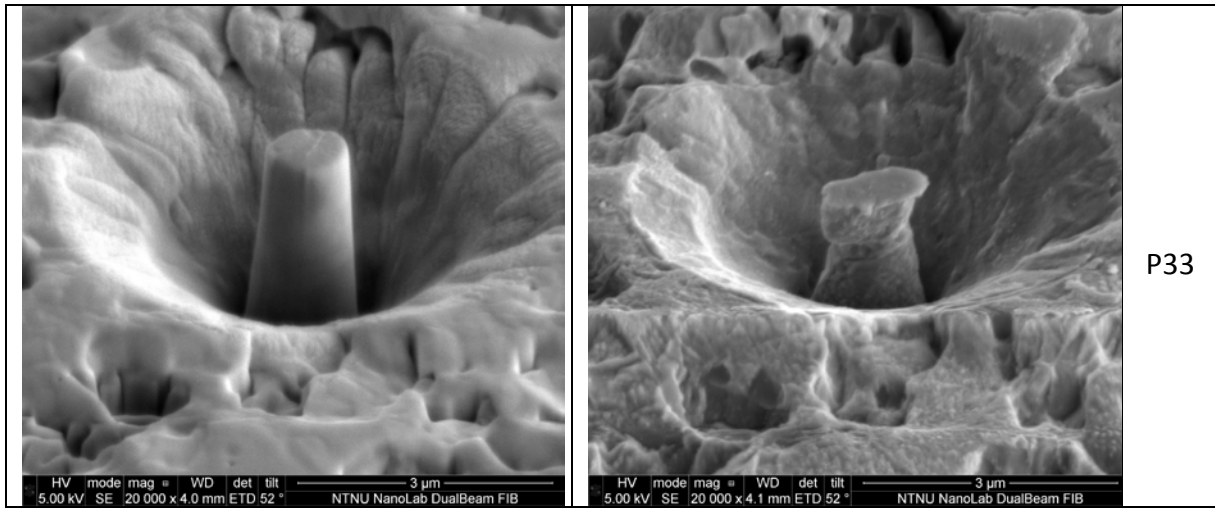
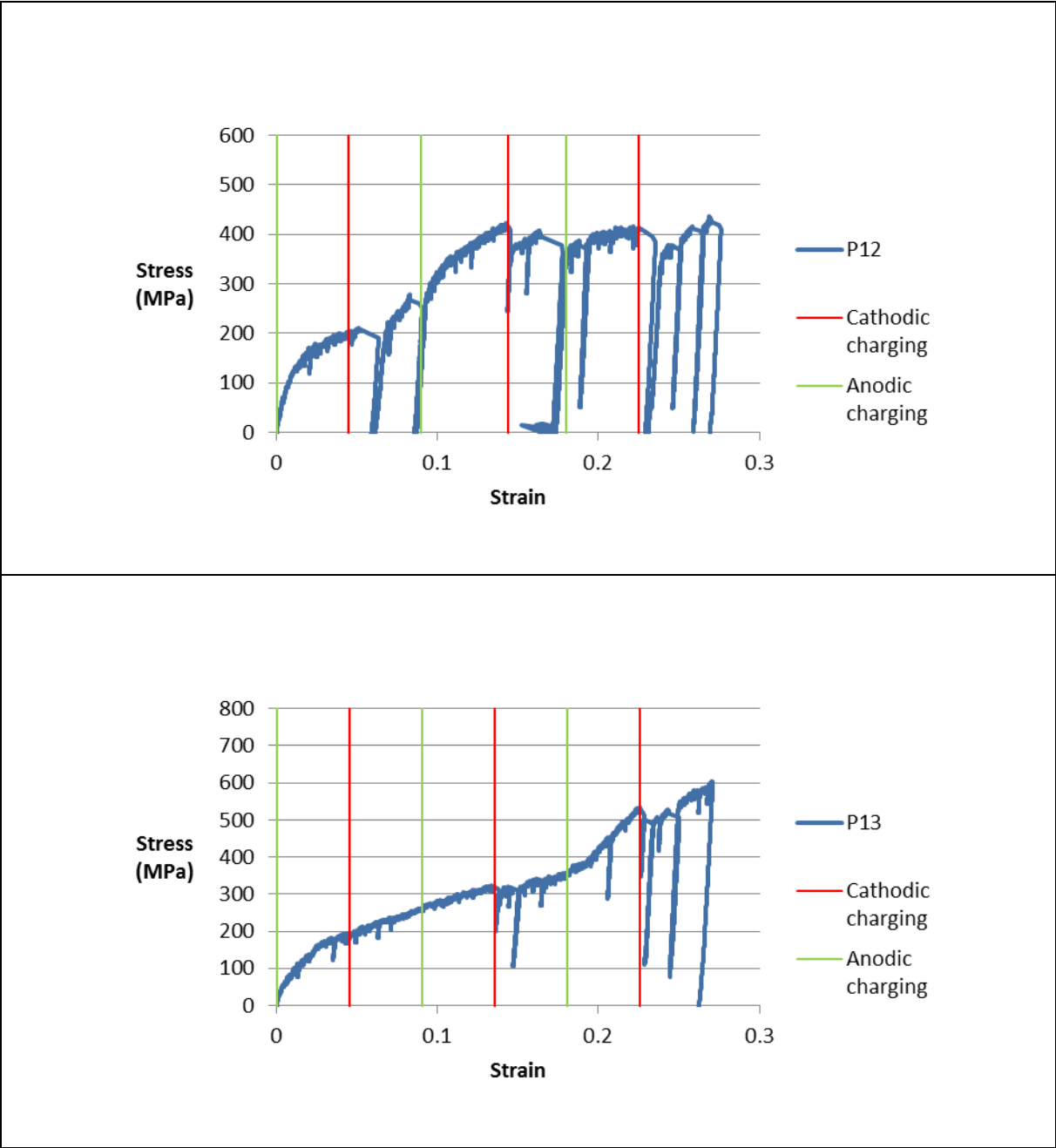
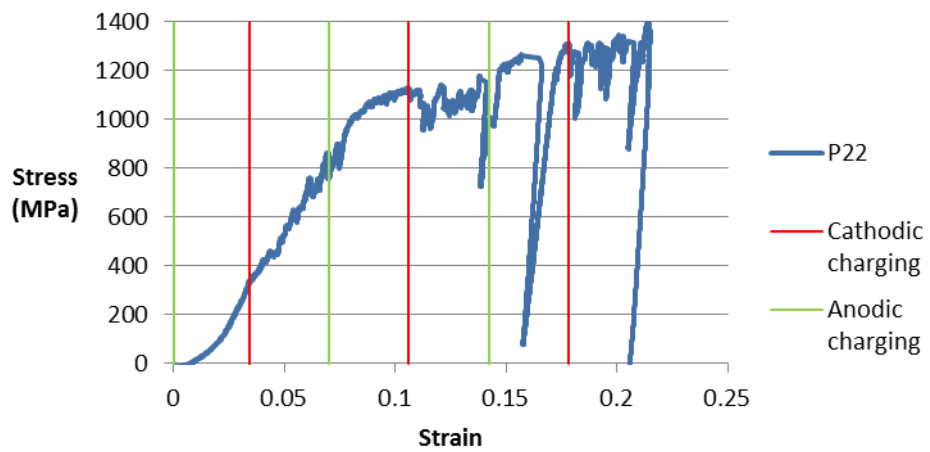
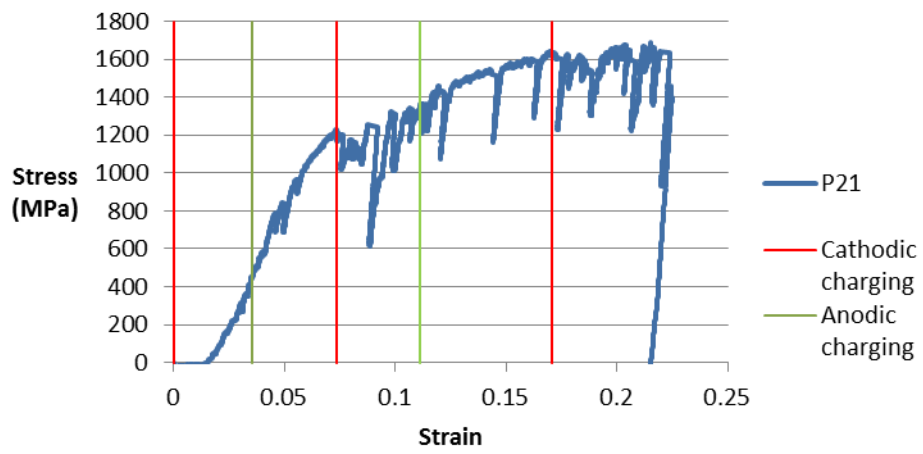
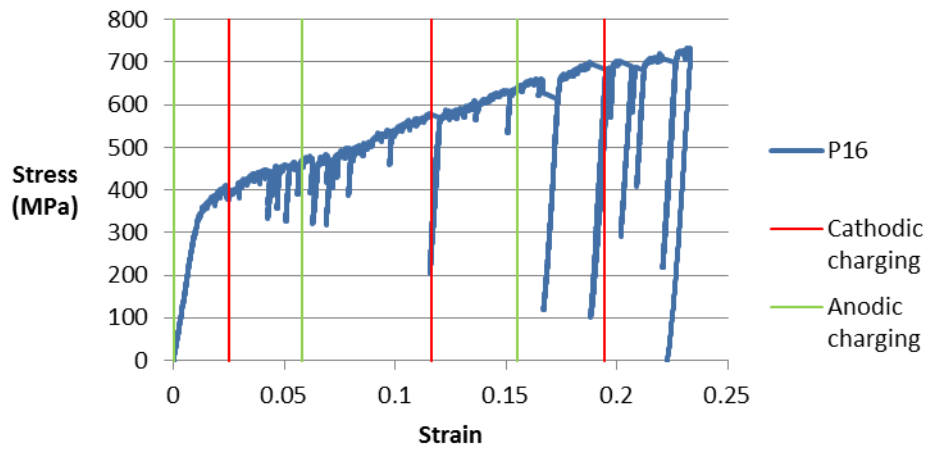


Table 15 - 1400M\_Ti pillars pre- and post-compression

Table 16 shows the stress-strain curves from the compression of the pillars on the second set of the 1400M samples, referred to as 1400M2.





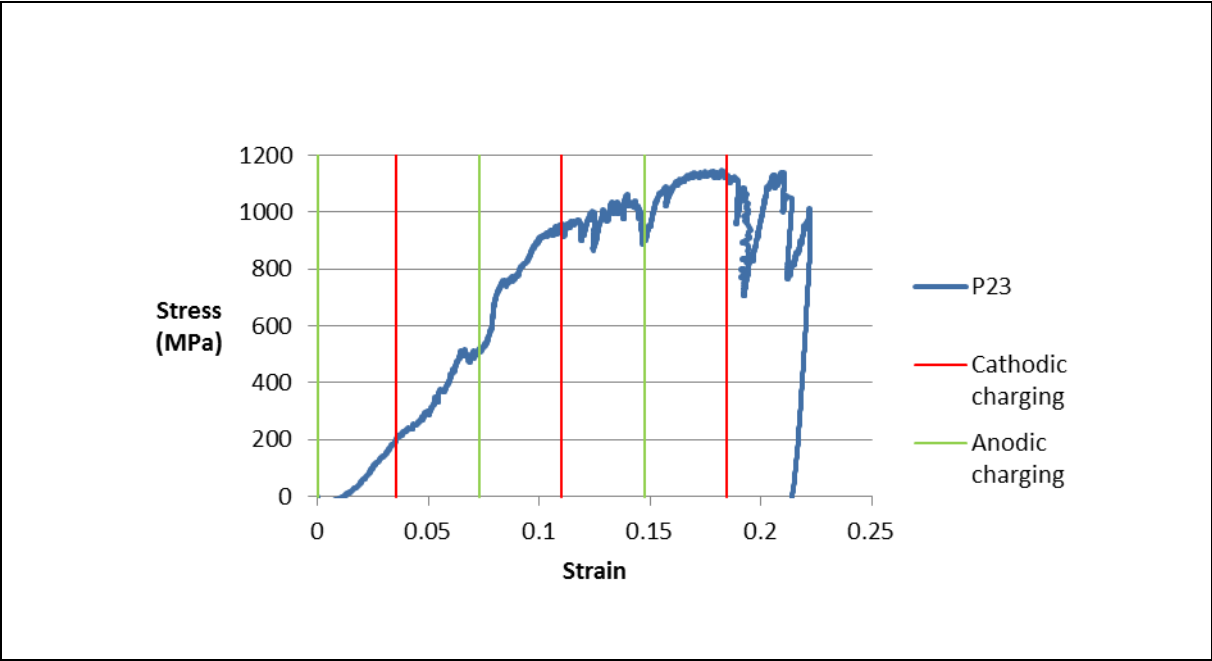


Table 16- 1400M2 pillars compressed under different potentials



Table 17 shows the pre- and post-compression images of the test pillars from the second set of the 1400M sample. The post-compression image is chosen to best show the deformation mechanisms. In the case of this sample the surface was too corroded to get images of the pillars post-compression.

		<p>P12</p>
		<p>P13</p>
		<p>P16</p>

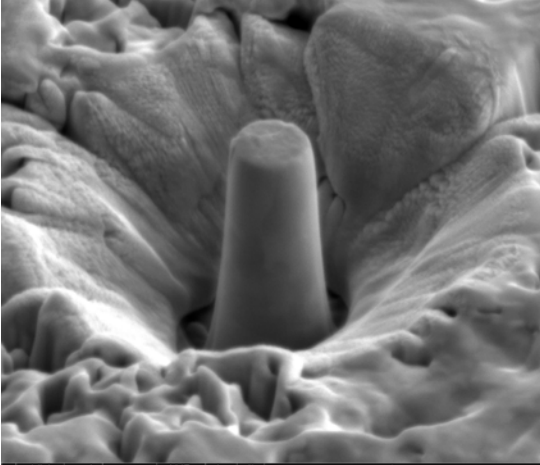
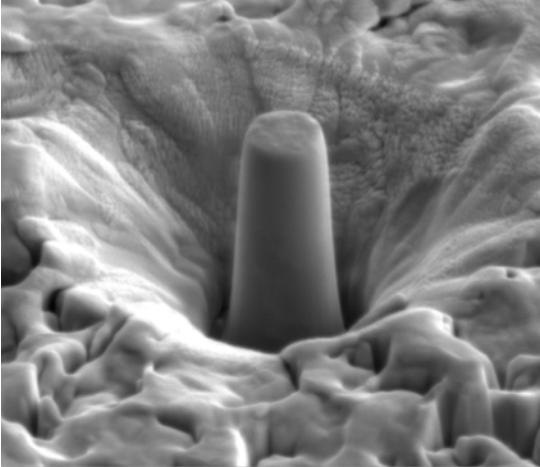
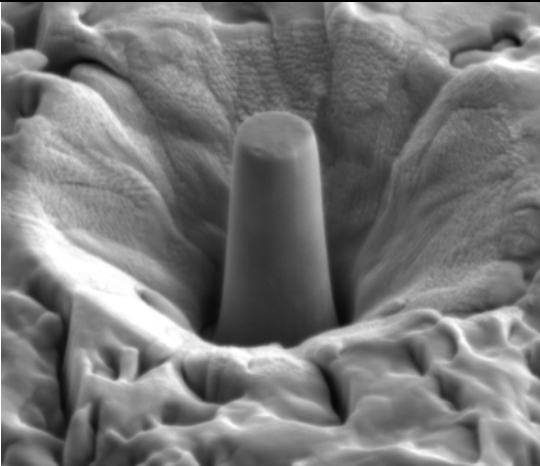
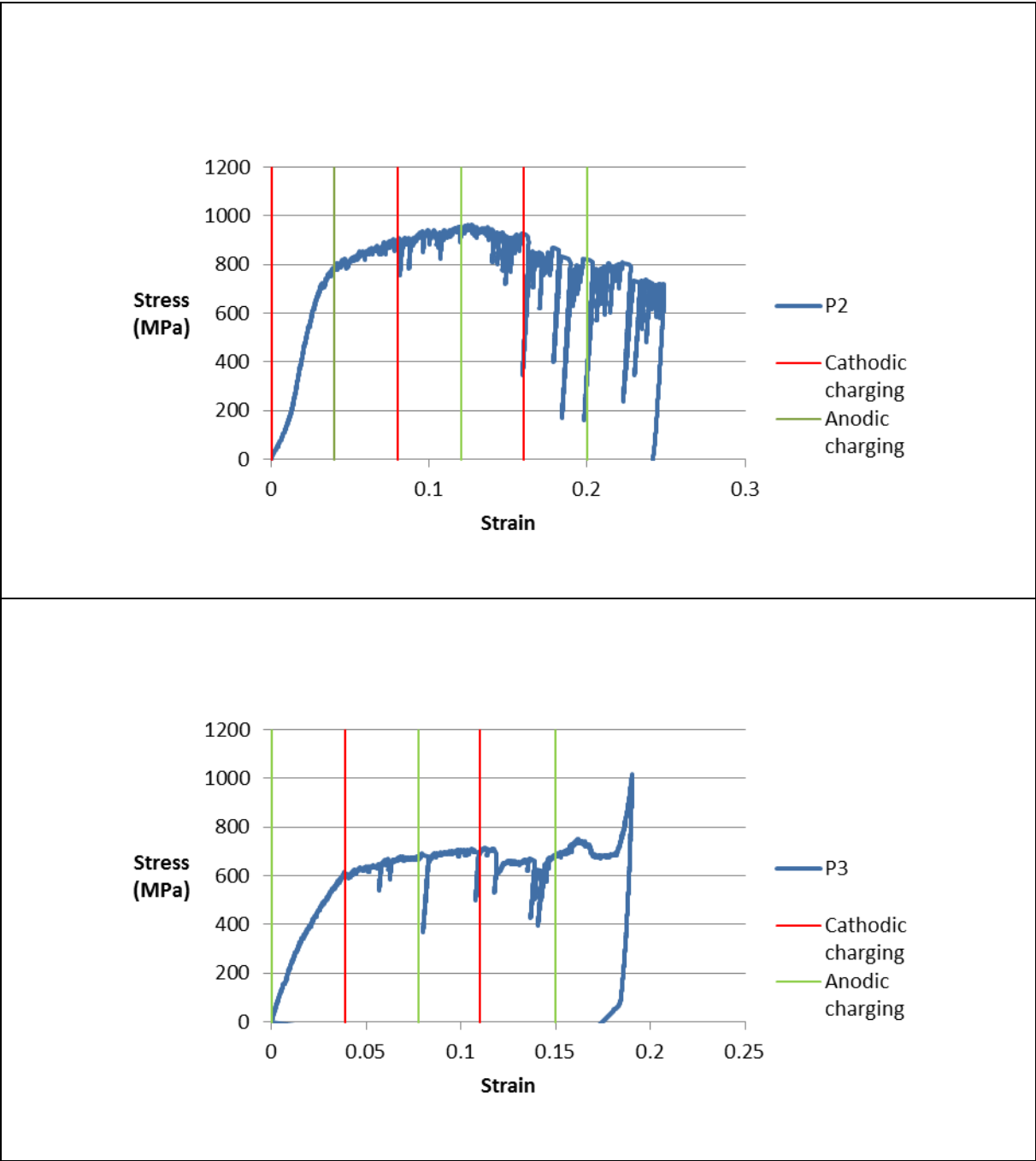
 <p>HV mode mag # WD det tilt 3 μm 5.00 kV SE 20 000 x 4.1 mm ETD 52° NTNU NanoLab DualBeam FIB</p>		P21
 <p>HV mode mag # WD det tilt 3 μm 5.00 kV SE 20 000 x 4.1 mm ETD 52° NTNU NanoLab DualBeam FIB</p>		P22
 <p>HV mode mag # WD det tilt 3 μm 5.00 kV SE 20 000 x 4.1 mm ETD 52° NTNU NanoLab DualBeam FIB</p>		P23

Table 17 - 1400M2 pillars pre- and post-compression

Lastly Table 18 is included showing the first test pillars which were compressed with switching potentials. These tests were performed on the second set of 1400M\_Ti.



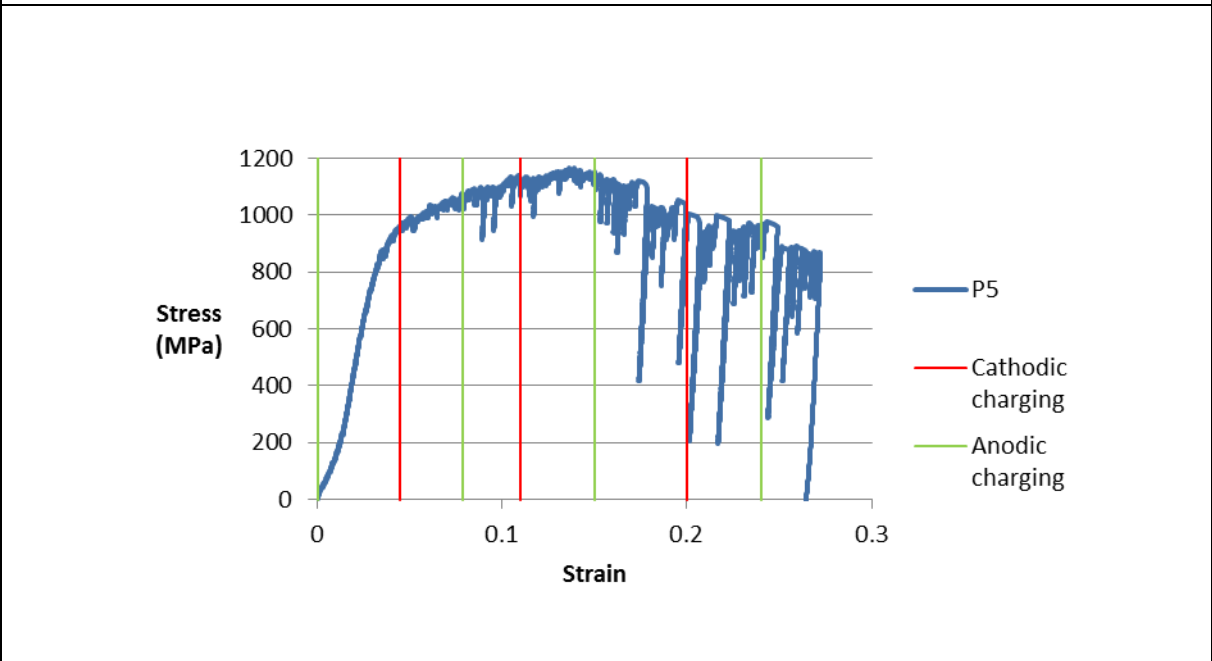
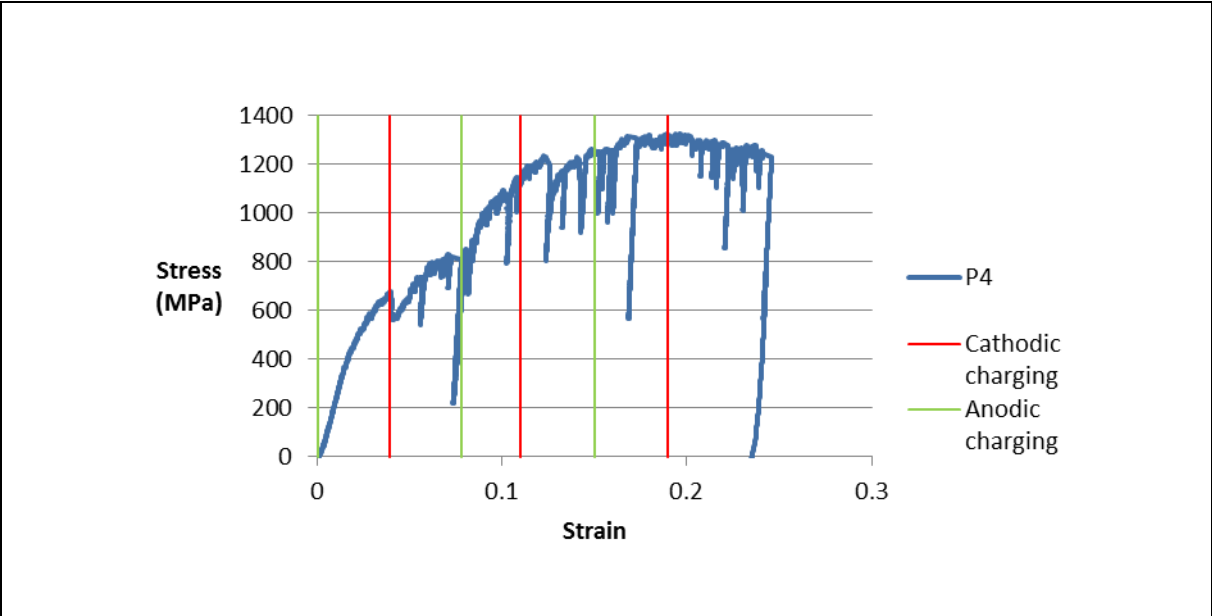

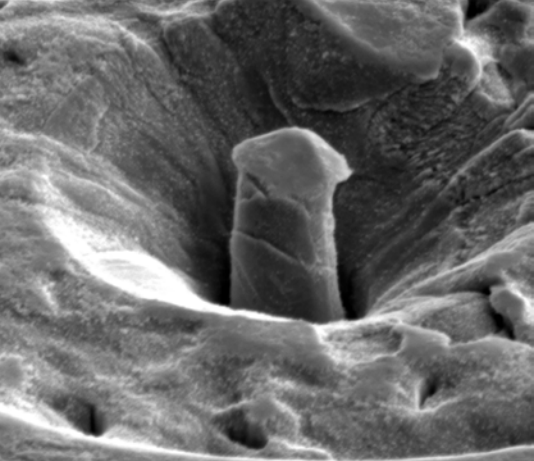


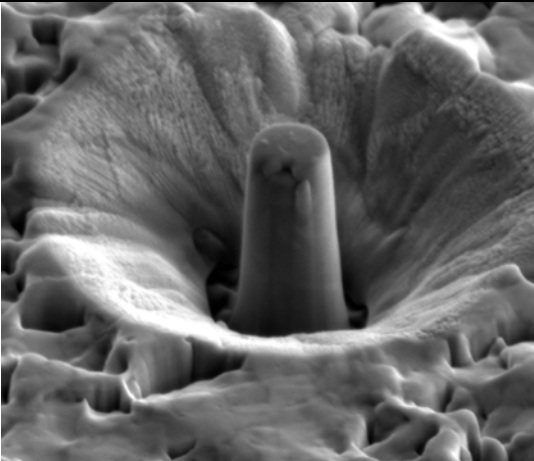
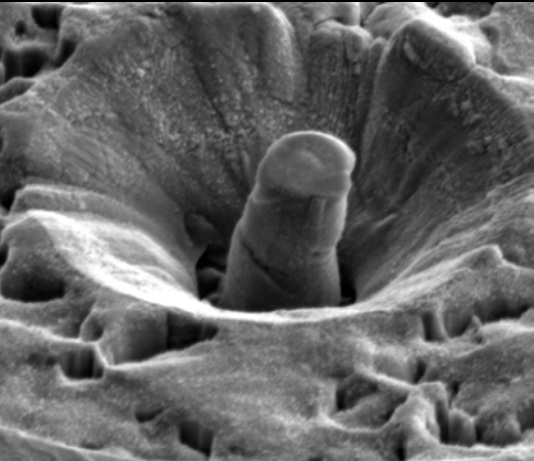


Table 18 - 1400M2Ti Pillars compressed under different potentials

Table 19 shows the pre- and post-compression images of the test pillars from the second set of the 1400M\_Ti sample. The post-compression image is chosen to best show the deformation mechanisms, and can therefore be from a different angle than the pre-compression image.

 <p>HV mode mag # WD det tilt 3 μm 5.00 kV SE 20 003 x 4.1 mm ETD 52 ° NTNU NanoLab DualBeam FIB</p>	 <p>HV mode mag # WD det tilt 3 μm 5.00 kV SE 20 000 x 4.2 mm ETD 52 ° NTNU NanoLab DualBeam FIB</p>	P2
 <p>HV mode mag # WD det tilt 3 μm 5.00 kV SE 20 000 x 4.1 mm ETD 52 ° NTNU NanoLab DualBeam FIB</p>	 <p>HV mode mag # WD det tilt 3 μm 5.00 kV SE 20 000 x 4.2 mm ETD 52 ° NTNU NanoLab DualBeam FIB</p>	P3
 <p>HV mode mag # WD det tilt 3 μm 5.00 kV SE 20 000 x 4.1 mm ETD 52 ° NTNU NanoLab DualBeam FIB</p>	 <p>HV mode mag # WD det tilt 3 μm 5.00 kV SE 20 000 x 4.2 mm ETD 52 ° NTNU NanoLab DualBeam FIB</p>	P4

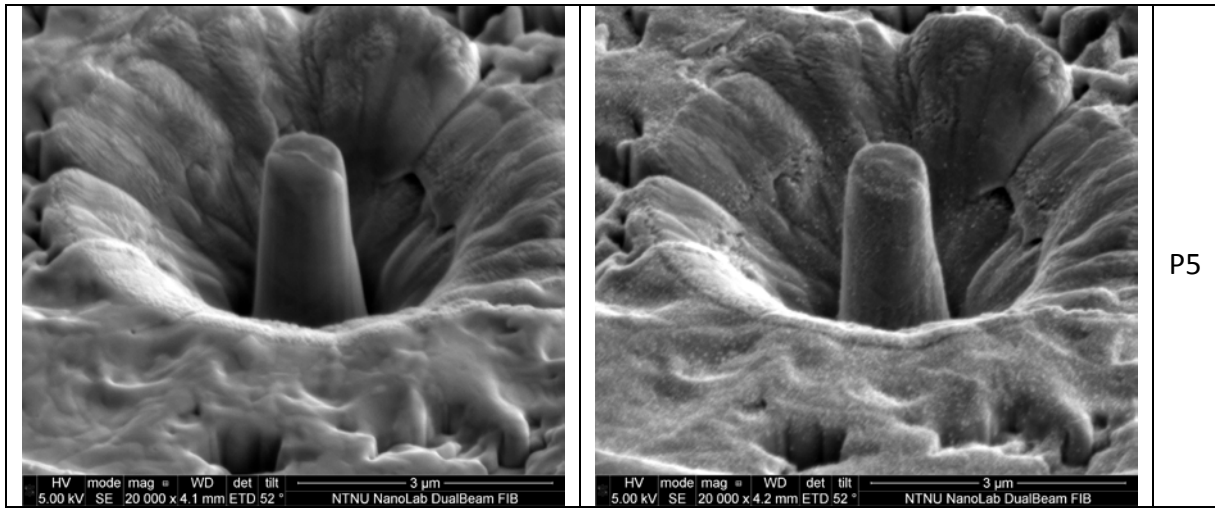


Table 19 - 1400M2Ti pillars pre- and post-compression